論文 / 著書情報
Article / Book Information

題目(和文)	CANGAROO-II 10m望遠鏡による超新星残骸SN1006からのTeVガンマ線の観測
Title(English)	Observation of TeV gamma-rays from the supernova remnant SN1006 with CANGAROO-II 10m telescope
著者(和文)	原敏
Author(English)	
出典(和文)	学位:博士(理学), 学位授与機関:東京工業大学, 報告番号:甲第4968号, 授与年月日:2002年3月26日, 学位の種別:課程博士, 審査員:
Citation(English)	Degree:Doctor (Science), Conferring organization: Tokyo Institute of Technology, Report number:甲第4968号, Conferred date:2002/3/26, Degree Type:Course doctor, Examiner:
学位種別(和文)	博士論文
Type(English)	Doctoral Thesis

Doctoral Thesis

February 2002

Observation of TeV Gamma-Rays from the Supernova Remnant SN1006 with CANGAROO-II 10m telescope

Satoshi Hara

99D01129

Department of Basic Physics
Graduate School of Science and Engineering
Tokyo Institute of Technology

Abstract

Observation of the north-eastern (NE) rim of SN1006 was carried out in April and May 2000, using the imaging atmospheric Čerenkov technique with the CANGAROO-II 10m telescope at Woomera, South Australia. The observation time is 55.2 and 48.8 hours, for ON- and OFF-source runs, respectively.

We have confirmed TeV gamma-ray emission from the NE-rim with 7σ statistical significance level at the same position as the previous result of the CANGAROO 3.8m telescope.

The energy threshold of the observed flux is estimated to be ~ 1.4 TeV by a Monte Carlo simulation assuming the inverse Compton like spectrum. The observed integral flux of the NE-rim of SN1006 is estimated to be $I(E > 1.4 \pm 0.4\text{TeV}) = (6.1 \pm 0.9(\text{statistical}) \pm 1.3(\text{systematic})) \times 10^{-12}$ [photons $\cdot$ cm^{-2} $\cdot$ sec^{-1}]. Also the differential flux between 1.25 and 3.3 TeV is estimated to be $F(E) = (7.4 \pm 2.0) \times 10^{-12} (E/1\text{TeV})^{-2.3 \pm 0.4}$ [photons $\cdot$ cm^{-2} $\cdot$ sec^{-1} $\cdot$ TeV^{-1}]. The integral and the differential fluxes are consistent with the previous results observed by the 3.8m CANGAROO telescope and support the expected magnetic field of $\sim 4\mu$G of the shock acceleration model.

In addition, the TeV gamma-ray emission region is not extended more than the point spread function of the telescope. Combined with the recent X-ray observation, this result strongly supports that the source of the TeV gamma-ray emission from the NE-rim of SN1006 is point-like and is due to the inverse Compton scattering by the ultra-relativistic electrons on 2.7K cosmic microwave background photons.

Contents

List of Figures

List of Tables

Chapter 1

Introduction

Astronomy has opened its history with the birth of a human being who looks up the sky. After the invention of the telescope, the wavelengths to observe in astronomy has been extended from radio to gamma-ray with the technological development. The observation using satellites in the space has enabled the observation in the wavelengths such as ultra violet and X-ray, which are impossible to observe on the earth because of the absorption by the atmosphere. The astronomy of the various wavelengths made many discoveries of astronomical phenomena such as the aspect of the star birth, the X-ray pulsar of the binary system, the X-ray burst, and so on. Gamma-ray astronomy is a new frontier, which is able to probe the deep universe and to understand the very high-energy cosmic phenomena.

The first high-energy cosmic phenomenon known in history is the discovery of cosmic-rays by Hess in 1912. After that, in the latter half of twenty century, radio and X-ray astronomy have started, and we have known the various aspects of the universe through the high-energy phenomena. They did not only stir up our curiosity for the unknown aspect of the universe but also provide the ideal laboratories in extreme physical conditions which cannot be artificially produced on the earth. For example, some of cosmic-rays have higher energy than those made in accelerators on the earth. Therefore, the above fact indicates the existence of the unknown mechanism to accelerate particles in the universe. However, due to the magnetic field extended in the Galaxy ($\sim 3\mu$G), cosmic-rays, which are mainly protons, cannot propagate directly from the acceleration sites of cosmic-rays to our observation sites, except for the most energetic cosmic-rays, of which tracks are hardly bent by the Galactic magnetic field [15]. The Larmor radii of the protons of 10^{15}eV and 10^{18}eV in the Galaxy are about 0.1 pc and 0.1 kpc, respectively. This problem of where high-energy cosmic-rays are generated remains unanswered. On the other hand, neutral particles such as photons and neutrinos are not bent by the magnetic field, and propagate to the earth preserving the information of the direction. Especially, non-thermal photons, namely radio, X-rays and gamma-rays, are expected to be generated simultaneously at the acceleration sites of cosmic-rays through several interactions between particles and fields.

Thus, information about the origin of cosmic-rays can be obtained from the non-thermal photons. However, it is difficult to distinguish the non-thermal photons from thermal radiations, which are dominant in the Galaxy, especially in the lower energy region.

In 1950's, Hayakawa and Morrison pointed out the importance of gamma-ray astronomy. Several gamma-ray sources were predicted as possible acceleration sites of comic-rays [13] [43]. In 1960's, satellite experiments were launched in order to find gamma-ray sources. A prologue in the history of the gamma-ray astronomy is the observations by the satellites of OSO-3, SAS-II and COS-B in the latter 1960's.

In particular, the observation during six and a half years of COS-B satellite [67], found strong diffuse radiation of gamma-rays along the Galactic plane with the energy range between 35 MeV and 5 GeV. In addition, 25 isolated gamma-ray sources with energies of over 100 GeV were also detected. However, since the angular resolution of the detector on the COS-B was only $\sim$ 1 degree, it was difficult to identify the sources emitting gamma-rays, except for a several sources, Crab pulsar, Vela pulsar and active galaxy nucleus 3C373. For example, the very intensive gamma-ray source called Geminga could not be identified even in the wavelength of radio, optical or x-ray. After COS-B, a large experiment using a satellite had waited until the advent of CGRO satellite in 1990's.

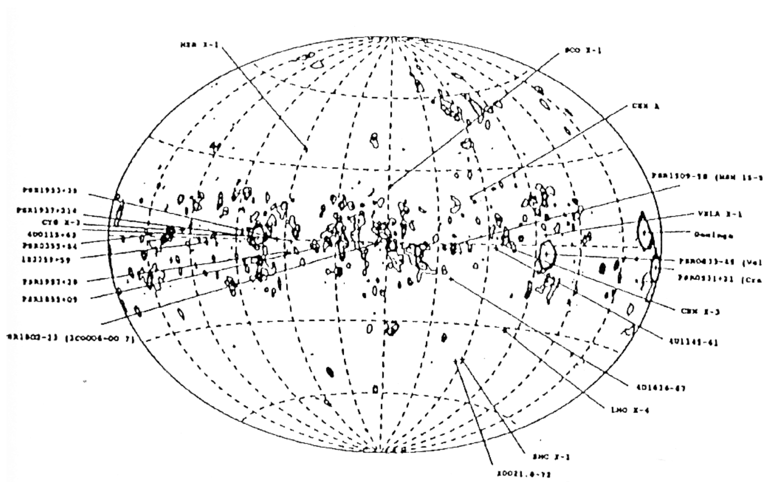

Figure 1.1: Sky map of gamma-ray sources obtained by the COS-B satellite [71].

On the other hand, in the higher energy region of more than 100 GeV, gamma-ray observations were done on the ground. In general, gamma-ray fluxes are monotonically decreased in power law as its energy increasing. Hence the detectable energy of a satellite observation is limited only to several GeV because of the restricted effective area. However, the ground based observation using an extensive air shower technique can obtain a very large effective area (chapter 3.1, Figure 1.2). Several observations based on the ground have been carried out since

1960's. In spite of a lot of experiments during those years, there had been no reliable evidence of the detection of celestial high energy (∼TeV) gamma-rays before 1990's.

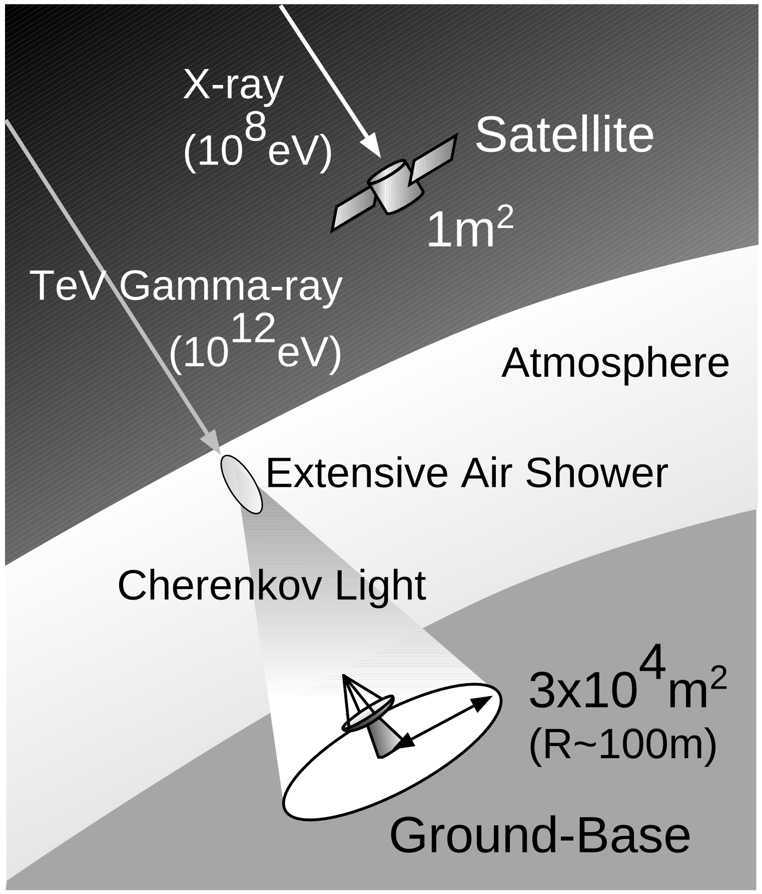

Figure 1.2: The comparison between satellite and ground-base observations.

In 1990's, gamma-ray astronomy had been developed dramatically, in both satellite and ground-based observations. Former success was brought by the U.S. gamma-ray satellite, Compton Gamma Ray Observatory (CGRO), which was launched in 1991. CGRO was a large satellite experiment for gamma-ray astronomy, and consisted of four detectors, BATSE, OSSE, COMPTEL and EGRET. In particular, EGRET (Energetic Gamma Ray Experiment Telescope) consisting of a set of spark chambers and an NaI calorimeter, observed the highest energy region of 30MeV ∼ 30GeV in the CGRO, and found 271 gamma-ray sources[12], most of which are newly discovered. According to the EGRET third catalog, there are the Large Magellanic Cloud, a solar flare in 1991, 6 pulsars, 1 probable radio galaxy (Cen A), 66 high-confidence blazer identifications (BL Lac objects, flat-spectrum radio quasars, or unidentified flat-spectrum radio sources), 27 lower confidence blazer identifications, and 170 unidentified sources, which are plotted in Figure 1.4. Many of those unidentified sources, which do not coincide to any object known in other wavelengths, are distributed along the Galactic plane, and are considered probably to be associated with pulsars or supernova remnants. However, due to the poor angular resolution of EGRET of ~ 1 degree [72], it could not identify them with observed objects. Further development of gamma-ray astronomy with satellites will be provided by GLAST (Gamma-ray Large Area Space Telescope), which is a next large gamma-ray satellite observing the energy range of 10MeV $\sim$ 100GeV with a large effective area and high efficiency [87] [20].

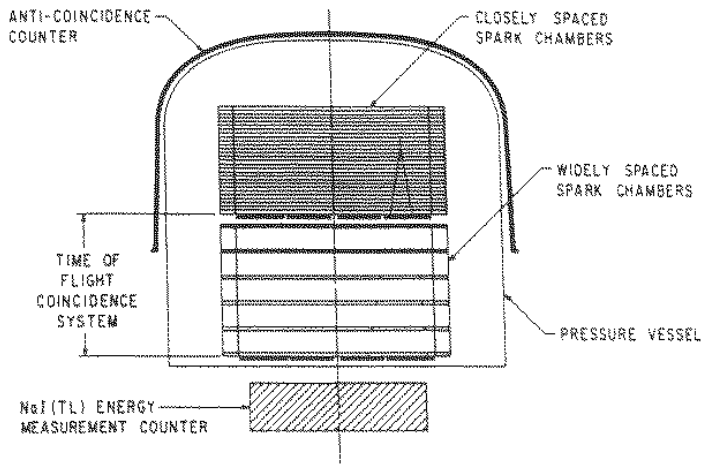

Figure 1.3: EGRET detector [36].

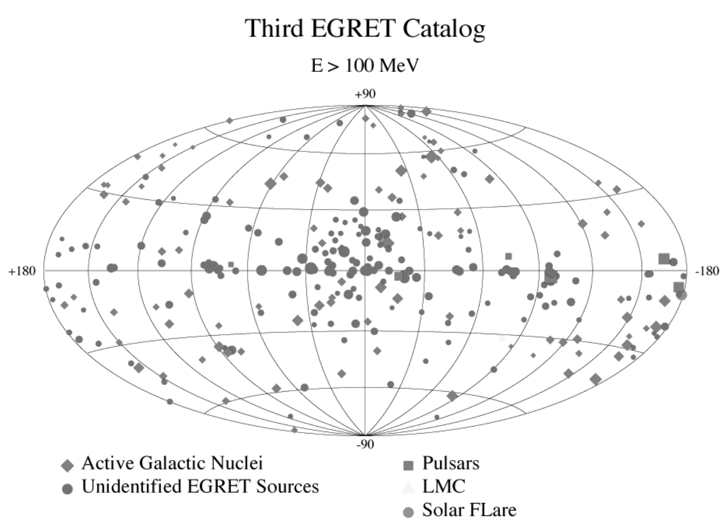

Figure 1.4: Sky map of gamma-ray sources obtained by EGRET [90].

Another great success of gamma-ray astronomy has made in the TeV region by the ground

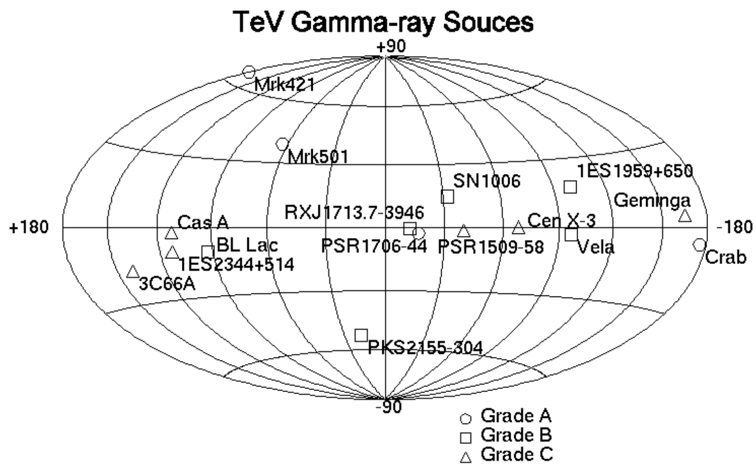

Figure 1.5: Sky map of TeV gamma-ray sources.

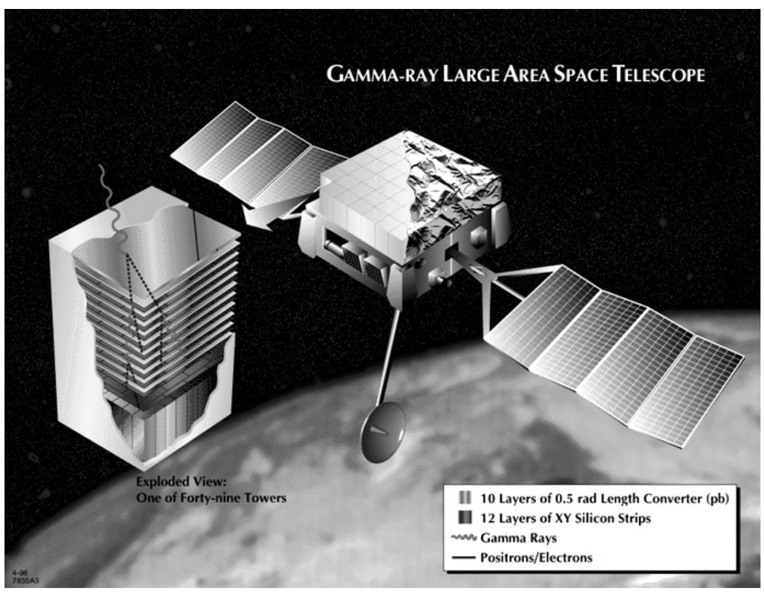

Figure 1.6: Gamma-ray satellite, GLAST [91].

based observation. In 1989, Whipple observatory had succeeded in detecting a steady TeV gamma-ray emission from the Crab nebula with a high confidence level using the imaging technique [78] (chapter 3.3). After this detection, several ground based telescopes also succeeded in detecting TeV gamma-ray signals from the Crab. Moreover, in 1994, Whipple group unexpectedly detected the significant TeV gamma-ray signals from the BL Lac object Mrk421 [55]. Soon, multi-band observations from radio to TeV gamma-ray were carried out, then the wide continuous spectrum from radio to gamma-rays and the large time variation were found. By these observations, TeV gamma-ray observations have been recognized to play an important role in astronomy.

In the northern hemisphere, the Crab, Mrk421 and Mrk501 were detected as TeV gamma-ray sources. On the other hand, the CANGAROO project, which is the international experiment between Japan and Australia since 1991 (chapter 4.1), had started the observation for TeV gamma-ray sources in the southern hemisphere. The observation in the southern hemisphere is of a great importance; ground based telescopes in northern hemisphere are not able to observe all of the southern sky, and there are many gamma-ray sources detected by EGRET near the Galactic center in the southern sky. The CANGAROO group had detected TeV gamma-ray signals from the pulsar PSR B1706–44 in 1993 [25], which was the first detection of TeV gamma-ray sources in the southern sky. After this detection, TeV gamma-ray signals from Vela pulsar [84], supernova remnant(SNR) SN1006 [68], and SNR RXJ1713.7–3946 [41] were detected in the southern sky using the CANGAROO 3.8m telescope (Figure 1.7).

In particular, the detection of the gamma-ray emission from SN1006 was the first direct evidence of the shock acceleration of the high-energy particles in SNRs. For a long time, SNRs have been believed to be a favored site for accelerating cosmic-rays up to 10^{15} eV, because only they can satisfy the required energy input rate to the Galaxy among several Galactic objects which show high-energy phenomena (chapter 2.4). In addition, a shock acceleration theory was established around 1980's, in which particles are accelerated with the collisions between particles and plasma gas moving at a super-sonic velocity (chapter 2.3). In 1995, Japanese X-ray satellite *ASCA* has found the strong non-thermal X-ray emission from SN1006. This detection of the synchrotron emission is the first reliable evidence for the efficient particle acceleration in SNR. TeV gamma-ray emission by inverse Compton process (chapter 2.1) assuming conventional magnetic field has been indicated by this X-ray detection. From these successes, detection of high-energy gamma-rays from SNRs becomes a good probe for investigating the origin of cosmic-rays.

On the other hand, an upper limit has been placed for the gamma-ray emission from the SN1006 at 300 GeV [3]. Therefore, it is necessary to confirm the emission of TeV gamma-rays from SN1006. In 1999, we constructed new telescope, the CANGAROO-II telescope (chapter 4), in order to investigate sub-TeV energy region. The confirmation of TeV gamma-ray emission from SN1006 is one of the most important motivations of this CANGAROO-II project. Also if we measure the spectrum of TeV gamma-rays, the spectral study will tell us what kind of particles are accelerated and generate gamma-rays. For example, the model based on the inverse Compton mechanism predicts the break of the gamma-ray spectrum around 1 TeV region. With these motivations, the NE-rim of the SN1006 was studied with by the CANGAROO-II 10m telescope, in April and May 2000. In this observation, the telescope was pointed to the NE-rim, where TeV gamma rays were found in the previous observation using the CANGAROO 3.8m telescope.

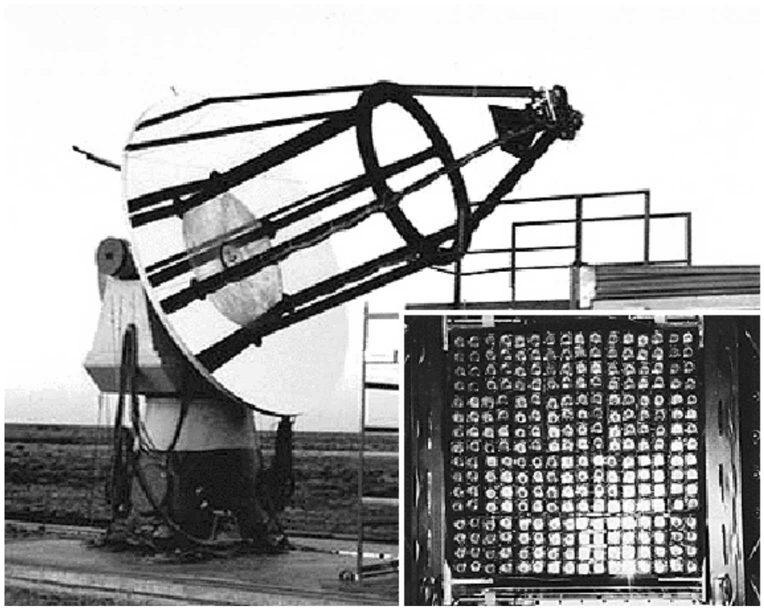

Figure 1.7: CANGAROO 3.8m telescope and the imaging camera.

This thesis is planed as follows. In chapter 2, a review is given on physical processes for TeV gamma-ray emission taking place in supernova remnants. Those for SN1006 are also described in this chapter. In chapter 3, the observational concepts and the technique of TeV gamma-ray detection are explained. In chapter 4, the CANGAROO experiment and the CANGAROO-II 10m telescope are described. In chapter 5, the summary of the SN1006 observation and the detail of the data calibrations are given. In chapter 6, the detail of data analysis is described. In chapter 7, the resultant spectrum of the NE-rim of the SN1006 and the significance map around the SN1006 are presented. Finally in chapter 8, I summarize the results obtained from the observation of SN1006, and discuss the high energy phenomena in SN1006 by comparing with a model.

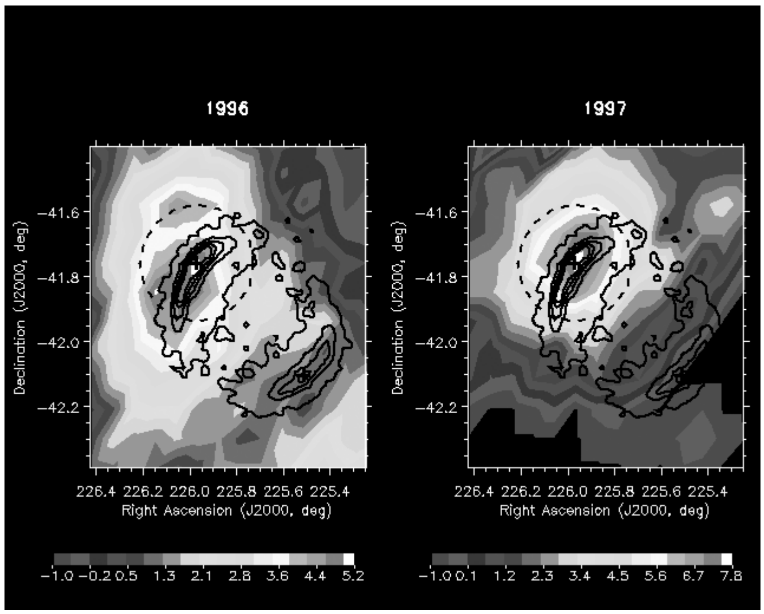

Figure 1.8: Previous result of SN1006 with the CANGAROO 3.8m telescope [68].

Chapter 2

Review on High Energy Gamma-Rays from Supernova Remnant

2.1 Production Process of VHE Gamma-Rays

Gamma-rays are most energetic photons, of which energies cover from $\sim$ 100 keV up to the highest energy of $\sim 10^{20}$ eV. Several detection methods of gamma-rays are used depending on the energy.

In the energy region less than 10 GeV, gamma-rays have been observed using satellites, while limited effective area of the satellite makes it difficult to detect higher energy gamma-rays as mentioned in Introduction. However using the atmosphere of the earth as a Čerenkov radiator, a very large detection area is obtained by the ground based telescopes (mentioned in chapter 3). Therefore, very high-energy (VHE) gamma-rays over 100 GeV are observed using the ground based detectors. Table 2.1 shows the classification of gamma-ray astronomy according to the energy range. The region of the CANGAROO project is classified as VHE gamma-rays.

511 keV $\sim$ 10 MeV	low/nuclear energy (LE)	scintillator (satellite)
10 MeV $\sim$ 30 MeV	medium energy (ME)	Compton telescope (satellite)
30 MeV $\sim$ 10 GeV	high energy (HE)	spark chamber (satellite)
10 GeV $\sim$ 100 TeV	very high (VHE)	atmospheric Čerenkov (ground)
100 TeV $\sim$ 100 PeV	ultra high (UHE)	air shower array
100 PeV $\sim$ 100 EeV	extremely high (EHE)	air shower array

Table 2.1: Classification of gamma-ray astronomy [77].

Here, production processes of VHE gamma-ray from accelerated charged particles are mentioned.

- **Neutral pion decay:**

  When a high energy proton (or nucleus) interacts with matter or ambient radiation, neutral pions are generated. Generated neutral pions immediately decay in two gamma-rays within the mean lifetime of $0.83 \times 10^{-16}\gamma_\pi$ seconds, where γ_π is the Lorentz factor of the neutral pion (Figure 2.1). These gamma-rays have similar energy spectrum to that of the parent high-energy particles (i.e. proton or nucleus).

- **Inverse Compton scattering:**

  The scattering of photons by low-energy free electrons is called Compton scattering, in which photons partly lose their energies. Conversely, when the energy of the electron is sufficiently higher than that of the photon, the photon gains its energy from the electron. This process is called inverse Compton (IC) scattering (Figure 2.2). When a relativistic TeV electron interacts with an ambient photon of 2.7K cosmic micro-wave background, a VHE gamma-ray is produced by IC process. The net power transferred from an electron to photons by the IC scattering is given as

  $$P_{\mathrm{IC}} = \frac{4}{3}\sigma_{\mathrm{T}} c \gamma^2 \beta^2 U \ , \tag{2.1}$$

  where σ_{T}, γ, β and U are the cross section of Thomson scattering, the Lorentz factor of the electron, the velocity of the electron in unit of c (light-velocity), and the energy density of the radiation field, respectively. This process is important, where the ambient photons are dense.

- **Bremsstrahlung:**

  When an accelerated electron (or any other charged particle) is passed through the Coulomb field of a nucleus, bremsstrahlung photons are emitted with a spectral distribution of $\sim 1/E_\gamma$ (E_γ is the energy of bremsstrahlung photons). Therefore, more photons are emitted at lower energies. Where matter is dense this process become dominant.

- **Synchrotron radiation:**

  Charged particles bent by a magnetic field also emit electro-magnetic radiations. When charged particles are relativistic, the radiation is called synchrotron emission (Figure 2.2). In a homogeneous magnetic field of strength H in Gauss, the characteristic photon energy E (eV) is given as follows [56],

  $$E = 5 \times 10^{-9} H \sin\theta \gamma^2, \tag{2.2}$$

where γ and θ are the Lorentz factor of the electron, and the angle between the direction of the electron and the magnetic field, respectively. This equation implies that only extreme relativistic electrons in an extreme strong magnetic field can emit VHE gamma-rays. However, we stress that low energy photons generated by this process play an important role as a target photons in inverse Compton process.

- **Curvature radiation:**
  In the exceptionally strong magnetic field of a pulsar such as 10^{12} Gauss, high energy electrons and positrons are constrained to move parallel to the magnetic flux line. These particles are accelerated and decelerated when they move along the curved field lines, and radiate "curvature" radiation in their moving direction. The characteristic energy of this radiation E (eV) is given as follows [56],

$$E_c \sim \frac{3}{2}\frac{\hbar c\gamma^3}{\rho_c} = \frac{2.96 \times 10^{-5}\gamma^3}{\rho_c}, \tag{2.3}$$

  where ρ_c, $\hbar = h/2\pi$ and γ are the radius of curvature of the magnetic flux line in unit of cm, Plank constant, and the Lorentz factor of the particle, respectively. For example of a typical pulsar of $\rho_c \sim 10^8$ cm and electron energy of $\sim 10^{13}$ eV, gamma-rays of ~ 2.5 GeV are emitted. This process is important for very high energy electrons and positrons around the pulsar surface.

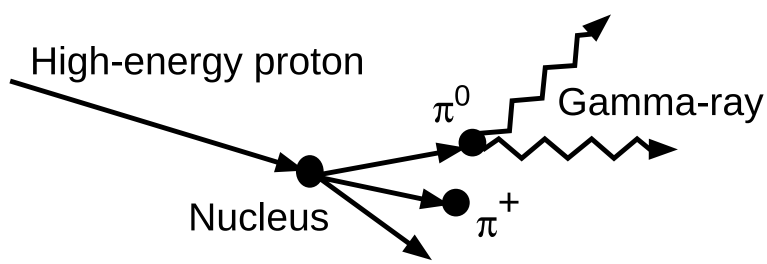

Figure 2.1: Neutral pion decay process.

Among the above processes, inverse Compton scattering is the most significant or dominant in producing VHE gamma-rays, since accelerated electrons can give almost all their energies to the scattered photons. Mechanisms to accelerate charged particles to the energies greater than the VHE region are described in the following section.

2.2 Supernova and Supernova Remnant

Supernova (SN) is one of the most explosive events in the universe, which is a final phase of the star evolution. In observations, there are two types of SNe, according to the absence or presence

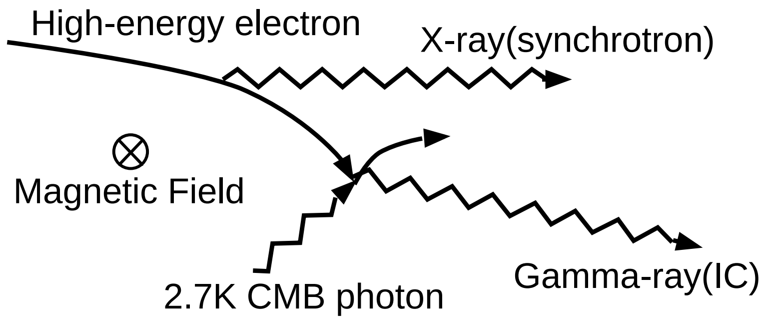

Figure 2.2: Inverse Compton and synchrotron processes.

of the hydrogen line in their spectra, which are called type-I or type-II, respectively. Most of type-I SNe have a silicon optical emission line, and are sub-classified as type-Ia, which is one of the major classes of SN. The existence of the hydrogen line means the existence of a hydrogen envelope around the progenitor star before the explosion.

- **Type-Ia Supernova**
  Absence of the hydrogen line in SN suggests no hydrogen envelope on the progenitor star. The standard scenario of type-Ia SN assumes as follows [47]. There exists a closed binary system consisting of a white dwarf (WD) and a companion star with an intermediate mass ($M < 8M_{\odot}$; $M_{\odot}$ is a solar mass). The companion star transfers matter from its hydrogen-rich envelope through the Roche-lobe overflow to the WD. The scenario has three cases by the accreting rate ($\dot{M}$) of the WD from the companion star. First, in the case of high accreting rate of $\dot{M} > 3 \times 10^{-6} M_{\odot}\ \ \mathrm{yr}^{-1}$, the accreting matter escapes from the WD, since the temperature becomes too high. On the other hand, in the case of low rate of $\dot{M} < 1 \times 10^{-8} M_{\odot}\ \ \mathrm{yr}^{-1}$, the accreting matter also escapes, due to small explosions on the surface. In the case of $1 \times 10^{-8} M_{\odot} < \dot{M} < 3 \times 10^{-6} M_{\odot}\ \ \mathrm{yr}^{-1}$, the accreting matter can be accumulated on the WD, and burns without ejection of hydrogen. When the total mass of the WD exceeds the Chandrasekhar limit of $1.4M_{\odot}$ and its central density reaches to $\sim 3 \times 10^{9} \mathrm{g/cm^3}$, the explosive carbon ignition is triggered at the center of the WD. The carbon-burning front propagates outward, and nuclear burnings, such as silicon, oxygen and neon, begins behind the front. Then ignitions produce heavier elements such as Fe, Ni, Ca, Ar, S, Si and so on, and the total explosion energy and the ejecting mass are estimated to be $\sim 1.3 \times 10^{51}$ erg and $\sim 1.4M_{\odot}$, respectively. Light curves for all of type-Ia SNe are very similar to each other, showing a rapid rise to maximum brightness, and staying at maximum for a short time, fading by 3 magnitudes in 30 days and decreasing ~ 0.015mag/day after 50 days.

- **Type-II Supernova**

Most of Type-II SNe are found in spiral galaxies, particularly in the spiral arms, where star formations are active (i.e. sites of massive stars), and not observed in early type galaxies, which consist of old type stars and little cold gas. These observational facts indicate that the progenitors of type-II SNe are early type stars. Type-II SNe is explained as a gravitational collapse of massive stars. This scenario was confirmed by the detection of the huge neutrino burst from SN 1987A, since a neutrino burst had been considered to be during the collapse of the iron core to the neutron star. At the last phase of the massive star ($M > 8M_\odot$) evolution, the iron core is formed at the center of the star, which is supported by the degeneracy pressure of the electrons. When the temperature of the iron core exceeds $\sim 10^{10}$ K the endothermical decompositions of ^{56}Fe occurs by electron-capture reactions.

$$^{56}\mathrm{Fe} + \mathrm{e}^- \rightarrow {}^{56}\mathrm{Mn} + \nu_e - 3.7\mathrm{MeV} \tag{2.4}$$

Thus, the number of electrons is reduced and then the degeneracy pressure becomes low. At the same time, the following degeneration of the Fe begins;

$$^{56}\mathrm{Fe} \rightarrow 13\mathrm{He} + 4\mathrm{n} - 124.4\mathrm{MeV}. \tag{2.5}$$

Immediately, the gravitational collapse begins, since the core cannot support itself by the inner pressure. During the collapse, the density of electrons increases. Finally the electrons are squeezed into the nuclei, and change to heavier neutron-rich isotopes. When the central density exceeds $2.7 \times 10^{14}\mathrm{g/cm}^3$, the central core becomes possible to support itself due to the degeneracy pressure of neutrons collapsed from matters. At the surface of the core, the further collapsing matter is bounced back and a strong outgoing shock wave is produced. If enough energy is provided to the shock, the further collapsing matter is blown away with the kinetic energy of $\sim 10^{51}$ erg. In addition, the central core becomes a neutron star (or a black hole).

After the explosion, the huge energy of the explosion affects the surrounding matters. The circumstellar and interstellar medium (CSM and ISM, respectively) are heated by the shock wave of the explosion, and observed as supernova remnants (SNR) for a long time in the interstellar space. From their appearance, SNRs are classified into two types, shell-like and prelions. Examples of the former are Cassiopeia A (Cas A, Figure 2.3 and Cygnus Loop. The prototype of the latter is Crab nebula (Figure 2.4), and therefore, prelions are also called a Crab-like SNR.

- **Shell-like SNR**

  The shock wave, when propagating through either the ISM, the CSM or the ejecta of SN provides almost all their energies to them. The ions and electrons in the medium are heated

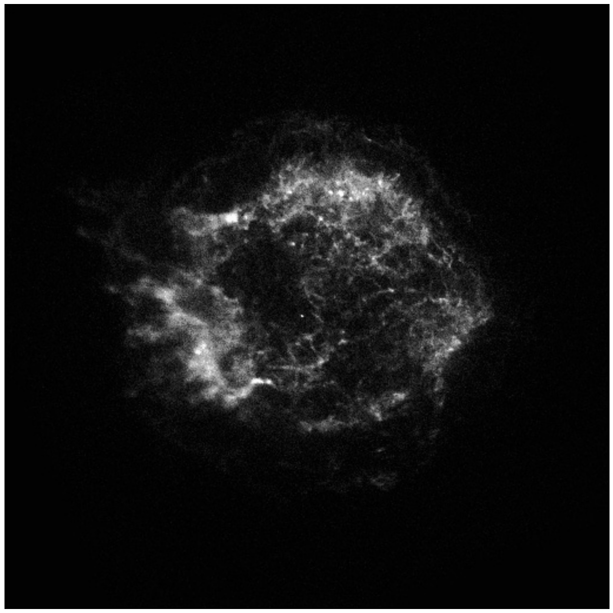

Figure 2.3: Image of Cassiopeia A obtained by *Chandra* [88].

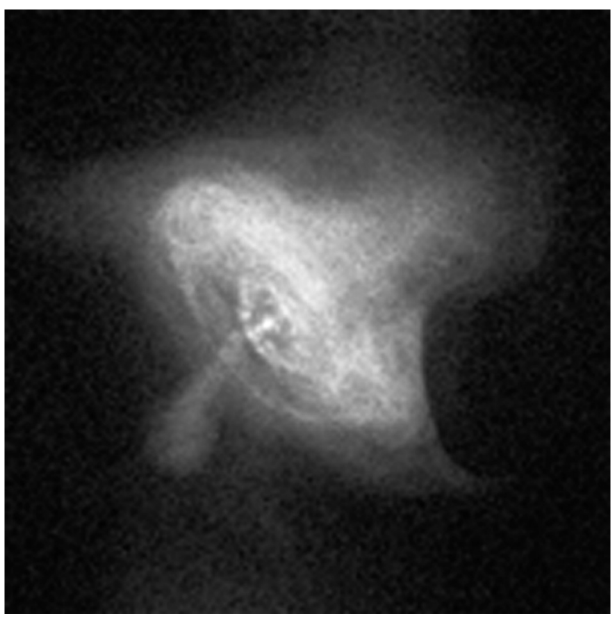

Figure 2.4: Image of Crab pulsar/nebula obtained by *Chandra* [89].

to the thermal plasma particles by the shock wave up to $\sim 10^7$K. The bremsstrahlung emissions from above plasma are observed in the X-ray with emission lines. In the front of the shock wave, the magnetic field in the plasma is frozen, and particles are assumed to be accelerated non-thermally. As an acceleration mechanism, First-order Fermi acceleration is widely supported. The spectra observed in the radio will indicates the feature of synchrotron spectrum emitted from the electrons accelerated by this mechanism.

- **Crab-like SNR**

  As mentioned above, type-II SNe leave the neutron stars (or black holes) after the explosion. When the neutron star spins rapidly and contains the strong magnetic field, it emits pulsating radio, X-ray and gamma-rays, which is called a pulsar. A pulsar often accompanies a nebula with a center filled morphology. Sometimes pulsars are the energy source of SNR, and release their energies by spinning down to surrounding nebula through radiation.

2.3 Shock Acceleration

The spectra of the shell-like SNRs in the radio are typically observed as a power-law with the index of ~ -0.5, which indicates the existence of non-thermal high-energy electrons with a power-law distribution. In shell-like SNRs, the first-order Fermi acceleration in the shock wave is considered to be effective in the acceleration of electrons [7] [2].

Here, consider the case that a relativistic particle having the kinetic energy of E_0, passes through the non-relativistic shock wave from the upstream to the downstream. The velocities of the shock in the upstream and the downstream, are defined v_{u} and v_{d} , respectively.

The particle is scattered elastically in the downstream, and its energy changes to E'_0 as following;

$$E'_0 \simeq \gamma_{\mathrm{d}}^2 (1 - \beta_{\mathrm{d}}^2) E_0 \tag{2.6}$$

where $\beta_{\mathrm{d}} \equiv v_{\mathrm{d}}/c$ and $\gamma_{\mathrm{d}} \equiv \sqrt{1-\beta_{\mathrm{d}}^2}$. Subsequently, the particle is also scattered in the upstream side, its energy changes again;

$$E_1 \simeq \gamma_{\mathrm{u}}^2 (1 + \beta_{\mathrm{u}}^2) E'_0 \simeq (1 + 2\beta_{\mathrm{u}})(1 - 2\beta_{\mathrm{d}}) E_0 \tag{2.7}$$

where β_{u} and γ_{u} are defined in the same way of β_{d} and γ_{d}, respectively. The particle can gain energy by repeating the scattering in both upstream and downstream, due to $\beta_{\mathrm{u}} > \beta_{\mathrm{d}}$ in the shock wave. In the 3-dimensional space, the velocity direction of the scattered particle is isotropic, and its energy gain is reduced compared to the above 1-dimensional case. The average energy of the particle after n rounds is calculated as follows;

$$\langle E_n \rangle = E_0 \mathrm{e}^{\frac{4}{3} n (\beta_{\mathrm{u}} - \beta_{\mathrm{d}})}. \tag{2.8}$$

Here, assuming that the direction of the particle in the shock wave becomes isotropic in the scattering process, due to the turbulences and lots of scatterings in the stream, the average velocity of the scattered particle is equal to the stream velocity of the shock wave. Then the particles scattered to the upstream side are let return back to the shock front. On the other hand, for the particles scattered to the downstream, the probability to escape from the shock wave, η is described as follows;

$$\eta = 4\frac{v_{\rm d}}{v_0} \tag{2.9}$$

where v_0 is the velocity of the particle. Therefore, the probability of the particle to repeat the round for n times is calculated to be

$$P_n = (1 - 4\beta_{\rm d})^n. \tag{2.10}$$

From the equations 2.8 and 2.10, the differential spectrum of the accelerated particles by the shock wave is estimated to be

$$N(E) \propto \frac{dP_N}{dE_n} \propto E^{-\frac{\beta_{\rm u}+2\beta_{\rm d}}{\beta_{\rm u}-\beta_{\rm d}}}. \tag{2.11}$$

Especially in the case of the strong shock of the ideal mono-atomic gas, $\beta_{\rm d} = \frac{1}{4}\beta_{\rm u}$, we obtain the typical spectrum;

$$N(E) \propto E^{-2}. \tag{2.12}$$

Thus, the mechanism of the first-order Fermi shock acceleration can accelerate the particles to have the power-law spectrum with the index of -2, and well explain the observation in the radio. In addition, due to no distinction between ions and electrons for the acceleration and very high efficiency of the acceleration this mechanism is assumed to have an important part in the SNRs as the origin of cosmic-rays.

2.4 Cosmic-Ray Origin

Cosmic-rays are the relativistic particles propagating in the universe. We cannot find the site of the cosmic-ray origin from the coming direction of the cosmic-rays, since the Lorentz force generated in the interstellar magnetic field bends the tracks of the cosmic-rays.

Although many kind of nuclei or electrons are observed in comic-rays, almost all of them are protons. The energy range of the observed protons is distributed widely between 10^9eV and over 10^{20}eV (the lower limit is due to the effect of the solar wind). The integral energy spectrum of the flux extends to the energy around 10^{15} eV, called the "knee" region, with single power-law of ~ -1.7 index, and changes its index to ~ -2.1 around the knee (Figure 2.6). With the typical magnetic field of $\sim 3\mu$G in the Galactic plane, the Larmor radius of the proton with the energy below 10^{12} eV is less than the thickness of the Galactic disk of ~ 300 pc, and the protons are

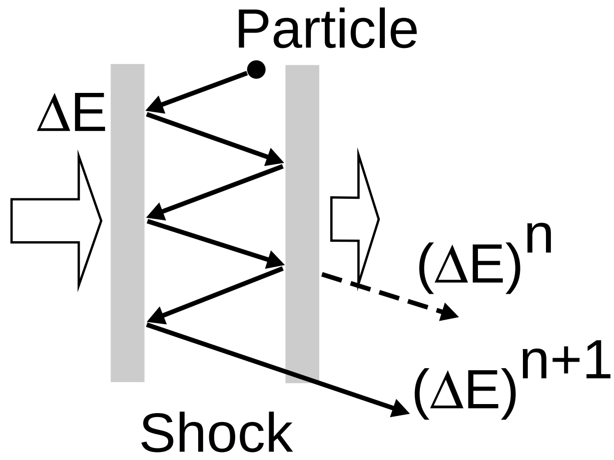

Figure 2.5: Schematic of the shock acceleration.

bound in the Galaxy. However, for energies over 10^{15} eV, the protons escape out of the Galaxy, then this indicates the observed break of the cosmic-ray spectrum, "the knee", and the origins of the cosmic-ray with below 10^{15} eV are assumed to be in the Galaxy.

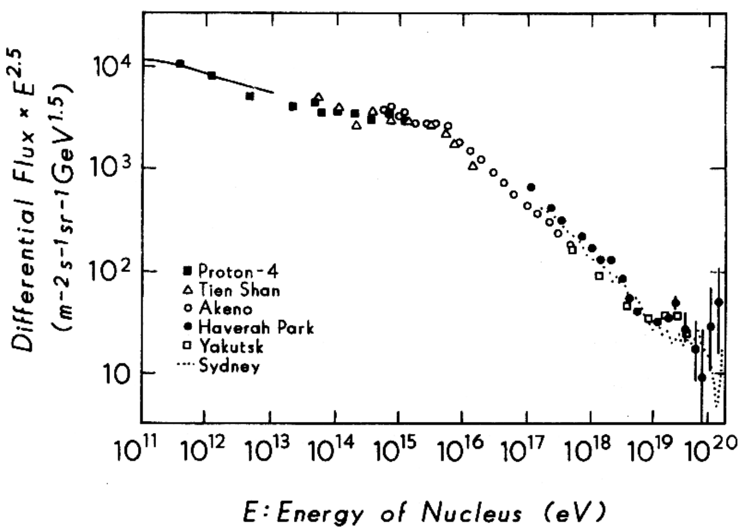

Figure 2.6: Energy spectrum of cosmic-ray protons [64]. The horizontal axis is energy (eV), and the vertical is Flux $\times$ energy$^{2.5}$.

The energy density of cosmic-rays is known to be $\sim$ 1eV/cm^3, and its mean lifetime is estimated to be $\sim$ 20 million years by the observed flux of the radioisotope ^{10}Be. Here, assuming that the Galaxy has the diameter of 30kpc and the disk thickness of 300pc, the total energy in the Galaxy is estimated to be $\sim 10^{54}$ eV. From the mean lifetime of cosmic-rays, the energy supply of $\sim 10^{40}$eV/sec is necessary to sustain comic-rays in the Galaxy. This huge energy budget is assumed to be supplied only by SN explosion. Since one SN explosion occurs every 30 years in the typical spiral galaxy, and its energy reaches $\sim 10^{51}$ eV as mentioned in chapter 2.2, the energy supply rate from the SNe is estimated to be $\sim 10^{42}$eV/sec. Several percents of this energy can cover the supply for the cosmic-ray acceleration. The radio synchrotron emission from SNRs, which is radiated from the electrons of $10^8 \sim 10^9$ eV in $\sim 3\mu$G of the typical magnetic field in the Galactic plane, indicates the cosmic-ray acceleration in the SNRs. In addition, the first-order Fermi acceleration seems to explain the power-law spectrum of cosmic-rays. However the observational evidence for particles accelerated to the energy over 10^9 eV in any SNR was not found until recently.

2.5 Preview of SN1006

SN1006 (G327.6+14.6) is a remnant of the brightest supernova in the history, of which explosion was observed in A.D.1006. Its explosion was recorded everywhere in the world, in diaries, chronicles and official records, as a new star in Europe, a guest star in Asia. This supernova had been observed to be brightened for more than 7 months. The light curve estimated from above records indicates this supernova to be type-I SN, since the light curve of type-II SN declines faster than this light curve [44]. In addition, strong Fe^+ resonance absorption lines were found from the observation of the present SN1006 remnant in the UV band [80], which strongly supports that SN1006 is a type-Ia SN. From the 11cm-radio observation, it was found that the remnant has a shell-like structure, and the index of the energy spectrum is ~ -0.6 [8] [58]. There exists two bright rims (north-eastern and south-western quadrant) symmetrically along the outer circle of the remnant with a diameter of 30 arcmin [59].

In the optical wavelength, an Hα filament was detected [85], and from the observation of the Balmer-line broad component, the shock velocity was inferred in the range $2800 \sim 3900$km/sec [26], using the non-radiative shock model [4]. Using the mean proper motion of the filament of 0.30 ± 0.04arcmin/yr [32], the distance to SN1006 was estimated to be $1.7 \sim 3.1$ kpc.

The energy spectrum observed in radio is represented as a power-law with the index of ~ -0.6, which is similar to the other shell-like SNR such as Tycho, Kepler and Cas A. Thus, observed spectra of SN1006 in radio and optical show that it is one of typical shell-like SNRs. However, X-ray observation of SN1006 revealed unexpected feature. Generally, the X-ray emission from shell-like SNRs is considered due to bremsstrahlung process in the thermal plasma of the ISM heated by the shock, where strong emission line are usually observed. On the other hand, the energy spectrum of SN1006 shows featureless structure over a wide energy band, with a few very faint emission lines.

In the energy spectrum of the rim-region of SN1006 observed with the SSS (the Solid State

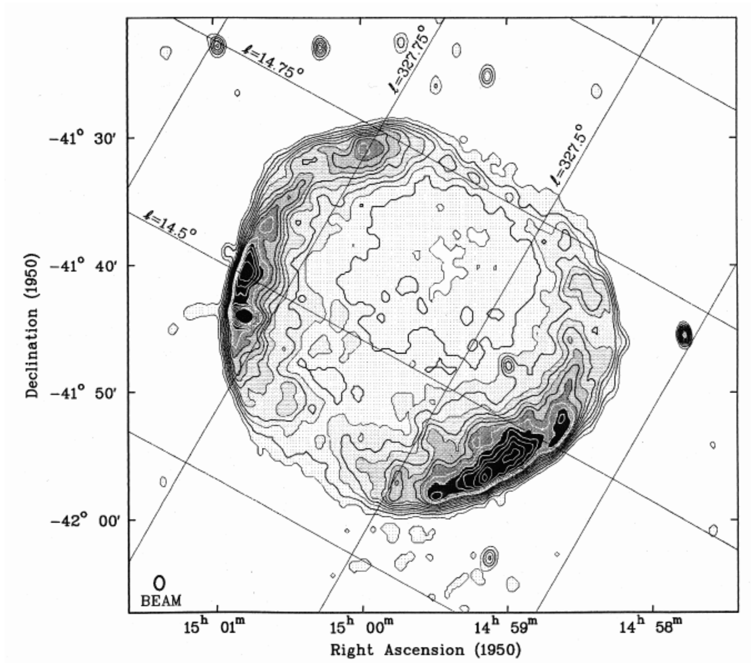

Figure 2.7: SN1006 in radio (845MHz). There exists two bright rims (north-eastern and south-western quadrant), which face each other symmetrically with the apparent diameter of 30 arcmin [59].

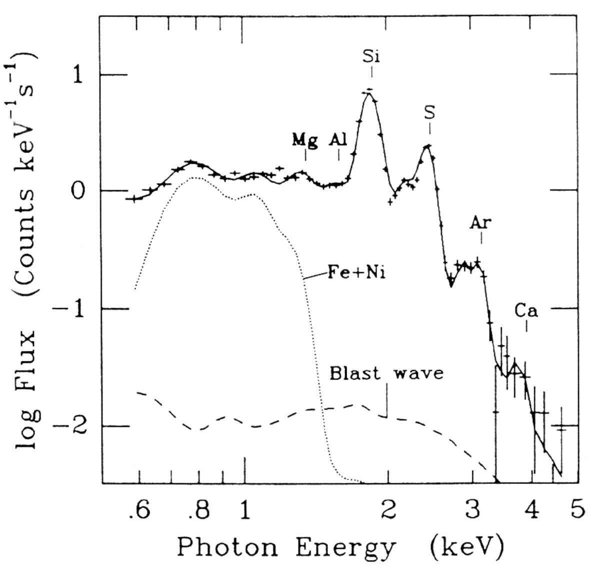

Figure 2.8: X-ray spectrum of the typical shell-like SNR (Tycho). There exists some emission line by the thermal plasma.

Spectrometer) on the *Einstein*(HEAO-2), there does not exist the Si emission line, which should appear the usual shell-like SNR. In addition, the observation with the CXS (Cosmic X-Ray Spectroscopy) on the *OSO-8* (Orbiting Solar Observatory) shows the spectrum with the index of -1.2 [1]. These fact: the absence of the Si emission line and the energy spectrum represented by a single power-law with a photon index of -2.2, had indicated the non-thermal origin similar to the synchrotron emission observed e.g. in the Crab nebula. However, the evidence for the

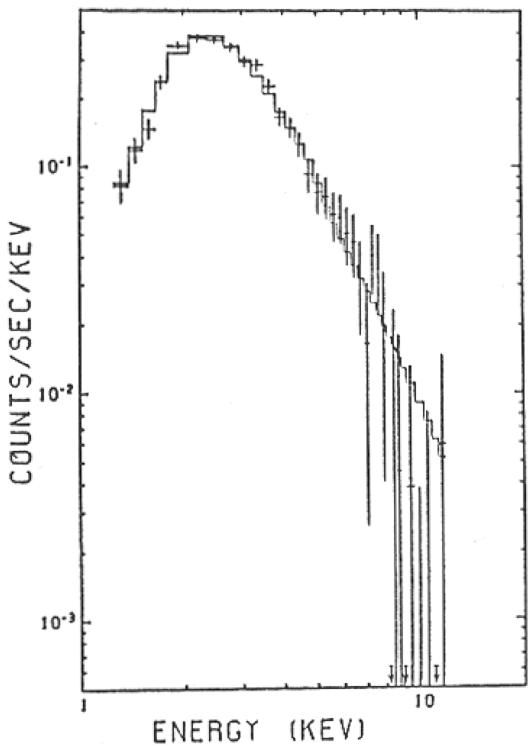

Figure 2.9: X-ray spectrum observed by *Tenma*. The energy spectrum was represented by a single power-law with the index of -2.2 [27].

thermal emission origin was also found by the observation of the K-emission lines from highly ionized oxygen (O VII, O VIII) [76]. On the other hand, *Tenma* observed X-rays from the Lupus Loop, whose location overlaps SN1006. The Lupus Loop is a very old SNR, of which age and distance are 10^4 years and $0.5 \sim 1.0$ kpc, respectively, and its size is ~ 270 arcmin radius. After the subtraction of the local background due to the Lupus Loop, it was found that the spectrum in the hard X-ray has an index of -2.2, which is steeper than that of typical synchrotron nebula [27].

Two models based on the multi-temperature, thermal plasma model and the first order Fermi shock acceleration, were investigated in order to explain the observed power-law spectrum and the absence of emission lines. The observation by *ASCA* provided an answer which gives an important result on cosmic-ray origin [28] [51].

ASCA had four X-ray detectors: two Solid state Imaging Spectrometer (SIS) and two Gas Imaging Spectrometer (GIS). The SIS had good energy and position resolutions, and the GIS has a wide field of view and a high sensitivity in the hard X-ray.

The GIS image shows the structure of the shell-like SNR consistent with the observation in radio, of which two bright rims of the NE and SW face each other. In the analysis, the region of the GIS image was divided to some pieces, and the spectrum in each region was obtained individually.

The results are: emission lines were not found in the two rim-regions, whereas strong emission lines of highly ionized Ne, Mg, Si and S were found in the residual regions. This result shows the existence of the thin-thermal plasma in SN1006 similar to other shell-like SNRs.

The observations for a part of the NE-rim and the center using the SIS, also gave the spectra consistent with the GIS result. The spectrum of the center region was fitted by the non-equilibrium ionization(NEI) plasma model, and the metal abundance obtained is equivalent to that of typical shell-like SNRs. On the other hand, the spectrum of the rim-region could be fitted well by a power-law with the index of -1.95 ± 0.20 together with the emission line of O VII and O VIII. Instead of the power-law function, the bremsstrahlung emission model was examined and rejected by fitting.

These results show that thermal X-rays are emitted from the whole region of the remnant, and also there exists the component of non-thermal strong emission in the rim-region of the remnant. Moreover, morphological consistency between the region bright in X-ray and that in radio, strongly support the synchrotron emission due to high-energy electrons, which are accelerated around the shock.

If the emissions from the rim were of synchrotron origin, the energy of the source electrons can be estimated, assuming the value of the magnetic field. Using the above method and the magnetic field of $B = 6 \sim 10\mu$G estimated by the theoretical model [57], the maximum electron energy is calculated to be ~ 100 TeV, which is close to the knee energy. This result of *ASCA* is the first observational evidence supporting that the SNRs are the sites of the comic-ray origin.

High energy electrons of ~ 100 TeV can produce also TeV gamma-rays through the inverse Compton scattering of 2.7K cosmic micro-wave background photons. After the discovery of the high-energy electrons by *ASCA*, the possibility of TeV gamma-ray emission was suggested [33] [34] [53] [81]. Soon, the CANGAROO group, as described in chapter 4.1, looked for TeV gamma-rays from SN1006 using the CANGAROO 3.8m telescope, and the significant signals of TeV gamma-rays were found from the non-thermal shell of the NE-rim [68]. Since the gas density in SN1006 is exceptionally small, it is assumed that the TeV gamma-rays are not due to π^0 decay, but due to the IC process. This discovery of the TeV gamma-rays undoubtedly indicate the existence of ~ 100 TeV electrons and the Fermi shock acceleration. The flux of the

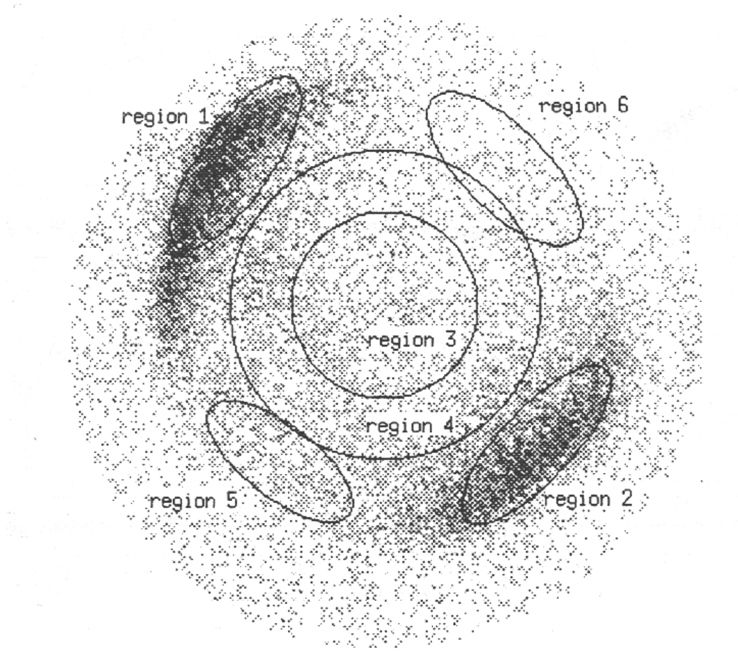

Figure 2.10: X-ray image of SN1006 observed by *ASCA*/GIS [51]. It appears the structure of the shell-like SNR consistent with the observation in radio, in which two very bright rims of the NE and SW face each other. The picture also shows the 6 regions for the spectrum analysis.

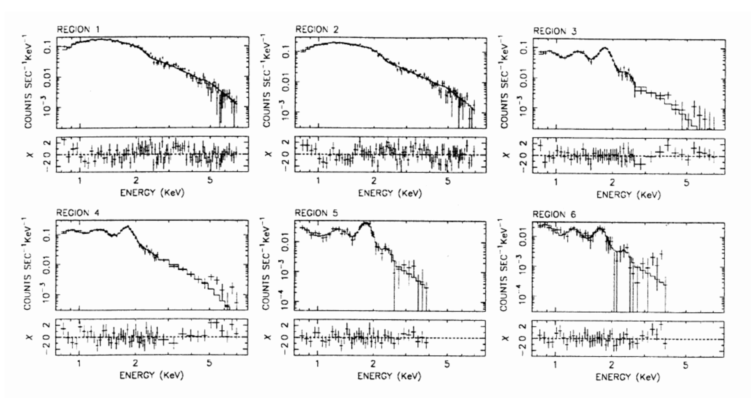

Figure 2.11: X-ray spectra of SN1006 observed by *ASCA*/ GIS . The regions correspond to those in Figure 2.10. The region 1 and 2 of the rim-regions have no emission lines, however there exist some emission lines in the other regions. The spectra of the rim-regions and the others were fitted by the single power-law and the thermal bremsstrahlung model with 4 Gaussian functions for the emission lines, respectively [51].

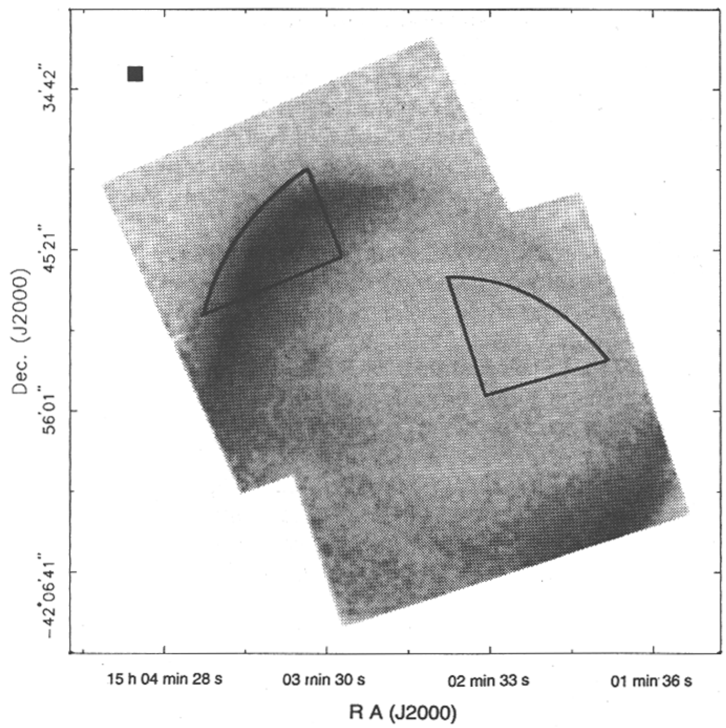

Figure 2.12: X-ray image of SN1006 observed by *ASCA*/SIS [28]. The structure of the SIS image is consistent with the GIS image. Two regions were analyzed for their spectra.

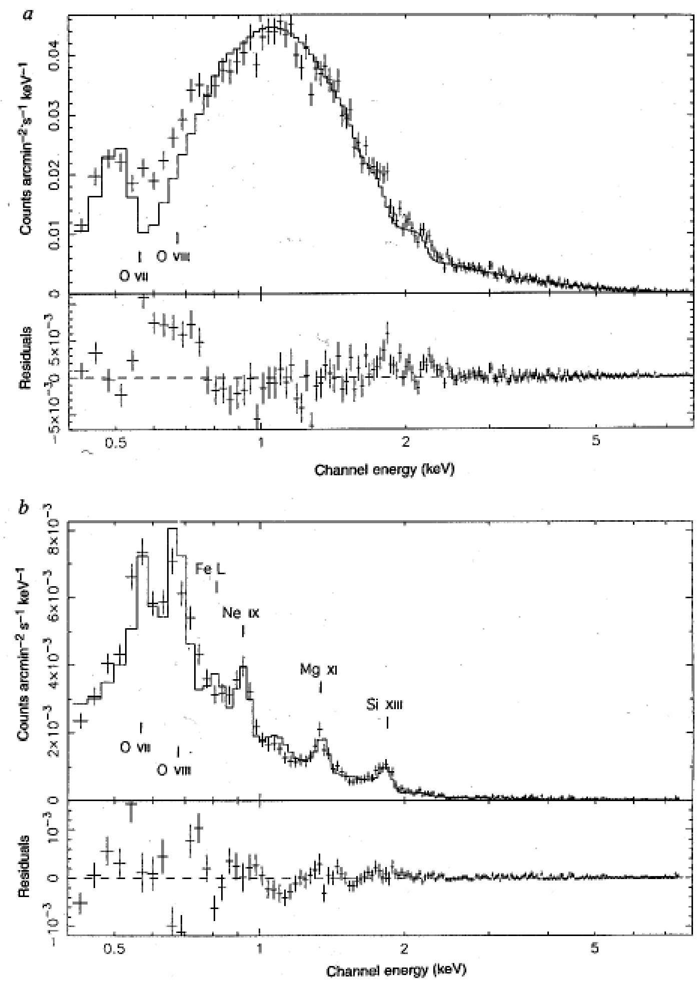

Figure 2.13: The X-ray spectra of SN1006 observed by *ASCA*/SIS . The upper figure is the spectrum of the NE-rim, which is represented by the power-law with the index of -1.95 ± 0.20 and two emission lines of 0.574(O VII) and 0.653(O VIII) keV. The lower is that of the center region, which shows several strong emission lines, and was fitted by the NEI model. [28].

TeV gamma-ray was estimated to be $(4.6 \pm 0.6_{\rm stat} \pm 1.4_{\rm sys}) \times 10^{-12}{\rm cm}^{-2}{\rm sec}^{-1}$ ($E_\gamma > 1.7 \pm 0.5$ TeV) and $(2.4 \pm 0.5_{\rm stat} \pm 0.7_{\rm sys}) \times 10^{-12}{\rm cm}^{-2}{\rm sec}^{-1}$ ($E_\gamma > 3.0 \pm 0.9$ TeV). Combining the IC model for the TeV gamma-ray with the synchrotron emission for the non-thermal X-ray observed by *ASCA*, the magnetic field is uniquely determined to be 6.5μG.

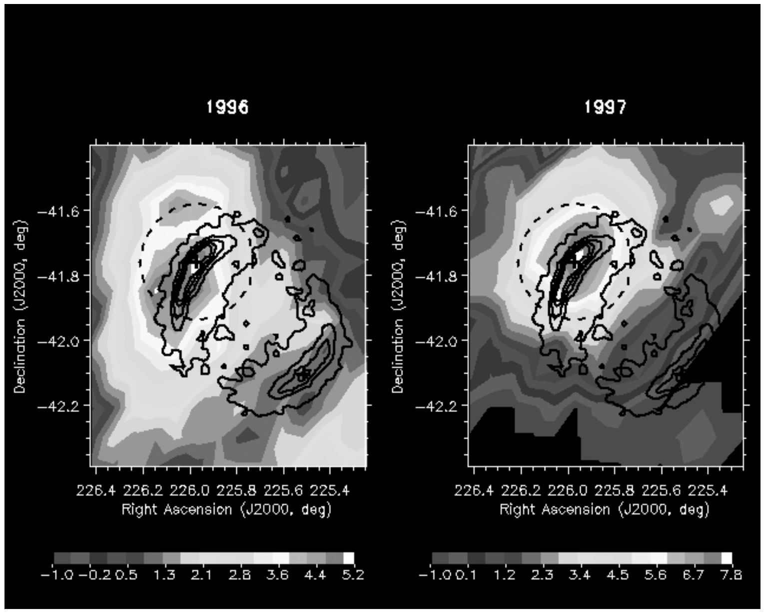

Figure 2.14: Significance map around SN1006 observed by the CANGAROO 3.8m telescope. The contour map of the statistical significance for various positions in the sky around SN1006 [68]. The hard X-ray fluxes of the *ASCA*/GIS are also overlaid as solid-line. The maximum flux point of each rim in the X-ray of the range $2 \sim 10$ keV is marked by a cross. The dashed circle is the point spread function(PSF) of the CANGAROO 3.8m telescope. The left map is observed in 1996 and the right is that in 1997, respectively.

Chapter 3

Detection of VHE Gamma-Rays

3.1 Extended Air-Shower

Cosmic high energy protons and gamma-rays come to the top of Earth atmosphere. They interact with air nuclei, and initiate many secondary particles. This phenomenon is called Extensive Air Shower (EAS).

When a gamma-ray with greater than 10 GeV is injected to the atmosphere, it causes at first the pair creation of electron and positron. The electron and positron produce photons via bremsstrahlung radiation. By such processes repeating, the secondary electrons and photons increase exponentially. They are known as the electromagnetic cascade. The energy of primary gamma-ray is divided to secondary particles via the electromagnetic cascade, and these secondary particles lose their energy by ionization. When the energy of a particle decreases less than the critical energy, no new particles can be created and the cascade will stop. The critical energy is the energy when energy loss by electromagnetic process of pair creation and that by bremsstrahlung are equal to the ionization loss energy, and is 81 MeV for the atmosphere.

On the other hand, when a nucleus or a proton is injected, the EAS consists of not only electromagnetic cascade but also nuclear cascade, generating secondary particles via nuclear interaction with atmospheric nuclei. Several kind of particles are generated in nuclear cascade, such as nuclei (proton, neutron, ...), mesons (pion, kion, ...), leptons (electron, positron, muon), in which pion is a major part of nuclear cascade secondaries. The neutral pion, due to its short lifetime (0.83×10^{-16}[sec]), immediately decays into two gamma-rays which initiate electromagnetic cascade.

$$\pi^0 \rightarrow 2\gamma \tag{3.1}$$

The lifetime of charged pion is 2.603×10^{-8}[sec]. Due to relativistic effect, the pion with greater than 10 GeV interacts with atmospheric nuclei before decaying, and initiates the development of EAS, while a lower energy charged pion decays to a muon and a neutrino before secondary interaction.

$$\pi^+ \rightarrow \mu^+ + \nu_\mu \tag{3.2}$$

$$\pi^- \rightarrow \mu^- + \bar{\nu_\mu} \tag{3.3}$$

Thus, the development of EAS is different for the kinds of the primary particles. Let us consider it from the following three perspectives. At first, the profiles of EAS differ between gamma-ray and nucleus. An EAS initiated by gamma-ray grows symmetrically and concentrates around the direction of the primary gamma-ray injection, because an electromagnetic cascade has no particles which bring the transverse momentum. On the other hand, a nuclear EAS has broad and asymmetrical distribution, since secondary particles generated by nuclear cascade bring the large momentum to the transverse direction. The second difference of the EAS is the height of EAS development. Since the nuclear interaction length is longer than the radiation length, a hadronic EAS begins in the lower atmosphere than the case of the gamma-ray EAS. The third difference is the number of secondary particles. In a hadronic EAS, secondary π^+, π^-, π^0 are produced isotropically. Therefore, the electromagnetic part of the hadronic EAS, which are generated by π^0 decay, is roughly one third of an gamma-ray EAS with the same initial energy.

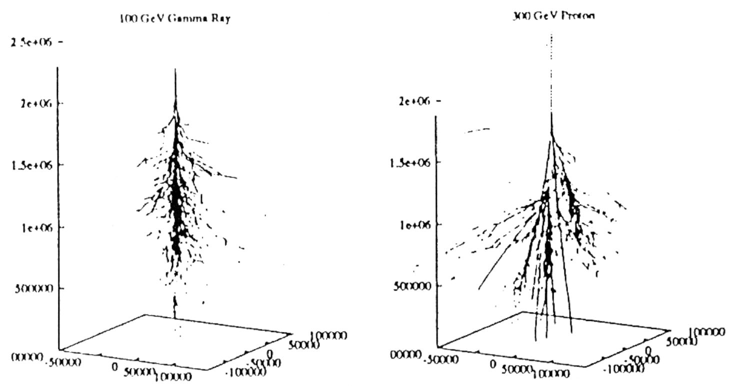

Figure 3.1: Development of EAS (simulation) [71]. The left figure is an EAS by 100 GeV gamma-ray, and the right is by 300 GeV proton. A lot of fluctuations appear in the proton EAS.

3.2 Čerenkov Radiation

The light velocity in a medium of refractive index n is reduced to c/n, where c is the light velocity in the vacuum. When a charged particle moves in the medium at the velocity v faster than c/n, it causes the polarization of medium along the particle track, and this polarization radiates photons into the forward cone, of which opening angle θ is defined with respect to the moving direction of the charged particle. This angle is known as Čerenkov angle, and written by using the velocity of the charged particle and the refractive index as follows;

$$\cos\theta = \frac{1}{\beta n}, \qquad \beta = \frac{v}{c}. \tag{3.4}$$

The output energy of Čerenkov radiation per unit path length by a particle with charge Ze can be expressed as;

$$-\frac{dE}{dx} = \frac{Z^2e^2}{c^2}\int_{\beta n \geq 1}\left(1 - \frac{1}{\beta^2 n^2}\right)\nu d\nu, \tag{3.5}$$

where ν is the frequency of Čerenkov radiation. From the above equation, the number of Čerenkov radiated photons N into the wavelength range from λ_1 to λ_2 is written as follows;

$$\begin{aligned} N &= \int_{\lambda_1}^{\lambda_2}\frac{1}{\hbar\omega}d\lambda\int_0^{\ell}\left(-\frac{dE}{dx}\right)dx \\ &= 2\pi\alpha\ell Z^2\left(\frac{1}{\lambda_1} - \frac{1}{\lambda_2}\right)\left(1 - \frac{1}{n^2\beta^2}\right) \end{aligned} \tag{3.6}$$

$$\alpha = \frac{e^2}{\hbar c} \simeq \frac{1}{137} \tag{3.7}$$

where α is the fine structure constant and l is the path length of the charged particle. From this equation, for a relativistic electron traveling a length of 1 m, 27 Čerenkov photons are radiated into the wavelength range from 350 nm to 550 nm.

In the EAS, charged secondary particles radiate Čerenkov photons. For the refractive index of atmosphere at 1 atm (on the ground) of $n \sim 1.00029$, and for the velocity of the relativistic particle, Čerenkov angle θ is 1.4 degree according to equation (3.4). Also, the threshold energies for Čerenkov radiation are calculated to be 21 MeV for electron, and 4.3GeV for muon, respectively. The refractive index of air is related to the air density ρ, and decreases as the altitude h increases;

$$n(h) = 1 + 2.9 \times 10^{-4}\rho(h), \tag{3.8}$$

$$\rho(h) = \rho_0 \cdot \mathrm{e}^{-\frac{h}{H}}, \tag{3.9}$$

where H is 7.1 km, and ρ_0 is the air density on the ground (1 atm). In addition, the effect of the multi-Coulomb scattering of charged particles in the EAS spreads the distribution of Čerenkov photons to a few degrees along the EAS axis. The distribution of Čerenkov photons on the ground reflects on the variation of the EAS development.

The number of Čerenkov photons emitted from hadronic EAS is roughly one third of that from gamma-ray EAS, due to the charge symmetry of $\pi^{\pm}$, π^0. Moreover, the distribution of Čerenkov photons has large fluctuation, because the energy and the generation altitude of pions fluctuate event by event. For a gamma-ray EAS, the lateral distribution of Čerenkov photons at the sea level is extended over a radius of 500 m and the core part within ~150 m radius looks uniform (Figure 3.2). The number of secondary particles in the EAS generally reaches at the maximum around the altitude of ~ 10km with little dependence on its initial energy, and also the emission angles of Čerenkov photons are collimated within one degree. These facts indicate that the area where the Čerenkov photons are spread, is estimated to be of the order of 10^4 m^2 independent of its initial energy, which is much larger than the typical detection area of the satellite of ~ 1m. In addition, since the distribution of Čerenkov photons on the ground is uniform, and its size is almost constant, the amount of Čerenkov photons obtained by the telescope becomes a good estimator for the primary energy of gamma-ray.

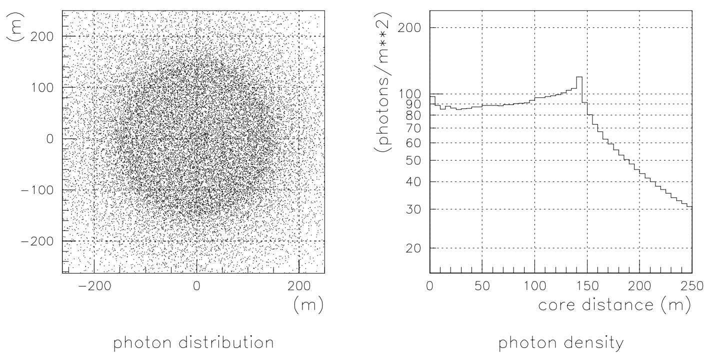

Figure 3.2: Density distribution of Čerenkov photons by a 1 TeV gamma-ray EAS (simulation). The right graph shows that the density is essentially flat within 150 m from the EAS axis.

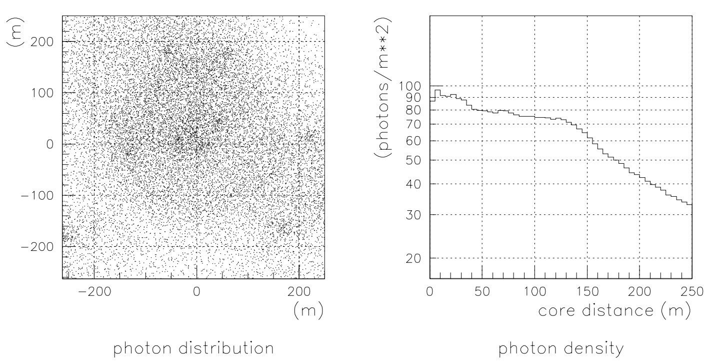

Figure 3.3: Density distribution of Čerenkov photons by a 3 TeV proton EAS (simulation).

3.3 Imaging Method

3.3.1 Imaging Technique

The flux of gamma-ray emitted from a strong celestial source such as the Crab pulsar/nebula is typically $\sim 10^{-11}\text{cm}^{-2}\text{sec}^{-1}$ above 1 TeV, while the flux of the cosmic-ray (as background) is $\sim 10^{-5}\text{cm}^{-2}\text{sec}^{-1}\text{str}^{-1}$ above the same energy. Even assuming a small effective field of view of a telescope with 1 degree radius ($\sim 10^{-3}$str), the signal-to-noise ratio in the detected events is estimated to be $\sim 10^{-3}$. In order to detect such a faint gamma-ray signals efficiently, an effective reduction of the background events is inevitable.

In early days (1960's), the VHE gamma-ray observation was made using a camera in which several PMTs were set on the focal plane. The signal was obtained as the residual of subtracting the number of background events from the number of events of source direction (ON-OFF chopping method). This measurement had the angular resolution of only $\sim$ 1 degree, because of no-imaging ability of the camera. In 1990's, with the appearance of the "imaging technique" described later, a good angular resolution of $\sim$ 0.1 degree was obtained. Furthermore, this technique has provided a powerful reduction of background, and the signal-to-noise ratio was improved by about 100 times better than before.

The principle of imaging technique is schematically shown in Figure 3.4. The Čerenkov

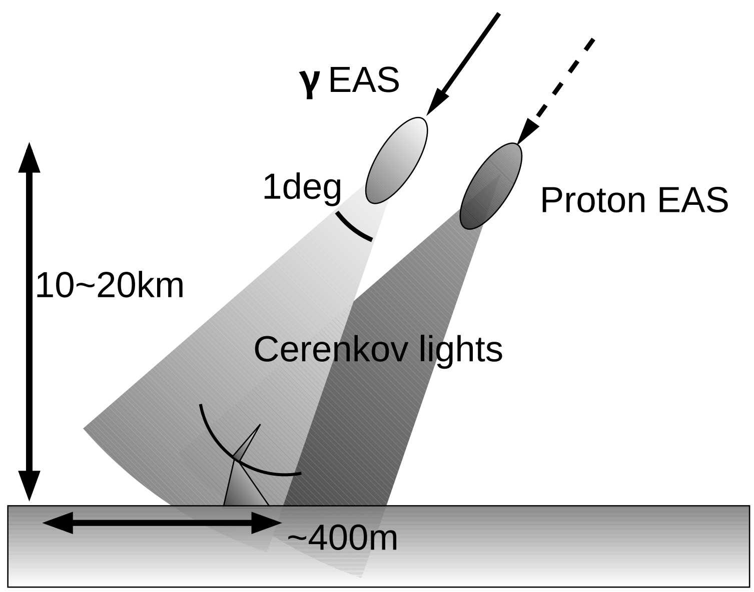

Figure 3.4: Principle of VHE gamma-ray detection. The image of Čerenkov photons from EAS measured with the imaging-camera of telescope represents the shape of the electromagnetic cascade. This image is elongated along the EAS axis in the direction to the source position of the primary gamma-ray.

photons collected by the reflector of the telescope make an image on the focal plane. This image is a projection of the EAS development onto the focal plane and elongated along the EAS axis. In the case of the gamma-ray EAS, it develops and concentrates along the axis, and hence the image becomes a clear ellipse. In addition, the major axis of this elliptical image points toward the gamma-ray source in the field of view.

On the other hand, for the cosmic-ray EAS, its image becomes broader than that of gamma-ray, due to its irregular development. Cosmic-rays propagating to the Earth are scattered by interstellar magnetic field, and then the primary direction of cosmic-rays on the earth is isotropic. Since the image reflects the primary direction and the irregularity of EAS development, the major axis of hadronic EAS is perfectly at random.

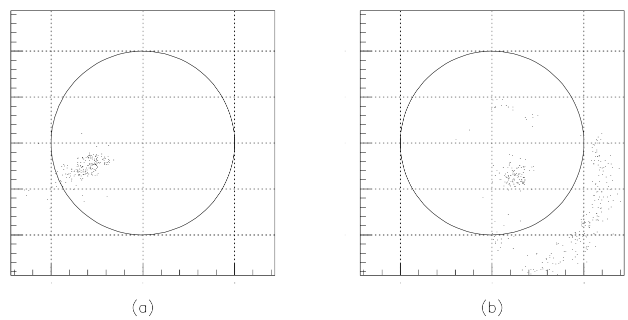

Figure 3.5: Typical EAS images on the focal plane (simulation). (a) is the case of 1 TeV gamma-ray injected from the direction of camera center. (b) is the case of 3 TeV proton injected in random direction. The gamma-ray image is compact and sharp in comparison to the broad and scattered image of proton. The circle in the figure indicates the field of view of 3 degree.

By the appearance of the imaging technique, it was found that the difference between gamma-ray and cosmic-ray images in the detector is essential in the background reduction, where Čerenkov photon images are measured by a fine pixel detector such as an assembly of small photo-multiplier tubes (PMTs).

Hillas(1985) argued the effectiveness of the parameterization based on fitting an ellipse to the Čerenkov photon images, and extracted the characteristics required to enhance gamma-ray signals [16]. In early 1990, Whipple observatory and The CANGAROO group detected TeV gamma-ray signals using this technique independently. These results proved that the imaging technique is essential. Consequently, the imaging technique has been widely used in detecting gamma-rays in the TeV energy region. The image parameters generally used in the imaging technique are schematically shown in Figure 3.6, and summarized bellow.

- **Width;** the root mean square (RMS) spread of Čerenkov photon image along the minor axis, a measure of the lateral development of the EAS.

- **Length;** the RMS spread along the major axis, a measure of the vertical development of the EAS.
- **Distance;** the distance between the centroid of the image and the source position.
- **Distance′;** The distance between the centroid of the image and the center of field of view.
- **Conc;** The parameter representing the concentration of photons in the particular part of an image, as determined from the ratio of the signals of several largest pixels to the sum of all signals.
- **Alpha;** The angle between the major axis and a line jointed the centroid of the image to the source position.

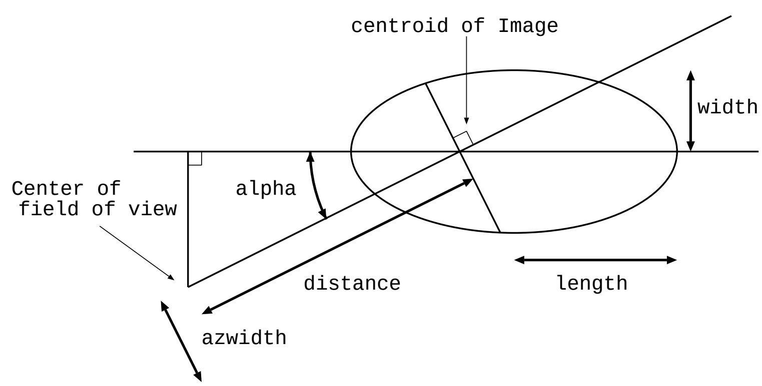

Figure 3.6: Definition of the parameters for the imaging technique.

The simulated distributions of the above parameters for both EASs initiated by gamma-rays and protons are shown in Figure 3.8. The Monte Carlo simulation were done assuming a point-like direction source for the gamma-rays and isotropic for the protons, respectively.

As mentioned above, the image of hadronic EAS should be broader in “Width”, longer in “Length” and lower in “Conc”, in general. due to the irregular and broad development. These image parameters are called “shape parameters”. On the other hand, to indicate the direction of the primary particle, “Distance” and “Alpha” are used, and called “orientation parameters”. The “Distance” reflects the distribution of the orientation angle of the primary particles. Since the cosmic-rays are isotropic, the number of events is proportional to its “Distance”. On the other hand, “Distance” of the gamma-ray EAS is concentrated to smaller than that of cosmic-ray EAS, because of the sharp development of EAS from the center of field of view. The “Alpha” of gamma-ray images coming from a point-like source should concentrate around 0 degree, while that of the hadronic images are distributed uniformly between 0 to 90 degree. The above features is seen in Figure 3.8.

The angular resolution of only ~ 1 degree was obtained by old ON-OFF chopping technique. However, the imaging technique provides the good angular resolution of ~ 0.2 degree for the directionality of gamma-ray images, as seen in the Alpha distribution of Figure 3.8.

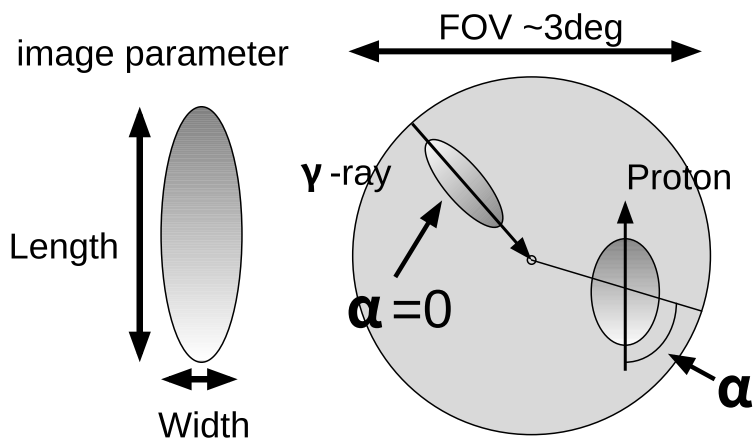

Figure 3.7: Illustration of EAS images on the focal plane. For gamma-ray EAS, the major axis of Čerenkov photon image indicates the source position, while for cosmic-ray EAS, it is distributed at random.

3.3.2 Definition of Calculation

The image parameters are calculated by following equations.

Assuming the elliptical image for Čerenkov photons, the major axis is defined as follows;

$$y = ax + b. \tag{3.10}$$

Figure 3.9 shows this schematically.

Defining the center of each pixel to be (x_i, y_i), pixel index " i ", and the amount of photons

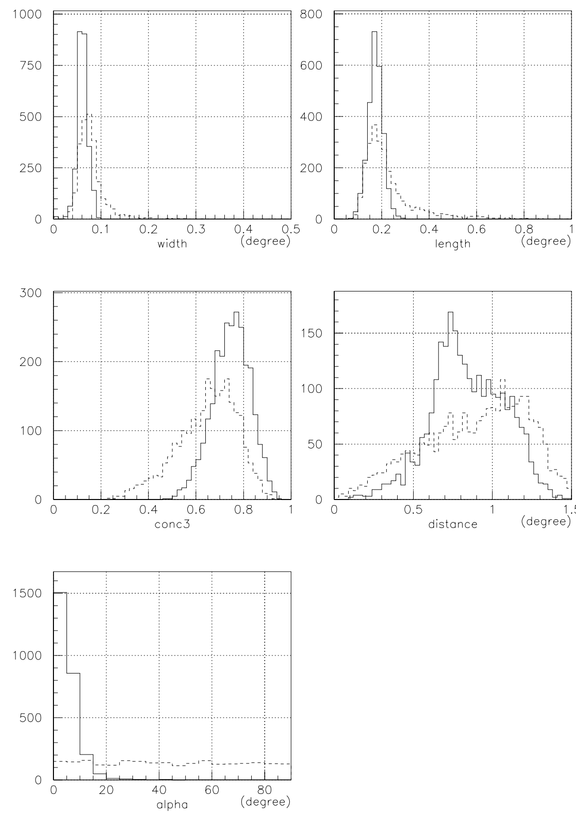

Figure 3.8: Distributions of image parameters (simulation). The solid line is for the gamma-ray (1 TeV) and broken line is for the cosmic-ray protons (3 TeV). For both, the number of generated events are almost equal.

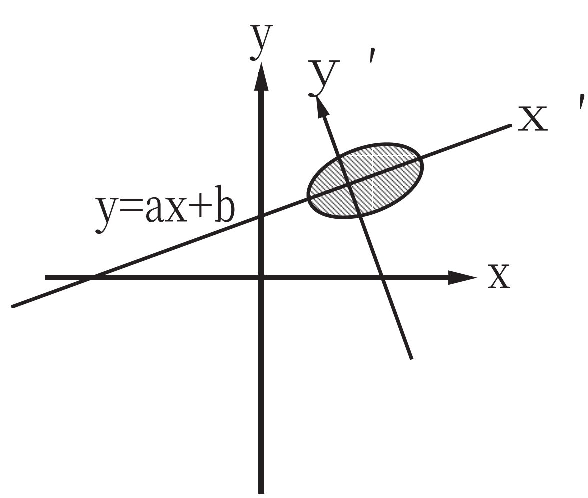

Figure 3.9: Coordinate setting for the image parameter calculation.

in the pixel to be s_i, various averages should be calculated as follows;

$$\langle x\rangle = \frac{\sum_i s_i x_i}{\sum_i s_i}, \quad (3.11)$$

$$\langle x^2\rangle = \frac{\sum_i s_i x_i^2}{\sum_i s_i}, \quad (3.12)$$

$$\langle x^3\rangle = \frac{\sum_i s_i x_i^3}{\sum_i s_i}, \quad (3.13)$$

$$\langle y\rangle = \frac{\sum_i s_i y_i}{\sum_i s_i}, \quad (3.14)$$

$$\langle y^2\rangle = \frac{\sum_i s_i y_i^2}{\sum_i s_i}, \quad (3.15)$$

$$\langle y^3\rangle = \frac{\sum_i s_i y_i^3}{\sum_i s_i}, \quad (3.16)$$

$$\langle xy\rangle = \frac{\sum_i s_i x_i y_i}{\sum_i s_i}, \quad (3.17)$$

$$\langle x^2 y\rangle = \frac{\sum_i s_i x_i^2 y_i}{\sum_i s_i}, \quad (3.18)$$

$$\langle xy^2\rangle = \frac{\sum_i s_i x_i y_i^2}{\sum_i s_i}. \quad (3.19)$$

Using the above, each R.M.S. (root mean square) deviation can be defined.

$$\sigma_{xx} = \langle x^2\rangle - \langle x\rangle^2, \quad (3.20)$$

$$\sigma_{xxx} = \langle x^3\rangle - 3\langle x^2\rangle\langle x\rangle + 2\langle x\rangle^3, \quad (3.21)$$

$$\sigma_{yy} = \langle y^2\rangle - \langle y\rangle^2, \quad (3.22)$$

$$\sigma_{yyy} = \langle y^3\rangle - 3\langle y^2\rangle\langle y\rangle + 2\langle y\rangle^3, \quad (3.23)$$

$$\sigma_{xy} = \langle xy\rangle - \langle x\rangle\langle y\rangle, \quad (3.24)$$

$$\sigma_{xxy} = \langle x^2 y\rangle - 2\langle xy\rangle\langle x\rangle - \langle x^2\rangle\langle y\rangle + 2\langle x\rangle^2\langle y\rangle, \quad (3.25)$$

$$\sigma_{xyy} = \langle xy^2\rangle - 2\langle xy\rangle\langle y\rangle - \langle y^2\rangle\langle x\rangle + 2\langle y\rangle^2\langle x\rangle. \quad (3.26)$$

The image axis parameters are defined as follows;

$$a = \frac{d + \sqrt{d^2 + 4(\sigma_{xy})^2}}{2\sigma_{xy}}, \quad (3.27)$$

$$b = \langle y\rangle - a\langle x\rangle, \quad (3.28)$$

$$(3.29)$$

where

$$d = \sigma_{yy} - \sigma_{xx}. \quad (3.30)$$

Finally, image parameters, "Width", "Length", "Distance" and "Alpha", are obtained;

$$\text{Width} = \sqrt{\frac{\sigma_{yy} - 2a\sigma_{xy} + a^2\sigma_{xx}}{1+a^2}}, \tag{3.31}$$

$$\text{Length} = \sqrt{\frac{\sigma_{xx} + 2a\sigma_{xy} + a^2\sigma_{yy}}{1+a^2}}, \tag{3.32}$$

$$\text{Distance} = \sqrt{\langle x \rangle^2 + \langle y \rangle^2}, \tag{3.33}$$

$$\sin(\text{Alpha}) = \frac{\mid b \mid}{\sqrt{1+a^2} \times \text{Distance}}. \tag{3.34}$$

Chapter 4

CANGAROO-II 10m Telescope

4.1 CANGAROO Project

The CANGAROO group [1] (Collaboration between Australia and Nippon for a GAmma-Ray Observatory in the Outback) is the international collaborated experiment between Australia and Japan for VHE gamma-ray observations since 1992.

Our group had observed southern VHE gamma-ray sources with the energy threshold of $\sim$ 2 TeV, using the 3.8m imaging air Čerenkov telescope operated near Woomera (Figure 4.1), South Australia (longitude 136°47'E, latitude 31°06'S, 160m a.s.l.) until 1998, and consequently, following TeV gamma-ray sources had been detected: the Crab pulsar/nebula, Vela pulsar, PSR B1706–44, SN1006 and RX J1713–37.

[1] The collaborators of CANGAROO group:
S.Hara, K.Sakurazawa, M.Moriya, J.Kushida, T.Takano; *Tokyo Institute of Technology*
T.Tanimori, H.Kubo, A.Asahara, J.Kataoka; *Kyoto University*
M.Mori, R.Enomoto, A.Kawachi, K.Okumura, S.Kabuki, H.Katagiri, F.Tsuchiya, H.Tsunoo,; *Institute for Cosmic Ray Research, University of Tokyo*
G.V. Bicknell; *Australian National University*
P.G. Edwards; *Institute of Space and Astronautical Science*
S.Gunji, T.Tokanai, T.Takano, A.Watanabe; *Yamagata University*
T.Hara, T.Naito; *Yamanashi Gakuin University*
S.Yanagita, T.Yoshida, C.Itoh; *Ibaraki University*
F.Kajino, S.Hayashi, S.Maeda; *Konan University*
T.Kifune; *Shinshu University*
Y.Muraki, Y.Matsubara; *Solar-Terrestrial Environment Laboratory, Nagoya University*
Y.Mizumoto; *National Astronomical Observatory of Japan*
H.Muraishi; *IPU*
K.Nishijima, T.Nakase, K.Uruma; *Tokai University*
J.R.Patterson, D.L.Swaby; *University of Adelaide*
T.Yoshikoshi; *Osaka City University*

Figure 4.1: Woomera in South Australia (longitude 136°47'E, latitude 31°06'S, 160m a.s.l.).

In order to investigate the sub-TeV energy region, a new 7m imaging air Čerenkov telescope has been constructed in March 1999, near the 3.8m telescope site, and operated since June 1999. Soon, we have extended the telescope aperture from 7m to 10m, by doubling the small mirrors on the reflector, in February 2000. Observations used in this thesis were carried out using the CANGAROO-II 10m telescope.

4.2 CANGAROO-II 10m Telescope

Figure 4.2 shows the photograph of the CANGAROO-II 10m telescope. This telescope has a 10.4m parabolic mirror consisting of 114 small plastic spherical mirrors. A composite mirror system is widely used by Čerenkov telescopes. Here, we have challenged the use of a plastic mirror and a parabolic frame. At the prime focus, we are equipped with a multi-pixel camera consisting of 512 PMTs covering the field of view of 2.8 degree. The details of each part are described hereafter. The characteristics of these telescopes are summarized in Table 4.1.

4.2.1 Main Frame and Driving System

The main frame of this telescope has a parabolic shape with the diameter of 10.4m and the focal length of 8m (i.e. F/0.77). This parabolic frame is one of the characteristics of the CANGAROO-II telescope. Most imaging air Čerenkov telescopes are designed as a Devis-Cotton type telescope. A Devis-Cotton type telescope has a structure that identical spherical mirrors are mounted on a spherical frame of which curvature radius is exactly a half of that of mirrors. About the off-axis focusing property, Devis-Cotton type is superior to a parabolic-frame type,

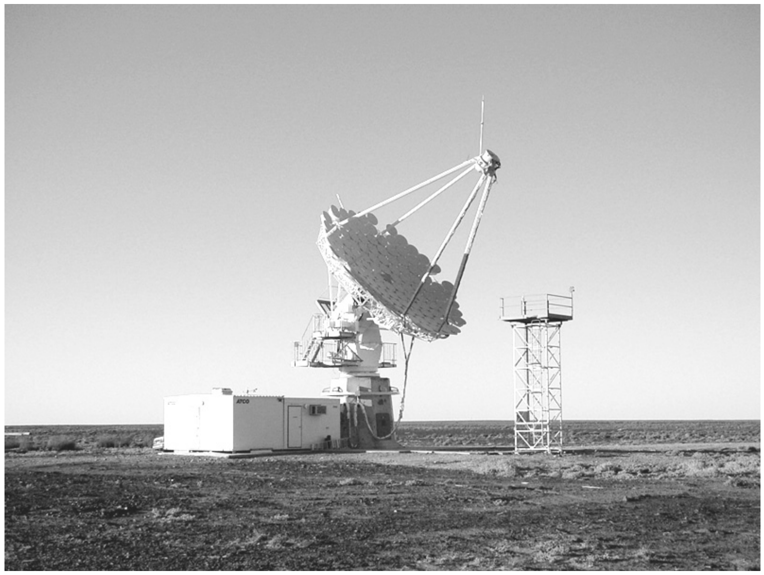

Figure 4.2: CANGAROO-II 10m telescope.

frame	parabolic
mount	altitude-azimuth mount
diameter	10.4m
focal length	8m
total correcting area	57.4m^2
the number of mirrors	114
shape of mirror	spherical
material	CFRP + aluminum sheet
diameter of mirror	80cm
focal length of mirror	16.4m
field of view	$2.8^\circ \times 2.8^\circ$
the number of PMTs	552
pixel size	16mm (0.115°)

Table 4.1: Specifications of CANGAROO-II telescope.

however it cannot get the information of the photon arrival time, because of the difference of the light path length depending on the position of the mirror. The parabolic frame type telescope is superior in acquiring the correct timing information. This timing information is very valuable for the elimination of night sky background noise as described in chapter 6.2.

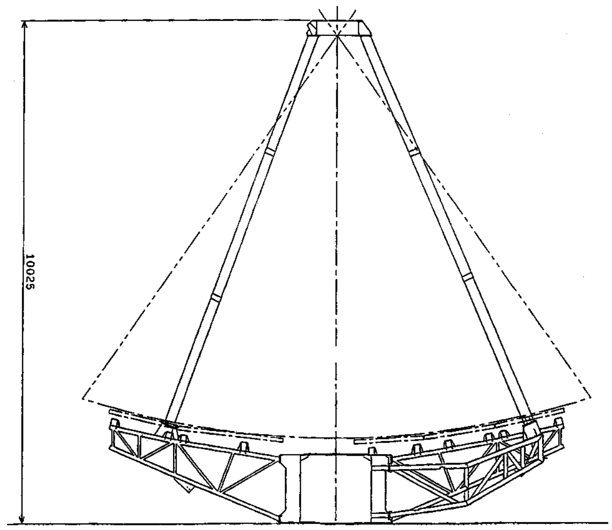

Figure 4.3: Main frame of the CANGAROO-II telescope (side view). The frame is designed to be parabolic.

The CANGAROO-II telescope is operated with an altitude-azimuth mount similar to other imaging air Čerenkov telescopes. The telescope controller is based on a 68K processor board. The computer calculates the coordinate of the present target position and sends the coordinate data to the telescope controller via a RS-232C serial port every 100 ms. In parallel, the computer receives the present direction of the telescope and controls as reducing the errors within 1 arc-min between two coordinates. In order to keep the real-time response for the telescope control, a KURT, which is the Linux operating system with a real-time extension, runs on the tracking control computer. The clock of the computer is synchronized to the coordinated universal time (UTC) by using the network time protocol (NTP) software with a GPS receiver (Furuno TS-800). In the above system, the accuracy of the tracking is better than 0.0001 degree.

4.2.2 Spherical Mirror

The reflector of CANGAROO-II 10m telescope consists of 114 small spherical mirrors and have a total collecting area of 57m^2. A small spherical mirror has a 80 cm diameter with the curvature radius of 16.4m. The curvature radius of produced mirrors are distributed between 15.9 and 17.1m, due to the accuracy limit of the pressing process in the production of the mirrors. However, these mirrors are arranged such that short radius mirrors are placed in the inner, and the long ones are in the outer, in order to minimize the aberration on the focal plane to be less than 0.1 degree in the field of view.

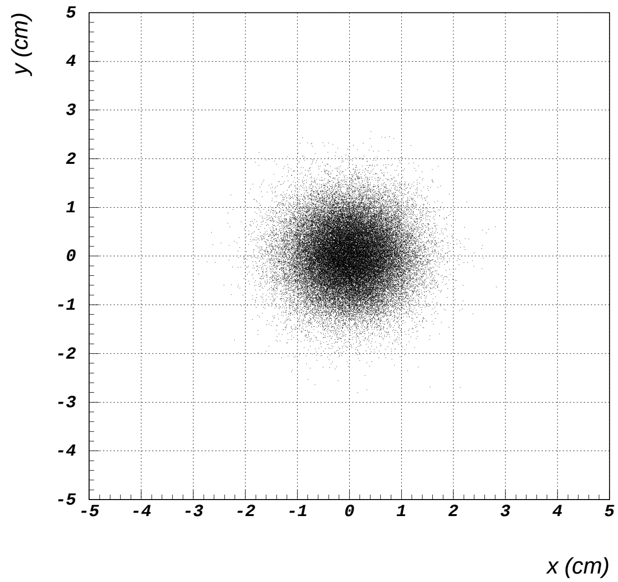

Figure 4.4: Aberration on the focal plane.

One of the most characteristic points of the CANGAROO-II telescope is that these mirrors are made of carbon fiber reinforced plastic (CFRP). The weight of a mirror is 6kg, 4 times lighter than that of glass. This light weight drastically reduces the load of the telescope and increases the durability. In addition, the surface of mirror is coated with fluorine to keep its reflectivity. Only with aluminum coating by vacuum evaporater, the reflectivity quickly decreases to a half. However, this mirror can be recovered its reflectivity up to 70% by water washing, even after three years operation. There is a strong requirement of this coating, since the surface of mirrors is damaged by dust and rain in particular for the CANGAROO-II telescope, which has no shed. The detail of the performance of the reflector is described in Kawachi *et al.*[24].

The direction of the each mirror direction is adjusted using two stepping motors (Oriental Motor PX533MH-A) installed in the back of each mirror (Figure 4.7). These two stepping motors are independently operated to adjust the two directions (x, y) of the mirror. The minimum step size of motors is 6×10^{-4} degree. A computer remotely controlled the stepping motors of each mirror via a relay switch.

After the first adjustment work (construction of 7m telescope), the deviation of mirror axis orientations achieved was 0.03 degree [23].

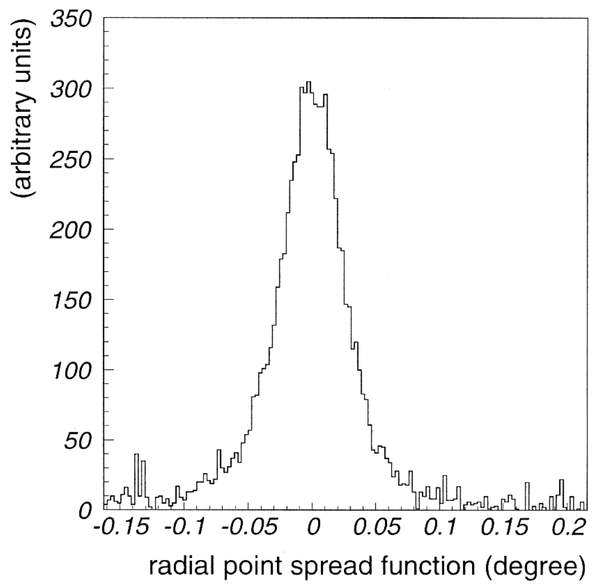

Figure 4.5: Radial point spread function of the mirror [24].

Figure 4.6: A spherical mirror of the CANGAROO-II telescope.

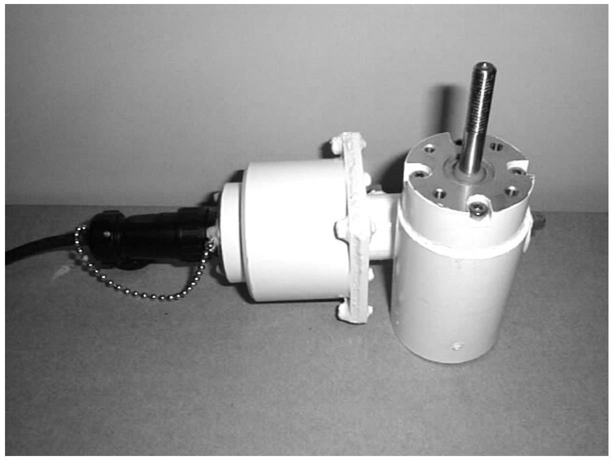

Figure 4.7: A stepping motor (Oriental Motor PX533MH-A) for adjustment of mirror direction.

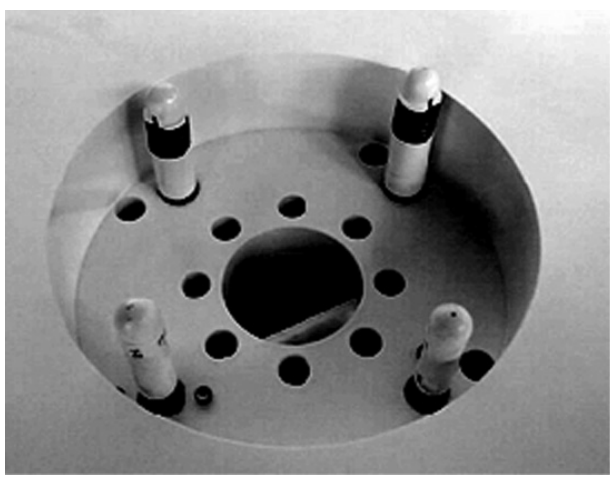

Figure 4.8: Structure for the mirror mount. Two of four supports are controlled by the stepping motors.

4.2.3 Imaging Camera

On the focal plane of the telescope, an imaging camera is installed, which consists of 552 photo-multiplier tubes (PMTs).

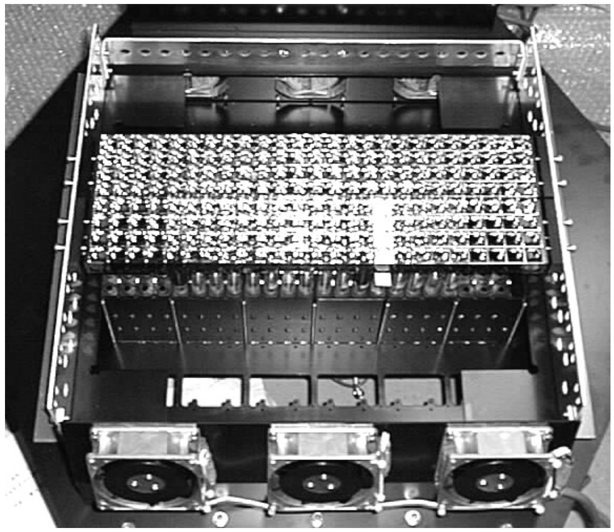

Figure 4.9: Imaging camera of the CANGAROO-II telescope. A part of the PMTs with light-guide are installed in this picture,

A PMT (Hamamatsu R4124UV) has a 13mm (1/2 inch) diameter with UV glass window, and its rise-time of signal is fast (1.1nsec). The photo-cathode is made of bialkali, of which spectral response is shown in Figure 4.11. Its average quantum efficiency is estimated to be 20% in the wavelength range from 250 to 500 nm.

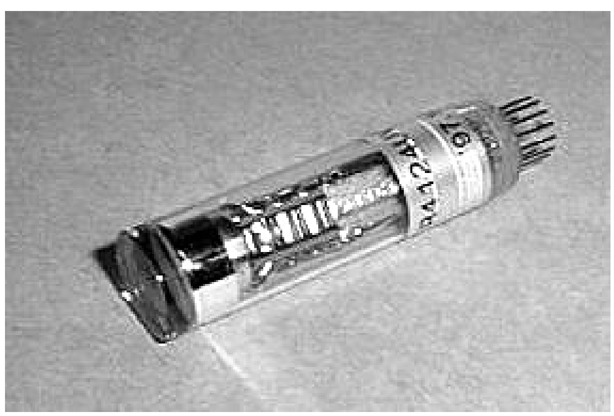

Figure 4.10: PMT Hamamatsu R4124UV, of which diameter is 13mm and length is 50mm.

A PMT covers $0.115° \times 0.115°$ square, which corresponds to 16mm $\times$ 16mm on the camera. A group of 4 PMTs (1×4 array) are installed in one amplifier module card (LeCroy TRA402S),

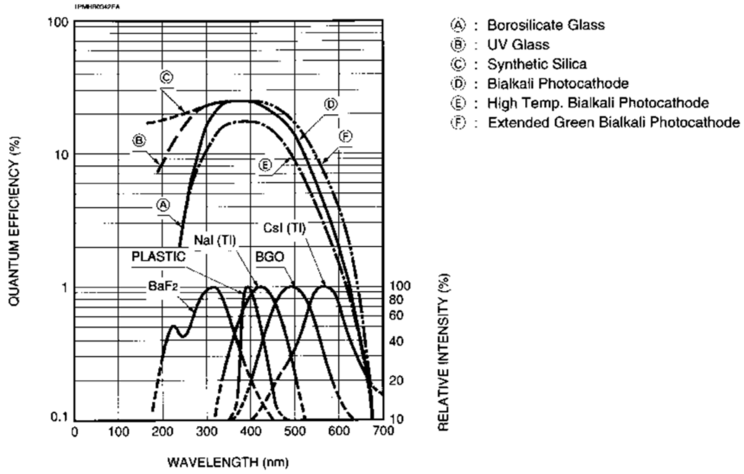

Figure 4.11: Spectral response curve of R4124. R4124UV is shown by the line marked B.

and 4 cards are installed in one high-voltage supply box (LeCroy 1461N). Each group of 16 PMTs are supplied with the same voltage of about -700V, and their gains are adjusted within 15%. This unit of 16 PMTs are arrayed in a 6×6 square with the four corner modules missing 10 PMTs of each edge. Total 552 pixels cover $2.8^\circ \times 2.8^\circ$ square as the field of view (Figure 4.12).

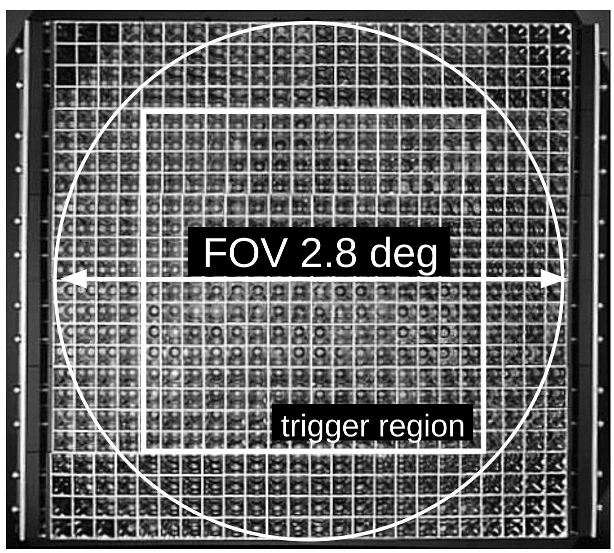

Figure 4.12: Field of view of the camera. The inner 256 PMTs are used for the event trigger.

Since the photo-cathode area of PMT is 10mm diameter, which covers only 30% of the pixel area, at the front of PMTs, the light-guide unit is attached in order to collect photons from the dead spaces over the photosensitive area of the PMTs. The light-guide (Figure 4.15) is

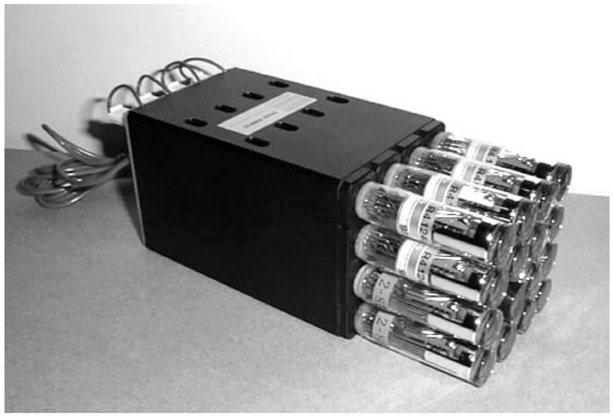

Figure 4.13: A AMP and high-voltage box of the imaging camera. This box contains with 4 amplifier cards, each of which amplifiers 4 PMTs.

made of acrylonitrile-butadiene-styrene (ABS) resin electroplated of aluminum, and its shape is a 16mm $\times$ 16mm square connected to a 10 mm diameter with a spline curve (Figure 4.15). The photons collected to a PMT becomes 1.1 times on average (Figure 4.16).

Figure 4.14: A light-guide for the CANGAROO-II imaging camera.

A blue LED is placed at the center of the reflector. This LED generates blue light pluses of about 20 nsec width, and is used to calibrate the relative gains of the PMTs.

4.2.4 Electronics and Data Acquisition System

The signals from all PMTs are fed to the electric hat by 36m twisted cables, which have the characteristic impedance of 74 Ω. The cables are connected to a VME divider module and a HV-power supply. The signal cables are also used as the power cables for the pre-amp, and one

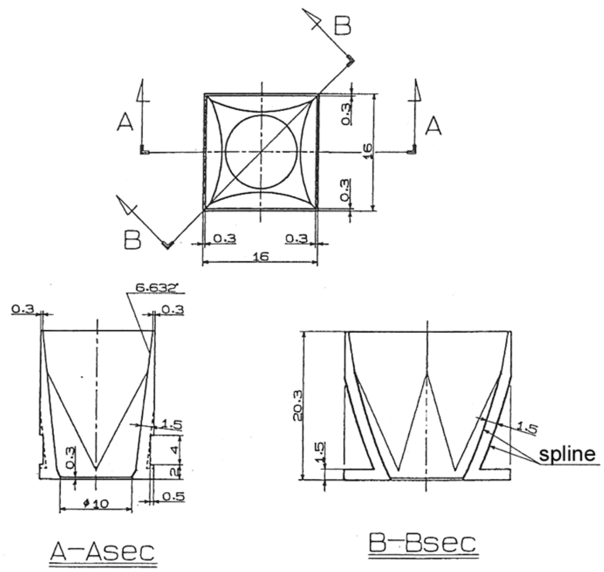

Figure 4.15: Structure of the light-guide for the CANGAROO-II imaging camera.

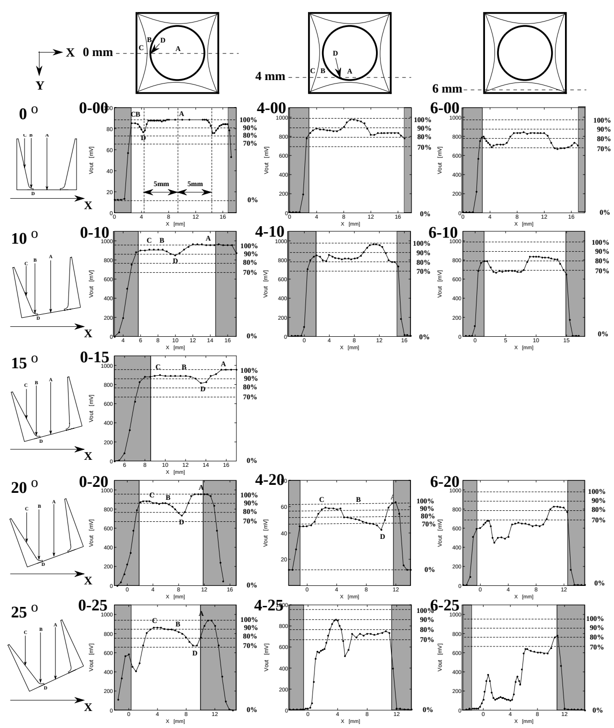

Figure 4.16: Measured efficiency of the light-guide. The photons collected to a PMT becomes 1.1 times on average.

signal line is grounded. The VME divider module divides the signal from PMTs to both the VME 9U-bus 32ch 12bit charge ADC(HOSHIN 2637) and TKO-bus Discriminator & Summing Module(DSM; HOSHIN 2548) which generates pulses used for the trigger decision. The signals of 2 AMP boxes (32ch of PMTs) are managed by one divider module, one DSM and one VME ADC. The ADCs receive the divided signals within the time window of 50 $\sim$ 100 nsec.

In the DSM, the signals are amplified and then divided into three signals. One is for the summing of 16 PMTs, which is available from the front panel. This signal is called the analog sum (Asum).

The second one is fed to the updated discriminator, and the discriminated pulses go to the CAMAC multi-hit TDC modules by flat cables. This discriminator makes a logic pulses of leading edge when a pulse exceeds the threshold level (called TDC-hit), of which width is proportional to the charge of signal as shown in Figure 4.17 and 4.18.

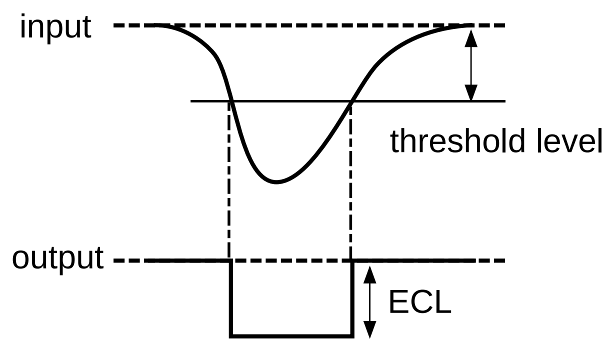

Figure 4.17: Updated discriminator. This discriminator makes a logic pulses of leading edge when a pulse exceeds the threshold level, of which width is proportional to the charge of signal.

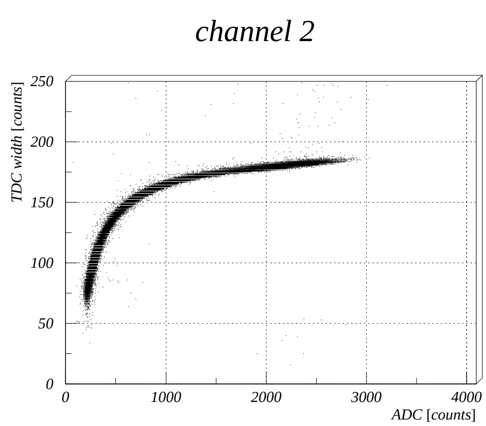

Figure 4.18: Correlation between the charge and the TDC width.

The third one is fed into a non-updated discriminator. The discriminated signals are fed into scaler on this board, which counts when signals exceed the threshold (called PMT-hit). This signal is also transformed into analog signal to be fed into summing-amplifier. This summed signal is called the logical sum (Lsum), and its pulse height is proportional to the number of hit PMTs. Lsum is available from the front panel.

Two threshold levels of the updated and the non-updated discriminators are controlled individually by the DAC in the same module. The level of TDC-hit threshold was set at $2 \sim 3$ photoelectrons in almost all observations.

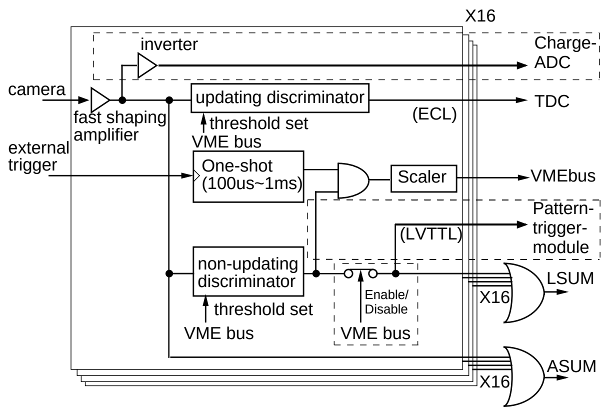

Figure 4.19: A schematic diagram of the front-end module(FEM) and discriminator & summing module(DSM).

After the DSM, the logical signals from updated discriminator are fed into the CAMAC multi-hit TDCs (LeCroy 3377). This TDC can measure up to 16 edges of sequential pulses with the resolution of 0.5 nsec during 256 nsec (9bit) in each channel. This good timing resolution becomes useful for the reduction of night sky background.

The signals of PMTs of the inner 16 AMP boxes are used to make the event trigger for the data acquisition(DAQ). Lsum signals from the DSMs of the inner 256 PMTs are summed, and discriminated at the preset value corresponding to several hit PMTs in the time window of 50 nsec. This threshold level is set to be $4 \sim 5$ PMTs. Asum signals of each AMP box are also discriminated, in order to require some concentration of photons in one AMP box. The final event trigger is generated by the coincidence between the above two discriminated signals. The global DAQ trigger is made of the event trigger, the GPS trigger and scaler trigger. The GPS trigger is made every 1 second for checking the time of DAQ system, and the scaler one is for reading the scaler counts in the DSM. The scaler counts within the time window of 700μsec for every event. Since this information is used for checking the night sky background and the electronic noises, its renewal frequency is not so fast, then the scaler trigger is made every 10 seconds.

The VME on-board CPU (FORCE 7V; Turbo Sparc 170MHz; Solaris 2.6) records the DSM scaler via VME-TKO interface, telescope tracking data via 100M-base fast-ether network from the telescope control computer, and the data of weather & cloud monitor via RC-232C interface. All the data from the VME-bus (ADC, GPS) and CAMAC data (TDC, visual scaler, interrupt register) are recorded by Linux PC workstation (Intel Pentium-II 266MHz; Redhat 6.2; Linux kernel 2.2) via VME-PCI and CAMAC-ISA interfaces, respectively. The portable DAQ system UNIDAQ[46] is installed and runs for DAQ and data storing to the hard-disk. The UNIDAQ was developed based on standard platforms so that the system could be easily ported to each institute. The system was developed by a collaboration between High Energy Physics Research Laboratory(KEK), Tokyo Institute of Technology, Superconducting Super Collider Laboratory(SSCL), Lawrence Berkeley Laboratory(LBL) and Michigan University. It is supported for almost all UNIX machines (SUN, DEC, SGI, HP, Linux and so on). The UNIDAQ system consists of mainly 4 modules, which are "Collector", "Recorder", "Analyzer" and "NOVA". The Collector reads the event data from various measuring instruments, and send the data to the NOVA. The NOVA is the buffer manager of the data flow from the Collector. The Recorder receives the data from the NOVA, and records it to the storage device; the hard disk drive is required for the CANGAROO-II telescope. The Analyzer displays the data in the real-time; this part is described later.

In order to keep the data as small as possible, the flexible data size of one event is adopted (TDCs record the data for only hit PMT). The typical data size of one event is 1.5 kbytes, and the data rate is $\sim$ 45kbyte/sec in average. The DAQ system can accept up to 80Hz triggers with a dead time of 20%. In the usual observation, it is operated at less than 30Hz. [30].

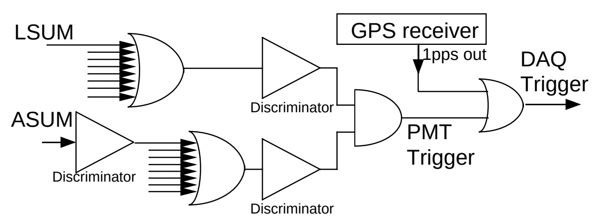

Figure 4.20: A diagram of event trigger logic.

In order to check the quality of the data in real-time, another Linux PC workstation (Intel Pentium-III 600MHz; LASER5; Linux kernel 2.2) simultaneously receives the data via 100base fast-ether network, and displays the ADC charge, the TDC start timing, the DSM scaler, and so on, using the Analyzer of the UNIDAQ. This computer also serves the system clock via NTP for all network computers by receiving GPS clock individually.

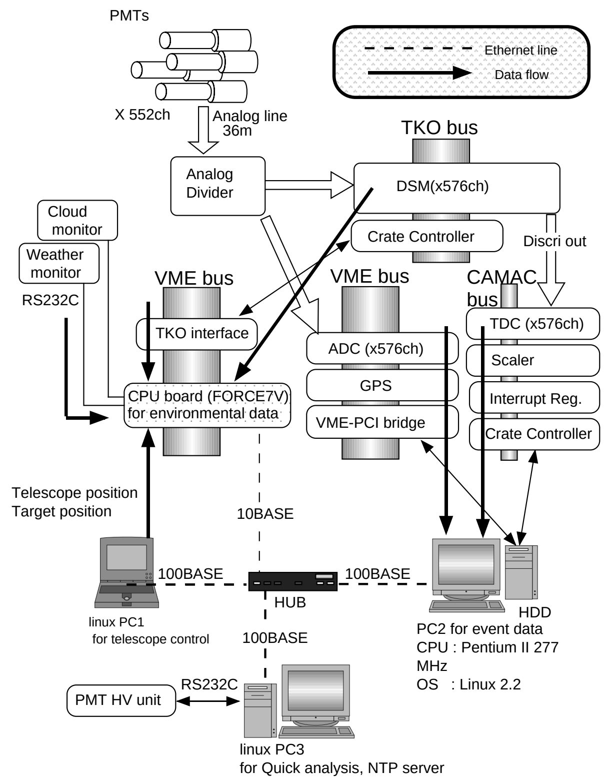

Figure 4.21: A diagram of DAQ for the CANGAROO-II 10m telescope.

Chapter 5

Observation and Calibrations

5.1 Observation of the SN1006 NE-rim

The observation of Supernova remnant SN1006 was done using the CANGAROO-II 10m telescope in April and May 2000.

In this observation, the North-Eastern rim of SN1006 was pointed as a gamma-ray source from the results of the CANGAROO 3.8m telescope [68]. In order to estimate the background cosmic-ray events contained in the observation for the gamma-ray source, ON-source and OFF-source runs were operated as follows in every observation; the telescope tracked the target position (called ON-source run), or the same path shifted with the Right Ascension offset corresponding to the ON-source observation time (called OFF-source run).

Before or after every run, the calibration runs were done to measure the variation of the gain of each PMT using the blue LED set on the center of the reflector, which emits successive pulses of 20 nsec width each.

In the ON-source run, the tracking position was usually set at the center of the camera, to obtain the maximum field of view for the gamma-ray detection. However in this observation of SN1006, the field of view of ON-source contains two 3.4 and 2.8 magnitude bright stars located by 0.9 and 1.7 degree from the NE-rim, respectively. Since these bright stars would increase the trigger rate drastically and distort the Čerenkov photon image, the tracking position of the ON-source run was shifted by $(\mathrm{R.A.}, \mathrm{Dec}) = (0.20^\circ, 0.25^\circ)$ or $(0.51^\circ, 0.16^\circ)$, from the source position (NE-rim), respectively.

The total observation time was 55.2 (48.8) hours, for ON-source (OFF-source) run. In order to keep the effects of weather conditions as small as possible, only the data observed in the good sky condition were used. This selection was done by checking the variation of the air shower rate during the observation. The estimation of this rate is described in the following chapter. The resulted good quality data of 52.2 and 44.9 hours were used for ON-source and OFF-source runs, respectively.

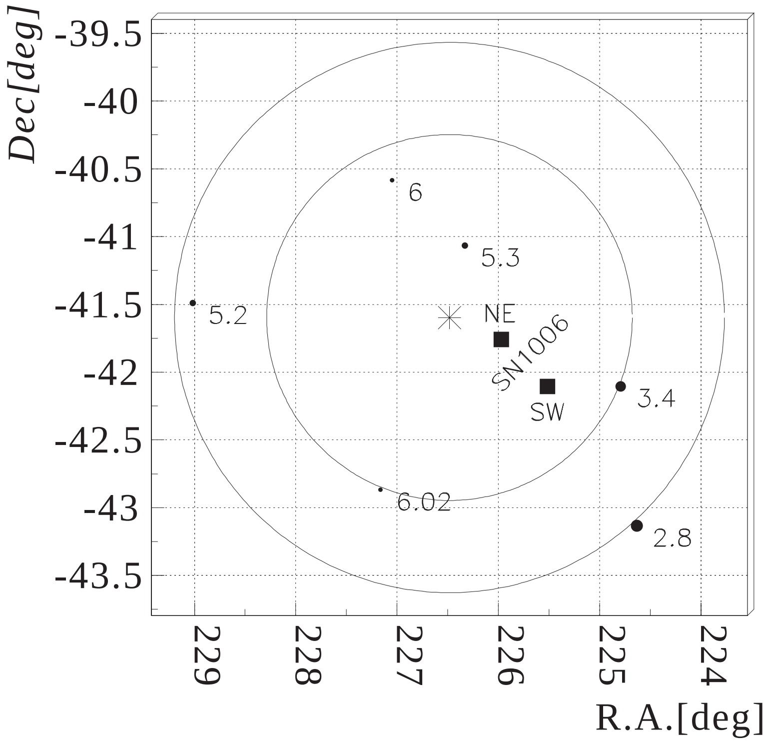

Figure 5.1: Star field map around SN1006. The center of these circles is shifted tracking position $(\mathrm{R.A.}, \mathrm{Dec}) = (+0.51^\circ, +0.16^\circ)$. The inner circle means the boundary of the trigger region, and the outer is that of the field of view.

Period	Tracking position	Offset from the NE-rim
April 1 – 2	$(226.1759^\circ, -41.4998^\circ)$	$(0.20^\circ, 0.25^\circ)$ $\Delta 0.30^\circ$
April 5 – 11	$(226.4833^\circ, -41.5974^\circ)$	$(0.51^\circ, 0.16^\circ)$ $\Delta 0.42^\circ$
April 27 – May 11	$(226.4833^\circ, -41.5974^\circ)$	$(0.51^\circ, 0.16^\circ)$ $\Delta 0.42^\circ$

Table 5.1: Tracking position (RA,Dec) shifted for the bright stars.

Period	ON (selected)	OFF (selected)
April 1 – 11	13.6 (11.2)	14.0 (11.3)
April 27 – May 11	41.6 (41.0)	33.9 (33.6)
Total	55.2 (52.2)	48.8 (44.9)

Table 5.2: Observation time (hours) for this analysis. The data used for analysis is selected by the sky condition.

5.2 Calibration

5.2.1 Tracking Center

As mentioned in chapter 3, the orientation of a gamma-ray EAS images is sensitive to the position of the source in the field of view. Therefore, it is important to calibrate the tracking position in the field of view. The fine pixel of the CANGAROO-II imaging camera allows the accurate determination of the tracking point.

The count rate of a PMT increases enormously when a bright star passes through the PMT. A candidate of the VHE gamma-ray source generally is not bright at the optical wavelength, and cannot be directly found its position by using PMT count rate. However, there often exist some bright stars in the field of view. The telescope is mounted on an altitude-azimuth mount and the imaging camera is fixed to the telescope. An object in the field of view rotates when the telescope tracks the target point of the sky. Thus, the image of the star rotates in the field of view, and the center of rotation should be consistent with the center of field of view.

The position of the tracking point on the camera is estimated in the following procedure. First, in order to extract the starlight signals from scaler counts, the background level of the scaler counts in the dark night sky were measured for each PMT. The count of the PMT, which was located at the bright star position, was not used for this estimation. Since the image of the bright star was extended over the pixel size, the region around it, defined as a radius of 2 pixel, was removed in this analysis (this region is called "star region" in the following analysis).

Second, the root mean square (RMS) of the scaler count is estimated for each PMT, then the 2-dimensional map of RMS value was made for the star region. This map has a peak, reflecting on the distribution of the bright star. This peak corresponds to the real position of the star, and comparing the distance and the direction of the difference between the real position and the calculated one, we can estimate the position of the tracking point, which is weighted time(events) of each run. The RMS map of all run was superimposed, and the peak was fitted to a 2-dimensional Gaussian distribution. The position of resulted maximum peak should be the most probable position for the tracking point.

There exists two bright stars in the field of view of SN1006. One of these, 2.8 magnitude star, was the brought out of field of view, since it was too bright. The other 3.4 magnitude star in the field of the view was used for this analysis. This star was distant at 1.3 degree from the tracking point, and good enough to estimate the tracking point accurately [83] [40]. As a result, the estimated tracking position is $(-0.06° \pm 0.08°, -0.07° \pm 0.08°)$ in the camera coordinate.

At the construction of the telescope, the measurement of the optical axis of the telescope was carried out, using the CCD camera which is set on the center of the reflector. The result was $(-0.058° \pm 0.01°, -0.015° \pm 0.01°)$. The point estimated from the scaler count is consistent with that obtained using the CCD within the error of this analysis. In the following analysis,

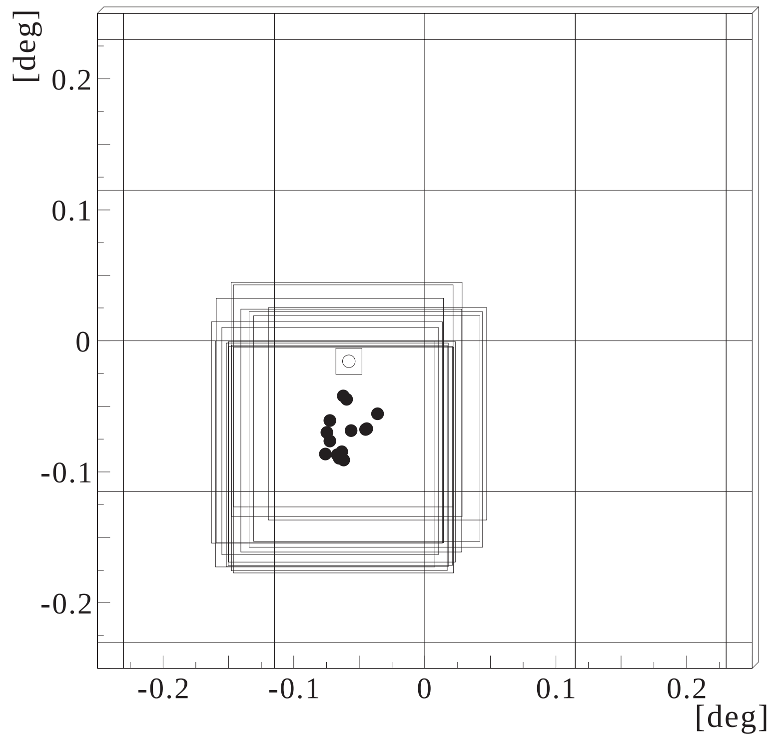

Figure 5.2: Estimated tracking center. The filled circles with boxes are the tracking center positions and error boxes estimated for every ON-source run. The blank circle with box is the position measured by CCD. The grids imply the camera pixels.

we use this CCD point as a tracking position.

5.2.2 ADC Calibration

At the first step in the analysis, each ADC value is subtracted by its pedestal value. The pedestal value was measured using the data of the calibration run, which was obtained by random trigger in the night sky. The measured pedestals of ADCs usually include the effect of night sky background light. The difference of the means of measured pedestals were less than 7% between the random-triggered run including night sky background and the random-triggered run with covered camera (without any photon). Then the pedestal values including night sky background were used in the following analysis.

The relative gain of each PMT was calibrated using the blue LED. Two data sets of different luminosity of the LED, namely 0dB and 1dB LED-run data, were used for this calibration. At first, the mean value for each PMT (a suffix i implies the i-th PMT) $Q_i(x\text{dB})$ and the averaged value for all PMTs $Q_{\text{ave}}(x\text{dB})$ were obtained for 0dB and 1dB, respectively. In order to reduce the night sky background, arrival timing of hit PMT was used. As the width of the LED pulse is 20 nsec, the calibration used the signal of which timing was within 75 nsec. The relative gain value for the i-th pixel G_i were obtained by fitting the following linear function;

$$G_i \equiv \frac{Q_{\rm ave}(x{\rm dB})}{Q_i(x{\rm dB})} \tag{5.1}$$

using two points, 0dB and 1dB. The obtained relative gain for each ADC is normalized to 1 by the mean of the relative gains of all PMTs.

5.2.3 Time-walk Correction

The CANGAROO-II telescope provides the accurate timing information of arrival photons, thanks to the parabolic mirror. In order to utilize this information, it is needed to correct the time-walk effect; when hit pulses are discriminated at some value of threshold, the timing of the discriminated pulse has an offset depending on its pulse height. The correction for the time-walk was estimated using the LED calibration data. The width of TDC pulse from the updated discriminator on DSM is used instead of its pulse height.

At first, the correlation between TDC width and TDC start count (the mean of the arrival timing) was plotted for each pixel, and fitted by the following quadratic function:

$$\mathrm{TDCstart} = f(\mathrm{TDCwidth}), \tag{5.2}$$

$$f(x) = P_0 + P_1 x + P_2 x^2. \tag{5.3}$$

Figure 5.3 shows a typical profile of TDC width v.s. TDC start count, fitted by the quadratic function. The corrected TDC start information is expressed as follows;

$$\mathrm{TDCstart_{correct}} = \begin{cases} f(175) - \mathrm{TDCstart} & (\mathrm{TDCwidth} > 175\mathrm{counts}) \\ f(\mathrm{TDCwidth}) - \mathrm{TDCstart} & (\mathrm{TDCwidth} < 175\mathrm{counts}) \end{cases} . \tag{5.4}$$

After this calibration, the full width at half maximum (FWHM) was improved to ~ 31 nsec from ~ 35 nsec of the raw data.

We use a self-trigger system in the data acquisition system of the CANGAROO-II telescope; the stop timing of TDCs are generated from PMT signals themselves. Therefore timing of the trigger varies event by event, according to the pulse shape of Čerenkov photons which usually fluctuate. In order to correct this fluctuation the average timing of hit PMTs is adjusted to the same value event by event. Figure 5.4 shows the arrival timing accumulated of all PMTs for all events. The FWHM of uncorrected timing distribution is ~ 31 nsec. After above calibration of timing information, the resultant distribution of the arrival timing is improved to ~ 18 nsec, and this distribution is consistent with the expected value from the distribution of the Čerenkov photons from the hadronic EAS simulation.

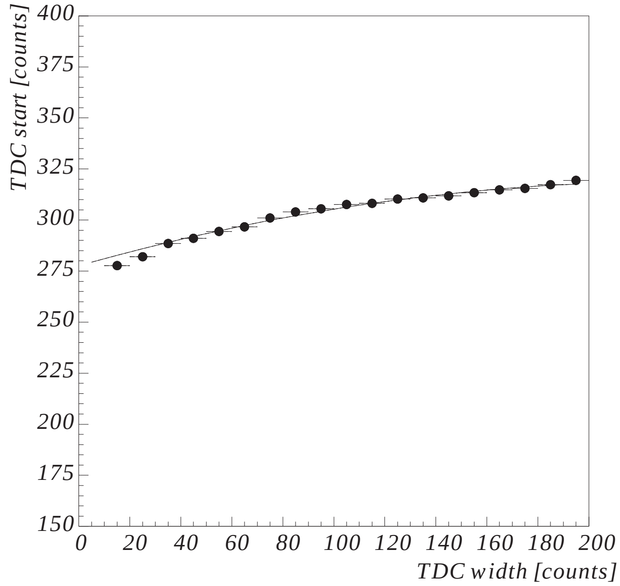

Figure 5.3: Profile of TDC width v.s. TDC start count using LED calibration data, fitted by a quadratic curve.

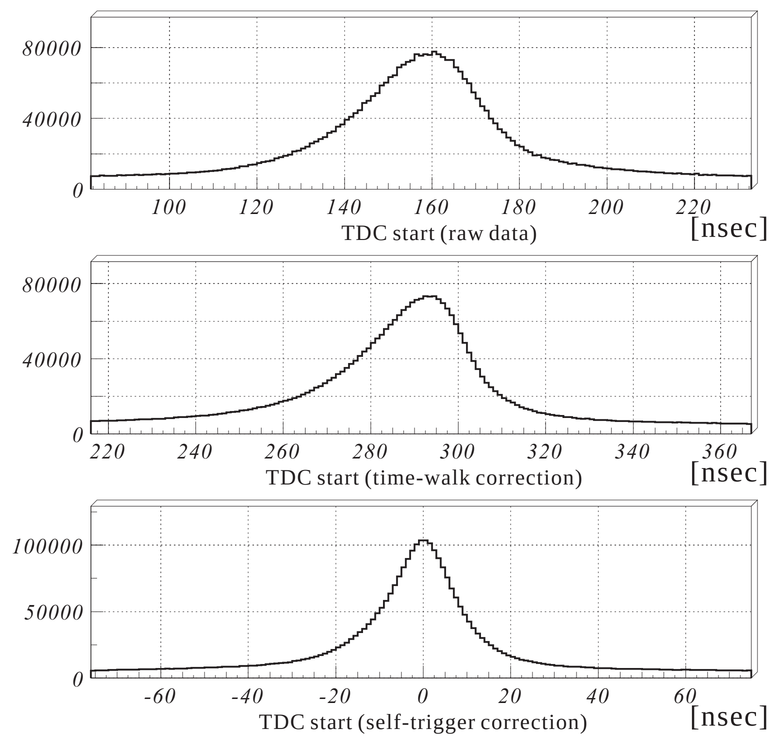

Figure 5.4: Timing distributions of all hit pixels of all events. The upper histogram is uncorrected timing (FWHM 35 nsec), the middle is corrected for the time-talk (FWHM 31 nsec), and the lower is corrected for self trigger timing (FWHM 18 nsec).

5.2.4 Trigger Condition

As mentioned in chapter 4.2.4, the master trigger is generated from Lsum signals. As almost all single counts of PMTs are due to the night sky background, we can estimate the threshold levels for two discriminators using the count rates recorded by the TDCs and DSM scalars.

The brightness of the night sky background (NSB) used is the value summarized by Jelly [19] as the standard night sky.

$$\frac{\mathrm{d}^3W}{\mathrm{d}S\mathrm{d}t\mathrm{d}\Omega} = 2.55 \times 10^{-4}\ [\mathrm{erg}\cdot\mathrm{cm}^{-2}\cdot\mathrm{sec}^{-1}\cdot\mathrm{str}^{-1}] \quad (430 \sim 550\mathrm{nm}). \tag{5.5}$$

This is commonly used as the standard intensity of NSB. Assuming the uniform spectrum of NSB, the photon energy per unit wavelength is estimated to be

$$\frac{\mathrm{d}^4W}{\mathrm{d}S\mathrm{d}t\mathrm{d}\Omega\mathrm{d}\lambda} = 2.125 \times 10^{-6}\ [\mathrm{erg}\cdot\mathrm{cm}^{-2}\cdot\mathrm{sec}^{-1}\cdot\mathrm{str}^{-1}\cdot\mathrm{nm}^{-1}]. \tag{5.6}$$

The number of photons in wavelength between λ_1 and λ_2 can be calculated,

$$\begin{aligned}\frac{\mathrm{d}^3N}{\mathrm{d}S\mathrm{d}t\mathrm{d}\Omega} &= \int_{\lambda_1}^{\lambda_2} \frac{\mathrm{d}^4W}{\mathrm{d}S\mathrm{d}t\mathrm{d}\Omega\mathrm{d}\lambda}\left(\frac{hc}{\lambda}\right)^{-1}\mathrm{d}\lambda \\ &= \frac{\lambda_2^2-\lambda_1^2}{2hc}\cdot\frac{\mathrm{d}^4W}{\mathrm{d}S\mathrm{d}t\mathrm{d}\Omega\mathrm{d}\lambda},\end{aligned} \tag{5.7}$$

where, h and c are plank constant and light velocity, respectively. Substituting the parameters of Table 5.3 to the above equation, the number of NSB photons is estimated as follows,

$$\frac{dN}{dt} = \frac{\mathrm{d}^3N}{\mathrm{d}S\mathrm{d}t\mathrm{d}\Omega} \times S_{\mathrm{mirror}} \times \Omega_\theta \times \varepsilon_q \times \varepsilon_{\mathrm{mirror}} \times \varepsilon_{\mathrm{guide}} \tag{5.8}$$

$$= 9.66 \times 10^{-3}\ [\mathrm{photoelectrons}\cdot\mathrm{nsec}^{-1}\cdot\mathrm{PMT}^{-1}]. \tag{5.9}$$

This value may have a fluctuation of about factor 2, depending on some uncertainties (place,

range of wavelengths; $\lambda_1 \sim \lambda_2$	$350 \sim 650$nm
collecting area of reflector; S_{mirror}	5.74×10^5cm^2
field of view of 1 pixel; Ω_θ	0.11×10^{-3}str
	$(0.115° \times 0.115°)$
quantum efficiency of PMT; ε_q	0.2
reflectivity of spherical mirror; $\varepsilon_{\mathrm{mirror}}$	0.7
efficiency of light-guide; $\varepsilon_{\mathrm{guide}}$	0.26

Table 5.3: Parameters for the estimation of night sky background photons.

time, weather, ... etc.). This fluctuation can explain the observed fluctuation of the count rate of PMTs by the Poisson fluctuation. The probability of accidental trigger rate P is defined as follows,

$$P \sim \sum_{N=m}^{\infty} \frac{N^n}{n!} \mathrm{e}^{-N} = 1 - \sum_{n=0}^{m-1} \frac{N^n}{n!} \mathrm{e}^{-N}, \tag{5.10}$$

where, m is the number of photoelectrons which corresponds to the threshold level of the discriminator. The expected count rate is shown as a function of a threshold level in Figure 5.5 with the fluctuation of factor 2.

The count rates of the Lsum discriminators are counted by the scalers in DSM, and those of the TDC discriminators are counted as a number of the multi-hit signals obtained by TDCs. These distributions of count rates, measured in April 2000 by random trigger run, are shown in Figure 5.6 and Figure 5.7. The count rates of these discriminators for one PMT are estimated, respectively,

$$\text{count rate}_{\text{TDC}} = 286 \text{ [hits/msec]}, \tag{5.11}$$

$$\text{count rate}_{\text{Lsum}} = 11.6 \text{ [hits/msec]}. \tag{5.12}$$

Consequently, the threshold levels of two discriminators are estimated from Figure 5.5,

$$\text{Threshold level}_{\text{TDC}} = 2.0 \pm 0.5 \text{ [p.e.]}, \tag{5.13}$$

$$\text{Threshold level}_{\text{Lsum}} = 3.0 \pm 0.5 \text{ [p.e.]}. \tag{5.14}$$

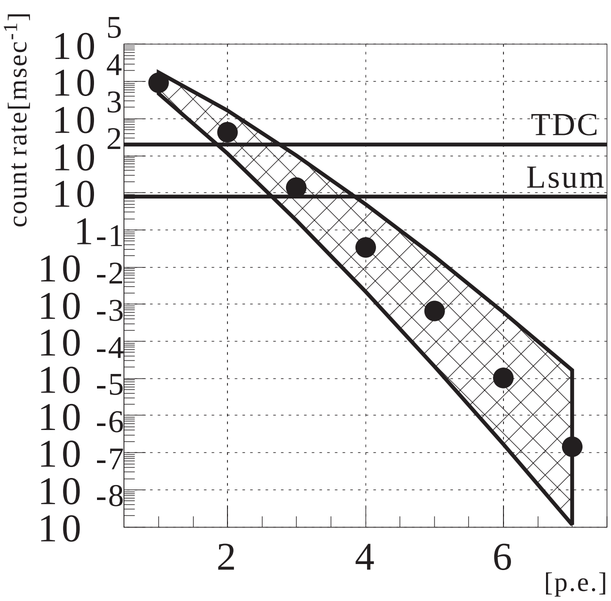

Figure 5.5: Relation between accidental trigger and threshold levels of Lsum and TDC discriminators. The hatched area means the fluctuation of NSB photons. The count rate is expressed in msec^{-1}.

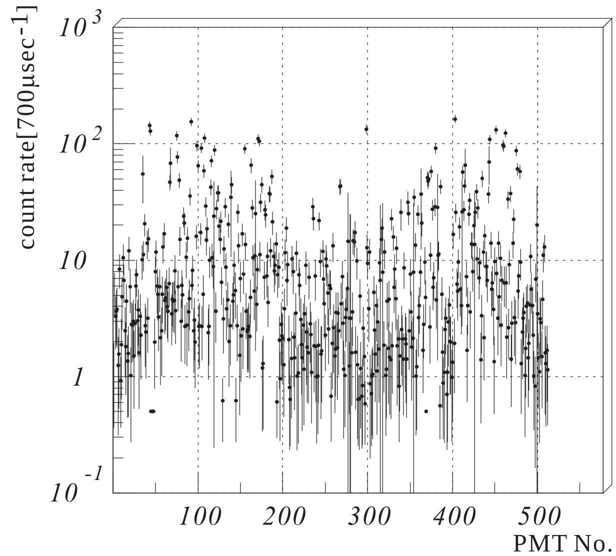

Figure 5.6: Distribution of the scaler value of the Lsum discriminator. The data of the count rate exceeding 100 (per 700 μsec) are removed from estimation of threshold level, in order to avoid bright star light. From this distribution, the count rate of the Lsum discriminator was estimated to be 11.6 hits/msec.

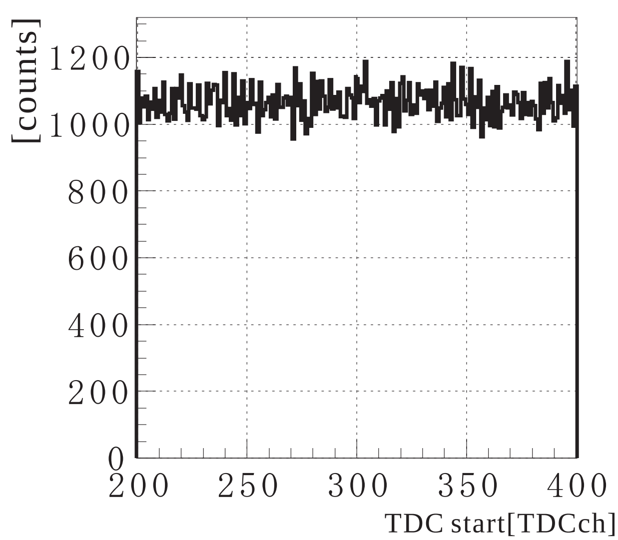

Figure 5.7: Distribution of TDC start signal. 1 TDCch is 0.5 nsec. From this distribution, the count rate of TDC was estimated to be 286 hits/msec.

Chapter 6

Analysis

6.1 Estimation of 1 p.e.

In order to compare the simulated and observed spectra, the absolute energy estimation of the sum of ADC is needed. Also the conversion factor from a ADC value to the absolute energy is significant to obtain the absolute energy of detected gamma-rays. Here we developed a comprehensive method to evaluate this parameter by comparing these spectra.

6.1.1 Simulation

A Monte Carlo simulation used in the CANGAROO-II analysis has been developed using the GEANT utility. The simulation code mainly consists of four components: the generators (energy, direction ...etc.) of primary particles, the EAS from a primary particle, the Čerenkov photons from the EAS, and the triggered event information by electronics, respectively.

As a generator of the EAS, GEANT version 3.21 is used. GEANT is a utility system of the detector description and simulation tools for high energy particle physics, which has been developed in CERN, and distributed in the world as one of the CERN library [86]. The atmosphere is described as 160 layers of particle calorimeter, which used air of 50 km altitude divided into 160 layers, because GEANT treats material of only uniform density. The US standard atmospheric structure is used to calculate the air density. The magnetic filed in the atmosphere is calculated at the telescope site assuming the dipole magnetic field of the earth.

In the EAS generated by GEANT, Čerenkov photons are produced from each charged particle. The number of photoelectrons in PMTs are calculated using equation (3.6). Here the Rayleigh and Mie scatterings, wavelength dependence of mirror reflectivity, and the quantum efficiency of the PMTs are also taken into account. Generated Čerenkov photons are collected by the reflectors on the ground. In addition, the structure of small mirrors including deformation, and the trigger condition mentioned in chapter 5.2.4 are also taken into account.

The obtained Čerenkov photons on the focal plane are converted to the ADC and TDC counts in the simulation code. The images of EAS are constructed for each triggered event taking the night sky background into account. The simulated images are fed to the same program used in the analysis of real data.

6.1.2 Cosmic-ray Events

In order to examine the performance of our simulation of cosmic-rays (proton), some imaging parameters calculated in the simulation (protons of 500 GeV $\sim$ 10 TeV) are composed with those obtained from the OFF-source data, and their comparisons are presented in Figure 6.1. Although there seems to be a small difference between the distributions, those looks to be reproduced well by the simulation.

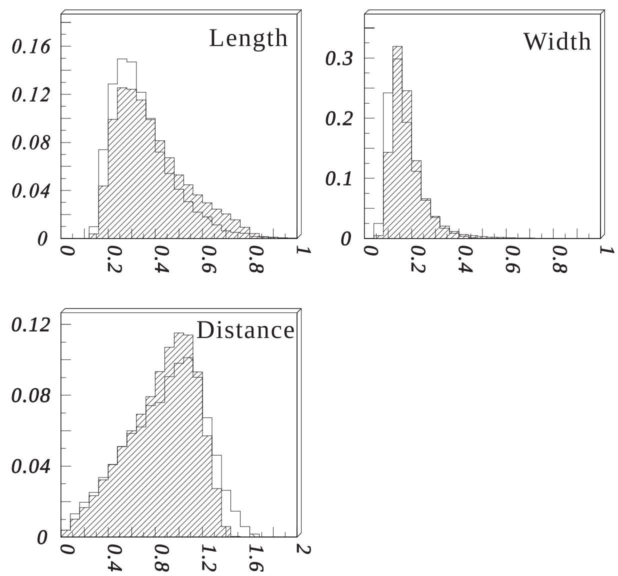

Figure 6.1: Imaging parameters ("Length", "Width" and "Distance") of the OFF-source (hatched histogram) and simulation data (blank histogram). The proton simulation was carried out in the energy range between 500 GeV and 10 TeV.

Here, we compare the cosmic-ray spectra obtained from the OFF-source data and from the proton simulation data. Figure 6.2 shows the event distributions as a function of the sum of the number of photoelectrons (simulation) and the sum of ADC value (OFF-source data), both of which correspond to the energy of the EAS. Both the slopes of the spectra become flatter as a energy decreases, due to the decrease of the detection efficiency around the threshold energy.

In addition, the count rate of EAS events can be estimated using the simulation study. At first, the threshold energy of the CANGAROO-II 10m telescope for cosmic-rays was estimated. Figure 6.3 shows the simulated correlation between the number of photoelectrons from the

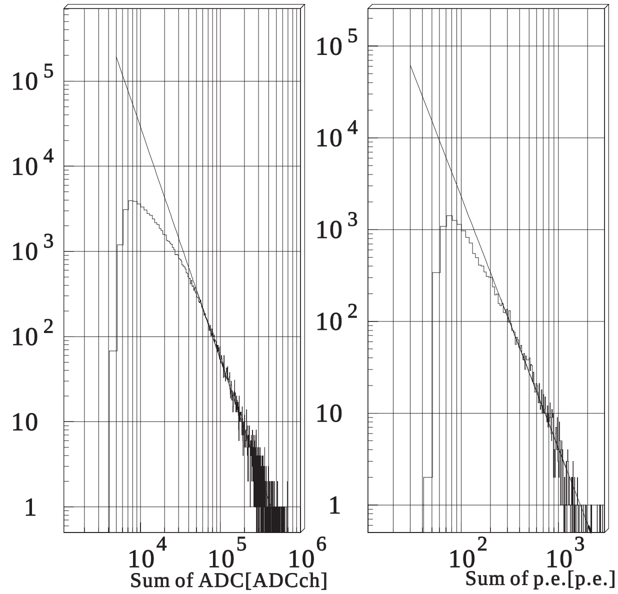

Figure 6.2: Spectra of the OFF-source (left) and simulation (right) data. The simulation was carried out for the energy range of 500 GeV to 10 TeV. The both spectra were fitted to a power-law function with a index of -2.7.

hadronic EAS and its primary energy. Although the sum of the number of Čerenkov photons is expected to be proportional to the energy of the EAS, the correlation curve becomes flatter as a energy decreases, which are considered to be due to the increase of the inefficiency. From this study, the threshold energy for cosmic-rays was estimated to be ~ 600 GeV.

Using this threshold energy, the rate of EAS events detected by the CANGAROO-II 10m telescope was calculated. As a standard cosmic-ray flux, we used the following value summarized by Ichimura *et al.* [17].

$$F(E) = 2.34 \times 10^4 (E/\mathrm{GeV})^{-2.78} \quad [\mathrm{m}^{-2} \cdot \mathrm{sec}^{-1} \cdot \mathrm{str}^{-1} \cdot \mathrm{GeV}^{-1}] \tag{6.1}$$

The event rate of cosmic-rays R was calculated as follows:

$$R = \int_{E_{\mathrm{th}}}^{\infty} F(E) S_{\mathrm{eff}}(E) \Delta\Omega dE \tag{6.2}$$

$$\sim 2.2[\mathrm{Hz}] \ , \tag{6.3}$$

where $\Delta\Omega$ is the angle of field of view (9.5×10^{-4} str), and $S_{\mathrm{eff}}(E)$ is the effective area as a function of the proton energy. Figure 6.4 shows the event rate of OFF-source run, and the event rate of ~ 2.7Hz was obtained from this rate curve, which was already applied the noise rejection described in chapter 6.2, while the ADC pedestal cut was done loosely (300 ADCch). The count rate of the EAS events detected (~ 2.7Hz) was well consistent with the simulated one,

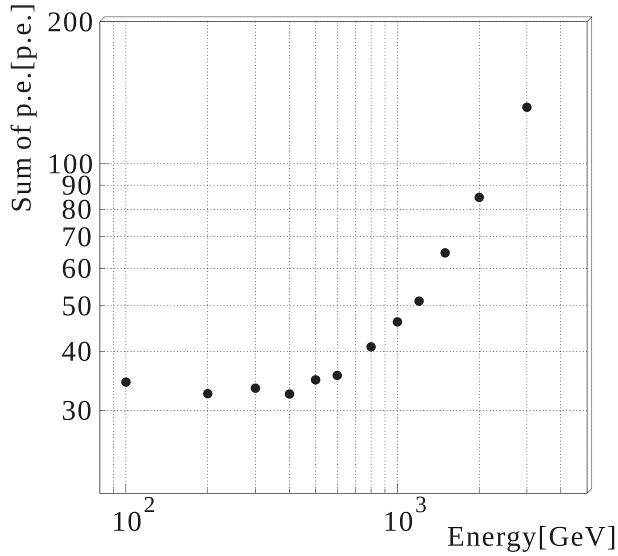

Figure 6.3: Correlation between the number of photoelectrons from the hadronic EAS and the primary energy of the cosmic-ray proton.

assuming the threshold energy to be $\sim$ 600 GeV, which means the goodness of the threshold energy estimation of $\sim$ 600 GeV.

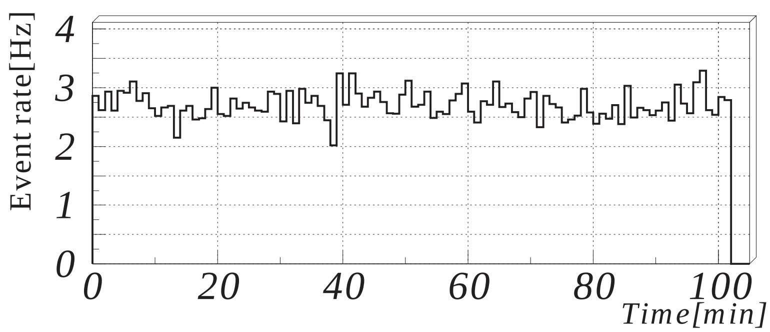

Figure 6.4: Time variation of the event rate of OFF-source run (one night).

6.1.3 Conversion Factor

In order to obtain the conversion factor between the number of photoelectrons and the ADC counts, we compare the sum of ADC counts obtained from OFF-source data (it means cosmic-ray events) and the sum of number of photoelectrons calculated from the simulated data of cosmic-ray protons.

Figure 6.5 shows the correlations between the number of hit PMTs (Nhit) and the sum of ADC counts of the OFF-source data, and that between the Nhit and the sum of number

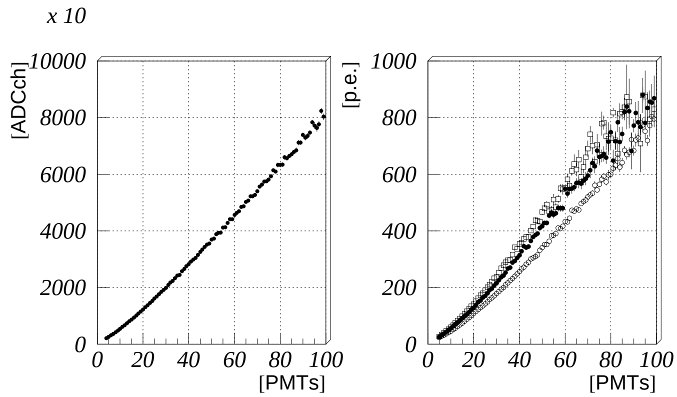

Figure 6.5: Sum of ADC counts and sum of number of photoelectrons v.s. number of hit PMTs. The left figure shows the correlation between the sum of ADC counts and Nhit obtained from the OFF-source data of this observation. The right is that between the sum of number of photoelectrons and Nhit (filled circles) simulated for cosmic-ray protons (500 GeV $\sim$ 10 TeV). The blank circle and square are the case assuming the fluctuations of twice and a half of NSB photons, respectively. and a half NSB photons.

of photoelectrons simulated, where "hit" means that pulse height of the PMT exceeds over the threshold level of the discriminator. There is a good correlation between the amount of Čerenkov light of the EAS events and Nhit, which means that the measured sum of ADC have a good correlation with the Nhit. We applied a loose noise cut for both data, in which at least three adjacent PMTs exceeding over 300 ADCch and 3 p.e. are required, respectively. Here the systematic error by the uncertainty of the night sky background (NSB) are taken into account by varying from the half to twice of the standard value of NSB.

The variation of the ratio of the sum of ADC to the sum of photoelectrons as a function of the number of hit PMTs is shown in Figure 6.6. The region bellow 10 Nhits is considered to be affected by the uncertainty of the estimation of the hit threshold level mentioned in chapter 5.2.4. The flat distribution of the ratio indicates that the conversion factor is independent on the Nhit. Thus, the conversion factor was estimated to be 92^{+13}_{-7}[ADCch/p.e.] independently on the amount of Čerenkov light of the EAS events, where systematic errors are estimated by changing the amount of the expected NSB in the simulation.

6.2 Noise Cut

Before the imaging analysis, all the calibration procedures were carried out: for example, adjustment of the pedestal and the relative gain for ADCs run by run, correction of the time-walk

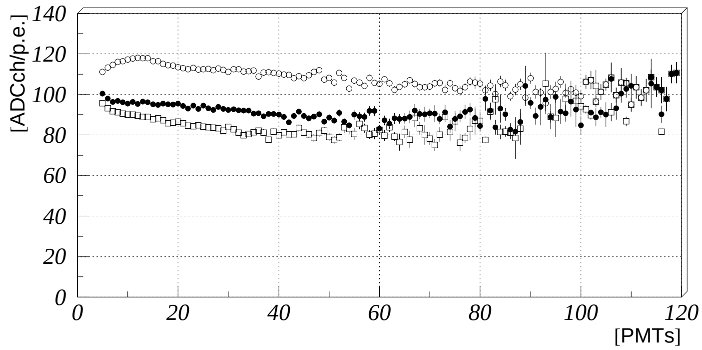

Figure 6.6: Ratio of the sum ADC to the sum photoelectrons v.s. number of hit PMTs. The blank circle and square are the case assuming the fluctuations of twice and a half of NSB photons, respectively. and a half NSB photons.

effect and the timing averages for TDCs event by event, as described in chapter 5.2.

In order to examine the conditions of the observations, loose event selections were carried out, removing obvious noise events coming from the electronics noise and the environment transient light.

Sometimes high gain PMTs were found while checking the count rate of PMT, TDC hit distribution or ADC distribution. As these PMTs often deform the shape of the image, they have to be removed before any noise cut.

In general, 10m class large Čerenkov telescope includes large NSB photons; for the CANGAROO-II 10m telescope, about 50 $\sim$ 200 photons in each event (as described in chapter 5.2.4). Therefore, only a small part of the PMTs contains Čerenkov photons from an EAS, whereas almost all of PMTs contain only NSB photons. Since these NSB photons also deform an image of the EAS, we should remove them by using the following cuts before proceeding to the image analysis.

The arrival timing of the Čerenkov photons are used at first. There are two components in the distribution of TDC start timing: the peak by the signals of the Čerenkov photons over the flatter distribution due to the NSB photons as shown in Figure 6.7. Timing of Čerenkov photons on the ground from the EAS concentrates within 10 $\sim$ 20 nsec at FWHM. In order to avoid the over cut of the photons of the EAS events, the photons within $\pm$25nsec at the peak of the timing distribution are required (Figure 6.7).

Second, the electronics noises due to the saturation of the ADCs were removed. The unknown current sometimes flows in the signal line, then the ADC saturates and returns a large value. Also this noise rarely hits a TDC. In order to remove the events having this noise, we use a correlation between the sum of ADCs and the number of hit PMTs (Figure 6.9). The concentration of the events including noises is apparent, and the following region in this plot is rejected.

$$\begin{cases} \text{sumADC} & > & 25000 \\ & \text{and} & \\ \text{sumADC} & > & 2000 \times \text{Nhit} - 25000 \end{cases}. \tag{6.4}$$

On the other hand, the photons from the bright star also deform the image, and this was removed using the scaler counts. The pixel, of which scaler count rate exceeds 4σ above its usual average, are removed from the image analysis.

Here we must comment about the unusual serious light background source in this observation. In 1999, Australian government constructed a Detention Center near on the telescope site at the distance of 5 km south. The projector light of the center was so bright that the DAQ rate rose drastically (a few hundreds Hz) when the telescope azimuth turned to the direction of the center. Therefore, in this observation, we had to increase the threshold level of noise cut as high as 10.5 p.e., in order to remove the bright background photons.

After these noise cuts, almost all the PMTs include Čerenkov photons, but these still remain a little hit PMTs by single NSB photons. In order to remove these PMTs, the clustering for hit PMTs is required for the image, where isolated PMT hit by NSB photons or noise of electronics are removed. Finally clusters which have at least 4 adjacent hit PMT are only selected, Clusters which do not satisfy with above requirement are classified to isolated PMTs and are eliminated. When an event contains multiple clusters, we use only one cluster having maximum number of photoelectrons; not maximum number of hit PMTs, since Čerenkov photons generated from a gamma-ray is generally concentrated more than that from hadronic EAS.

6.3 Selection of Gamma-Ray like Events

In this analysis, the NE-rim of SN1006 is treated as a point source according to the result of the CANGAROO 3.8m telescope [68]. We apply the standard image cut technique [16] [78] described in chapter 3.3. Conventional imaging parameters of "Alpha", "Distance", "Length" and "Width" are used. "Conc" is not used, since the distribution of "Conc" varied drastically by the amount of the Čerenkov photons. It seems due to the fine pixel of 0.1 degree of the camera.

In this analysis a new parameter "Eratio" was adopt to select the major part of the shower in the complex image. This parameter is defined as the ratio between the most energetic (having the largest photoelectrons) cluster and all clusters in one image.

$$\text{Eratio} = \frac{E_{\text{max}}}{\sum^{all} E} \tag{6.5}$$

In order to avoid over-cut, the selection criterion of "Eratio" was determined loosely;

$$\text{Eratio} > 70\%. \tag{6.6}$$

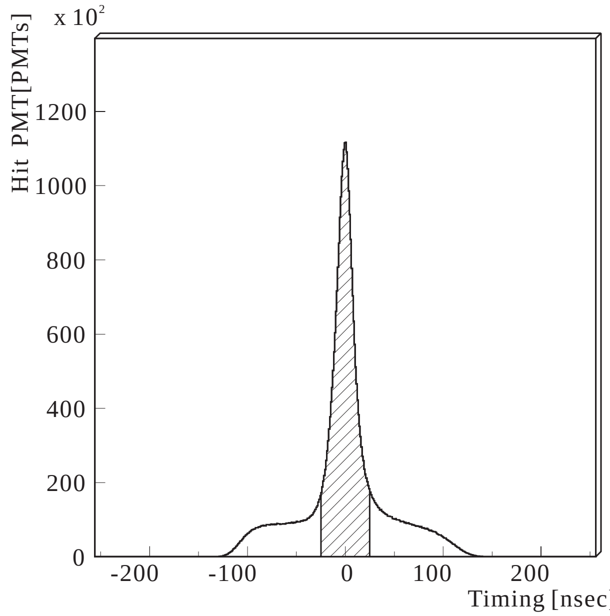

Figure 6.7: Selected region of arrival timing distribution. There exists two components; the peak by the signals of the Čerenkov photon and the flat distribution due to the NSB photons. This timing distribution is already corrected for time-walk and relative timing. The hatched region is selected for analysis.

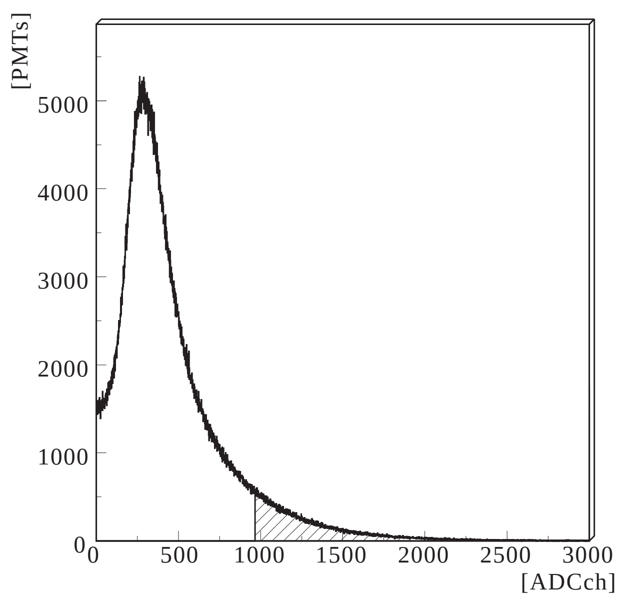

Figure 6.8: Selected region of ADC distribution. The hatched region is selected for analysis.

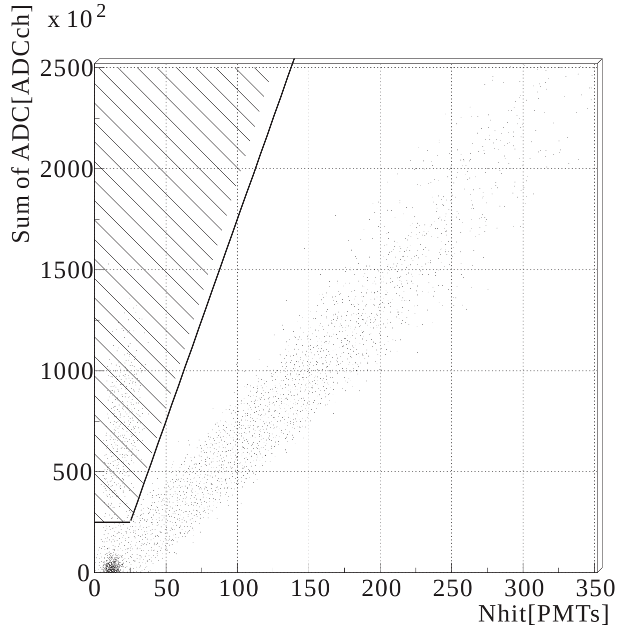

Figure 6.9: Correlation between the number of hit PMTs (Nhit) and the sum of ADC value of every event. The hatched region of which the noise events appear is rejected from analysis.

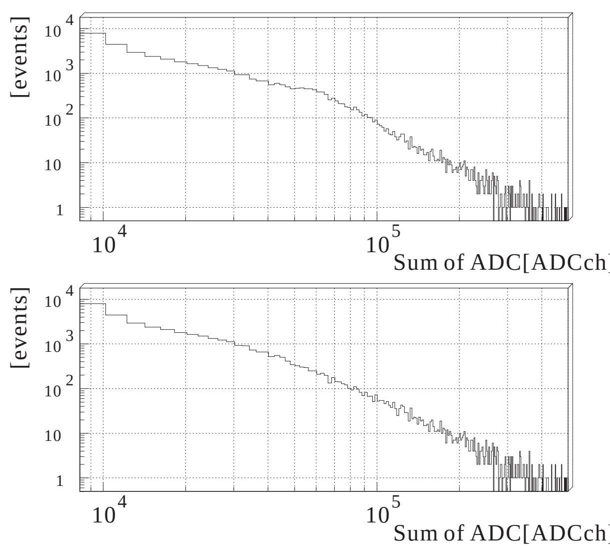

Figure 6.10: Effect of the noise rejection on the spectrum. These histograms are the spectra of the sum of ADC before (the upper figure) and after (the lower one) cutting the electronics noise. The peak of region around $\sim 10^5$ due to the noise is rejected.

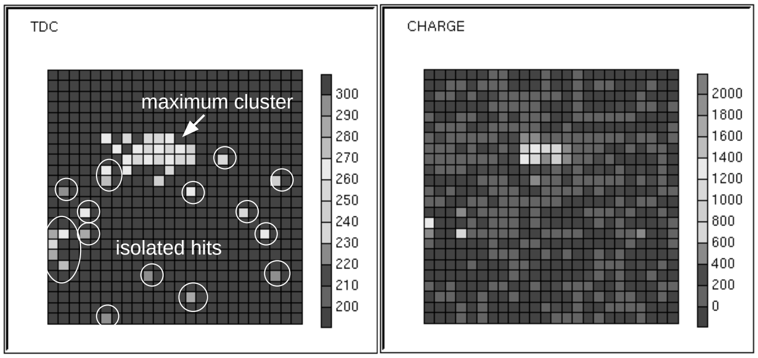

Figure 6.11: Typical cluster and isolated pixel. The upper and the lower figures show the TDC start timing and the ADC charge, respectively. Less than 4 adjacent cluster was rejected, and only the maximum cluster was used for the image analysis.

After selecting the most energetic cluster, image parameters were calculated only for this cluster.

The image survived noise cut was fitted to an elliptical shape, and the image parameters defined in chapter 3.3.2 were calculated for each event.

Some imaging parameters were calculated by the Monte Carlo simulation for gamma-ray events, and also those for hadronic events using the data of OFF-source run. On the basis of obtained parameter distributions shown in Figure 6.12, the selection criteria for the enhancement of gamma-ray signals from a point source were determined as follows:

$$\text{Distance}' < 1.20, \tag{6.7}$$

$$0.40 < \text{Distance} < 1.20, \tag{6.8}$$

$$0.06 < \text{Length} < 0.40, \tag{6.9}$$

$$0.05 < \text{Width} < 0.20, \tag{6.10}$$

$$\text{Alpha} < 15.0. \tag{6.11}$$

Those selection criteria are similar to the imaging cuts used by other groups. In principle, the "Length" of image of gamma-ray EAS is not longer than "Distance", since the development of the gamma-ray EAS image starts from the source position. Therefore, the following criterion was added to the selection criteria;

$$\text{Length} < \text{Distance}. \tag{6.12}$$

The variation of the "Alpha" distributions by sequential application of these selections can be seen in Figure 6.13.

Since cosmic-rays come isotropically, the "Alpha" distribution of the background images should be flat if the field of view is sufficiently larger than the image size. However, before the

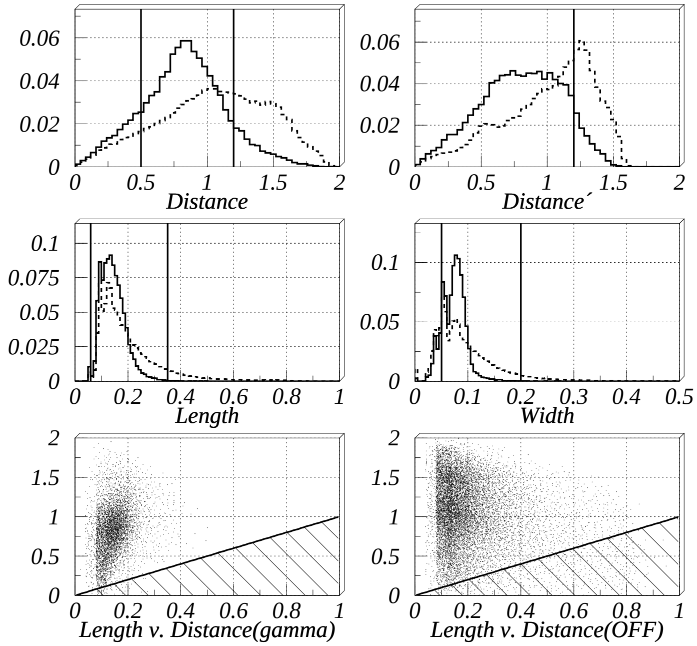

Figure 6.12: Selection criteria of the image parameters for the gamma-rays.

"Distance′" selection, the "Alpha" distribution is a flat. This is due to the boundary effect of the limited field of view. Using "Distance′" selection, this effect disappears and the flat "Alpha" distribution is obtained (Figure 6.13).

In the imaging method, the "Distance" of the gamma-ray EAS images has a positive correlation with the distance between the shower axis and the telescope axis (called "impact parameter"). Therefore, the upper limit for the "Distance" roughly represents the outer boundary of the detected EAS in the Čerenkov photon pool. Then the image of a gamma-ray EAS becomes an almost circular image rather than an elliptical one as its impact parameter closing to the center. Since such images cannot indicate the EAS direction accurately, the lower "Distance" events were rejected.

Above cuts do not consider the dependence of the image parameters on the energy of primary gamma-ray (shown in Figure 6.14). In order to enhance gamma-ray signals, we applied the image cut criteria depended on the charge of each event. Then the data was divided in six energy regions with the sum of ADCs, and adopt the energy dependent image cut of "Length"" and "Width" for each energy bin. Used image cut parameters are summarized in Table 6.1.

Even after above cuts, the cosmic-ray events cannot be rejected completely, and still events remaining are mostly background events. Therefore, the significance level of the detected gamma-

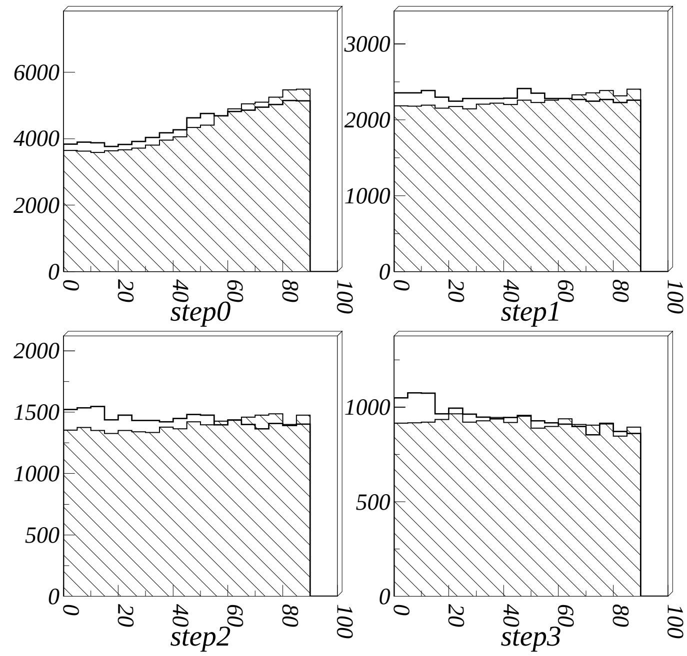

Figure 6.13: Variation of "Alpha" distributions with image parameter cut. The distributions are after noise cut (step 0), Distance′ cut (step 1), Distance cut (step 2), and Length and Width cut (step 3), respectively. The significance of the excess is 5σ in step 3.

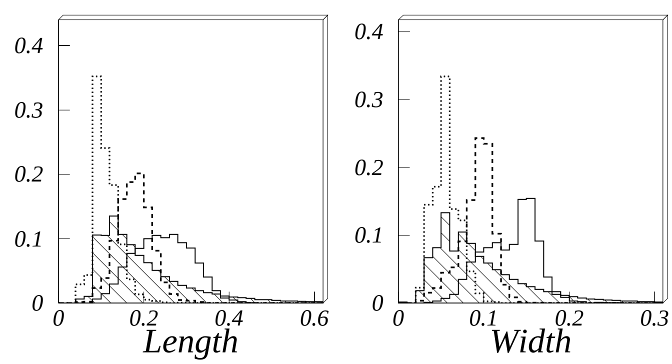

Figure 6.14: Energy dependence of image parameters. The hatched histogram are distribution of the OFF-source. The solid line, dashed line and break line are those of the gamma-ray simulation of 10 TeV, 3 TeV and 1 TeV, respectively.

Sum of the ADC [kch]	Length	Width
~ 5	Length < 0.15	Width < 0.12
$5 \sim 10$	Length < 0.15	Width < 0.12
$10 \sim 20$	Length < 0.30	Width < 0.17
$20 \sim 40$	Length < 0.34	Width < 0.20
$40 \sim 80$	Length < 0.41	Width < 0.25
$80 \sim$	Length < 0.41	Width < 0.30

Table 6.1: Image cut criteria for each energy bin.

ray signals due to the enhancement around 0 degree, has to be compared with the statistical fluctuation of the background events. When $N_{\rm ON}$ and $N_{\rm OFF}$ events are defined to be those within 15 degrees (selection criterion for the "Alpha") in the "Alpha" distribution of ON- and OFF-source data, respectively, the number of observed gamma-ray signals is

$$N_{\rm sig} = N_{\rm ON} - \langle N_{\rm BG} \rangle = N_{\rm ON} - \beta N_{\rm OFF}, \tag{6.13}$$

where $\langle N_{\rm BG} \rangle$ and β are the expected number of background events included in $N_{\rm on}$ and the ratio of the ON- and OFF-source exposure time, respectively. Here, $N_{\rm ON}$ and $N_{\rm OFF}$ are estimated using the region of criterion for "Alpha". Then the standard deviation $\sigma_{\rm sig}$ of the signal $N_{\rm sig}$ is

$$\sigma_{\rm sig}^2 = \sigma_{\rm ON}^2 + \beta^2 \sigma_{\rm OFF}^2 = N_{\rm ON} + \beta^2 N_{\rm OFF}, \tag{6.14}$$

where $\sigma_{\rm ON}$ and $\sigma_{\rm OFF}$ are the expected standard deviations of the ON- and OFF-source counts, respectively. This definition of the normalization factor by observation time occurs the inconsistency with the normalization method using the number of events, applied in the image analysis. However the time-normalization method is better, the normalization using the number of events was adopt here.

The significance level S is defined as the ratio of the excess counts above background to its standard deviation as follows,

$$S = \frac{N_{\rm sig}}{\sigma_{\rm sig}} = \frac{N_{\rm ON} - \beta N_{\rm OFF}}{\sqrt{N_{\rm ON} + \beta^2 N_{\rm OFF}}}. \tag{6.15}$$

This estimation of the significance level was investigated by Li and Ma [31] using Monte Carlo simulations. They showed that it is consistent with the Gaussian probabilities for the case $\beta = 1$, but is systematically underestimated and overestimated for the case $\beta < 1$ and $\beta > 1$, respectively, using the hypothesis that only background events have been detected.

For the events passing through these cuts, gamma-ray signals from the NE-rim of SN1006 should be enhanced as a positive excess around 0 degree in the "alpha" distribution of the ON-source events against the OFF-source events. Since "Alpha" of the gamma-ray image concentrates within $\sim 20^\circ$, the OFF-source events were normalized to the ON-source events, comparing with the number of events at $30° <$ Alpha $< 90°$; in order to avoid over-estimation, the region of $20° <$ Alpha $< 30°$ was not used in the above normalization.

Total "Alpha" distribution obtained by above event selections, is shown in Figure 6.15. The statistical significance calculated for the total counts after event selection is 7.0σ, and the number of excess events with statistical error was obtained to be 558 ± 79.5. Figure 6.16 presents the "Alpha" sub-distributions divided into six energy regions. Table 6.2 shows the excess and significance level for each energy region.

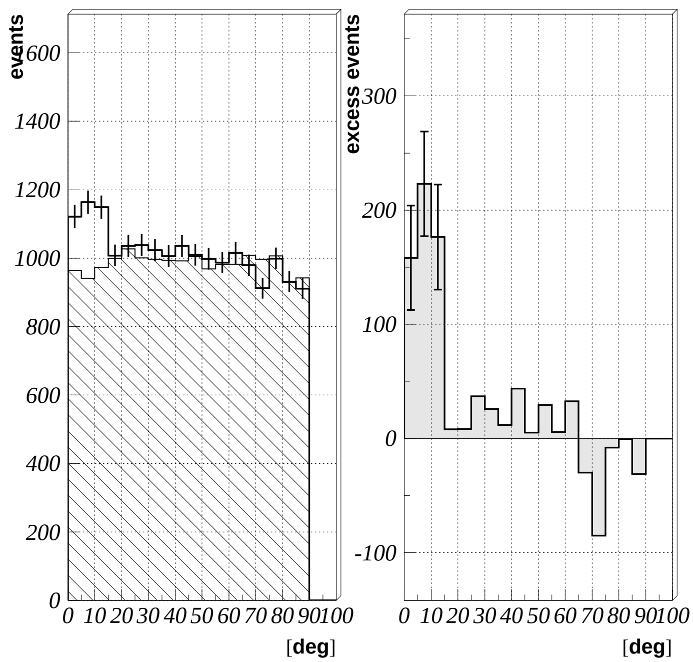

Figure 6.15: Excess signals of gamma-rays. The left "Alpha" distribution for ON-source run (the blank histogram with error bars) and for OFF-source run (the hatched one). The right histogram is the background subtracted signal.

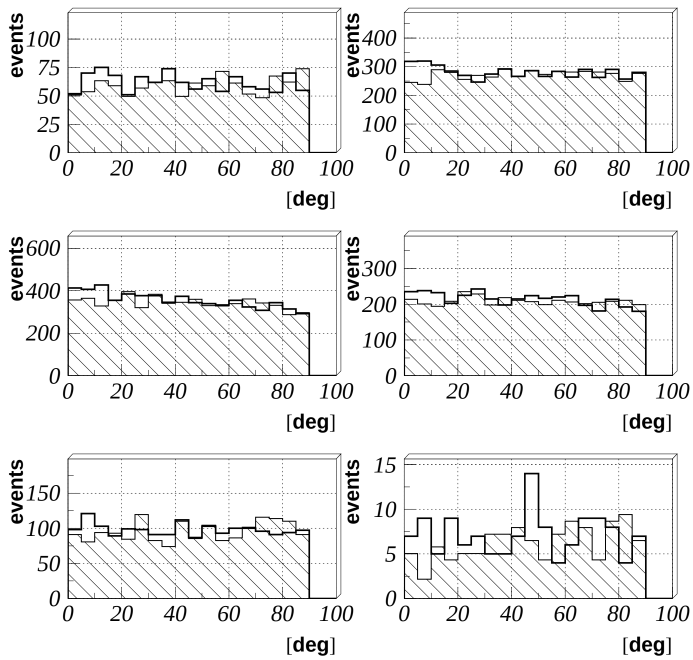

Figure 6.16: "Alpha" sub-distributions divided into six energy bins based on the sum of ADCs.

Sum of the ADC [kch]	Excess	Significance level
~ 5	29.3 ± 19.1	1.5σ
$5 \sim 10$	170 ± 41.4	4.1σ
$10 \sim 20$	197 ± 47.9	4.1σ
$20 \sim 40$	96.9 ± 36.3	2.7σ
$40 \sim 80$	56.9 ± 24.2	2.3σ
$80 \sim$	7.99 ± 5.83	1.4σ
TOTAL	558 ± 79.5	7.0σ

Table 6.2: Variation of excess signals. The significance levels are calculated using Li-Ma method.

Chapter 7

Results

7.1 Integral Flux

In order to obtain the gamma-ray flux corresponding to the excess obtained with the image analysis, the effective area of our telescope and energy estimation for detected gamma-rays were investigated by the Monte Carlo simulation.

The effective area $S_{\rm eff}(E)$ is defined as a function of energy E as follows:

$$S_{\rm eff}(E) = \frac{N_{\rm select}}{N_{\rm all}} \times \pi r_\gamma^2 \tag{7.1}$$

where, $N_{\rm all}$ and $N_{\rm select}$ are the numbers of gamma-ray events generated by the simulation and that selected by the analysis program, respectively. The lateral distribution of Čerenkov photons from gamma-ray EAS is almost flat up to $\sim$ 150m radius in an EAS distribution. In the simulation, gamma-rays were injected in the region within $\frac{250}{\cos\theta}$m radius from the telescope, where is enough larger than the distribution of Čerenkov photons (θ is the zenith angle of the injecting direction). Figure 7.1 shows the expected effective area of the CANGAROO-II 10m telescope, using the same analysis, as a function of the energy of gamma-rays emitted from a point source.

The direction of the simulated gamma-ray EASs is set at the zenith angle of 20 degree according to the observation of SN1006. Also the index of power-law spectrum of gamma-rays was assumed to be -2.3 by the previous result of the index observed by the CANGAROO 3.8m telescope around 2 TeV [68]. The threshold energy for the gamma-ray detection is defined to be the energy at the maximum differential flux. As shown in Figure 7.2, the threshold energy for the observed integral gamma-ray flux is determined to be about 1.5TeV.

The integral flux $F_{\rm Int}$ is defined as follows,

$$F_{\rm Int}(> E_{\rm th}) = \frac{N_{\rm sig}}{T\overline{S_{\rm eff}}}, \tag{7.2}$$

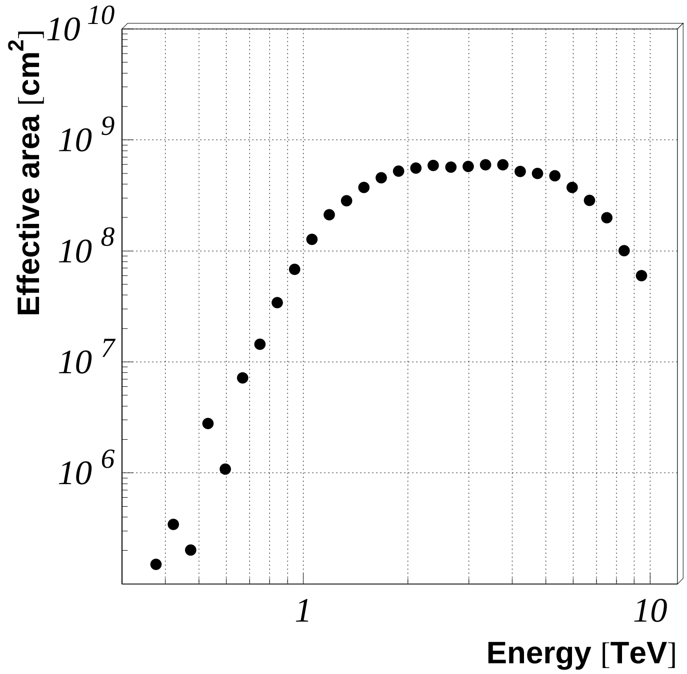

Figure 7.1: Effective area as a function of the energy of gamma-rays.

where $N_{\rm sig}$, T and $\overline{S_{\rm eff}}$ are the number of gamma-ray signals, the observation time, and the averaged effective area, respectively. In order to calculate the integral flux of gamma-rays, it is needed to estimate the averaged effective area. and The averaged effective area $\overline{S_{\rm eff}}$ is calculated as follows,

$$\overline{S_{\rm eff}} = \frac{\int_{E_{\rm th}}^{\infty} S_{\rm eff}(E) E^{-\alpha} dE}{\int_{E_{\rm th}}^{\infty} E^{-\alpha} dE}, \tag{7.3}$$

where $S_{\rm eff}(E)$ is the differential effective area (Figure 7.1), and α is the assumed power-law index of the differential flux. The integral flux was estimated to be

$$F_{\rm Int}(> 1.4{\rm TeV}) = (6.1 \pm 0.9) \times 10^{-12} \quad [{\rm photons} \cdot {\rm cm}^{-2} \cdot {\rm sec}^{-1}], \tag{7.4}$$

the parameter used in this estimation is summarized in Table 7.1.

7.2 Differential Flux

The differential spectrum was estimated as follows. First, gamma-ray events were simulated between 100 GeV and 10 TeV, assuming a differential power-law index of -2.3.

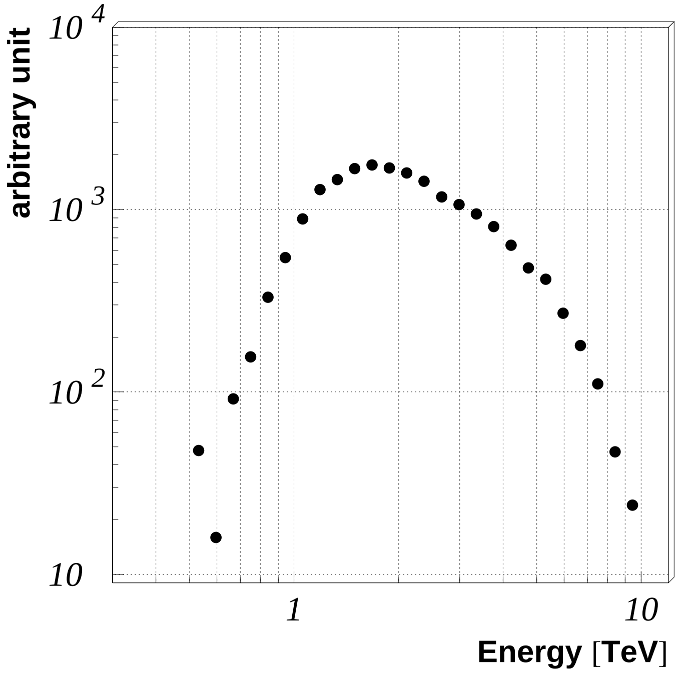

Figure 7.2: Definition of the threshold energy. The threshold energy for the gamma-ray detection is defined to be the energy at the maximum differential flux. By assuming spectrum index -2.3 from the CANGAROO 3.8m telescope result, the threshold energy for this analysis was estimated to be ~ 1.4 TeV.

Threshold energy; $E_{\rm th}$	1.4 TeV
Excess signals; $N_{\rm sig}$	557 ± 79.5
Averaged effective area; $\bar{S}_{\rm eff}$	$4.84 \times 10^8 {\rm cm}^2$
Observation time; T	1.88×10^5 sec

Table 7.1: Parameters for the estimation of the integral flux.

For the every energy bin of the differential spectrum, $\overline{S_{\rm eff}}dE$ and averaged energy $\overline{E}$ is estimated from the simulation result. Using these values, a differential flux was obtained at each energy bin as follows,

$$J(\bar{E}) = \frac{N_{dE}}{T\bar{S_{\rm eff}}dE}. \tag{7.5}$$

The averaged energy of each energy bin is estimated by same way as the integral flux estimation. Using the only parameters over 2σ signals of Table 7.2, the resultant differential spectrum $F(E)$ between 1.25 and 3.3 TeV is written as

$$F(E) = (7.4 \pm 2.0) \times 10^{-12} (E/1\mathrm{TeV})^{-2.3\pm0.4} \quad [\mathrm{cm}^{-2} \cdot \mathrm{sec}^{-1} \cdot \mathrm{TeV}^{-1}], \tag{7.6}$$

where the errors are statistical only.

Averaged energy $\bar{E}$[TeV]	Excess signals N_{dE}[photons]	Effective area $\overline{S_{\rm eff}}dE$[cm^2 $\cdot$ TeV]	Differential Flux [cm^{-2} $\cdot$ sec^{-1} $\cdot$ TeV^{-1}]
1.00	29.3 ± 19.1	2.5×10^7	$(6.2 \pm 4.1) \times 10^{-12}$
1.25	170 ± 41.4	2.3×10^8	$(4.0 \pm 1.0) \times 10^{-12}$
1.70	197 ± 47.9	3.6×10^8	$(2.9 \pm 0.7) \times 10^{-12}$
2.50	96.9 ± 36.3	6.0×10^8	$(8.6 \pm 3.2) \times 10^{-13}$
3.30	56.9 ± 24.2	7.5×10^8	$(4.0 \pm 1.7) \times 10^{-13}$
5.00	7.99 ± 5.83	1.0×10^9	$(4.3 \pm 3.1) \times 10^{-14}$

Table 7.2: Estimation of the differential flux.

7.3 Systematic Errors

Some systematic errors concerned with the absolute flux of gamma-rays were estimated.

The reflectivity of the mirrors was considered to degrade during the observation (the reflectivity can be recovered by water washing). The uncertainty of the reflectivity was estimated $\sim$ -10 % from the several direct measurements of the reflectivity carried out in the observation. This uncertainty affects the effective area for the EAS, namely the estimations of the flux and the threshold energy. The degradation of -10% generates the uncertainties of 13% and 14%, for the estimation of flux and the threshold energy, respectively.

Also the uncertainty of the trigger condition is estimated. The threshold level of the discriminator for "Lsum" signal is set 3 p.e.. However, as mentioned in chapter 5.2.4, this threshold level has the uncertainty of ± 0.5 p.e. from the uncertainty of NSB photons. In our trigger schema addition, five PMTs exceeding the Lsum threshold are required for the event trigger, and its uncertainty is ± 1 PMT. The uncertainties of these effects from the above two uncertainties summarized in Table 7.3.

	uncertainty	flux errors(%)	energy errors(%)
reflectivity	$\sim -10\%$	-13	-14
trigger condition			
Lsum threshold	(3.5 ± 0.5) p.e.	± 2	$\pm$ 3
Lsum hit PMTs	(5 ± 1) PMTs	$\pm$ 1	$\pm$ 1
conversion ratio	92^{+13}_{-5} ADCch		$\pm$ 29
image cut	$\pm$ 10%	$\pm$ 18	
total		± 22	± 32

Table 7.3: Systematic errors on the flux and the energy threshold. The total systematic errors were obtained by adding those errors quadratically.

The error of the conversion ratio of the ADC counts to the number of photoelectrons mainly contributed to the uncertainty of the estimation of the absolute energy of detected gamma-ray events. The uncertainty from this systematic error of the conversion factor (mentioned in chapter 6.1.3) was estimated to be 29% for the threshold energy.

The number of observed gamma-rays are estimated from the peak of "Alpha" distribution and hence its number fluctuates due to the method of the background reduction (imaging cut). This uncertainty of the number of the gamma-ray events was estimated to be $\pm 18\%$ by changing cut parameters (here, "Length" and "Width") within reasonable range.

These systematic errors give the uncertainties for the integral and the differential fluxes, and the threshold energy, which are summarized in Table 7.3. By adding those errors quadratically, the total systematic errors are estimated $\sim 22\%$ on the flux and $\sim 32\%$ on the threshold energy, respectively.

7.4 Significance Map

As mentioned in chapter 6, the source of gamma-rays was assumed to come from the NE-rim as a point like source. Since there is possibility that the region of TeV gamma-ray emission is extended over the point spread function(PSF) of the telescope (Figure 7.3), the spatial distribution of detected gamma-rays from SN1006 should be studied. The region within about 2 degree from the center of SN1006 was searched by the following method.

The field of view around SN1006 was divided into a grid with the pitch of 0.04 degree, and image parameters were calculated at every grid cell for both ON- and OFF-source data. Then the significance of the "Alpha" peak, which is residual of the ON-source over the OFF-source, passing the gamma-ray selection criteria are obtained at each grid point. The 2-dimensional histogram of the resultant significances. is shown in Figure 7.4.

The PSF of the CANGAROO-II 10m telescope was estimated to be 0.24 degree radius (Figure 7.3), using the following method. The gamma-ray events emitted from a point like source were simulated taking into account of the observation condition, and its image parameters were calculated at various position similarly to the above method for the significance map. The obtained 2-dimensional distribution of the reconstructed direction was fit to the Gaussian distribution, and the PSF is defined as the standard deviation.

In Figure 7.4, the hard X-ray ($2 \sim 7$ keV) of the *ASCA* data are also overlaid. It is apparent that the region showing TeV gamma-ray emission appears mainly around the NE-rim, and the spatial distribution of the significance is not extended over the PSF of the telescope. In addition, the point with the highest significance is consistent with the maximum flux point in hard X-ray and also with the previous result of the CANGAROO 3.8m telescope.

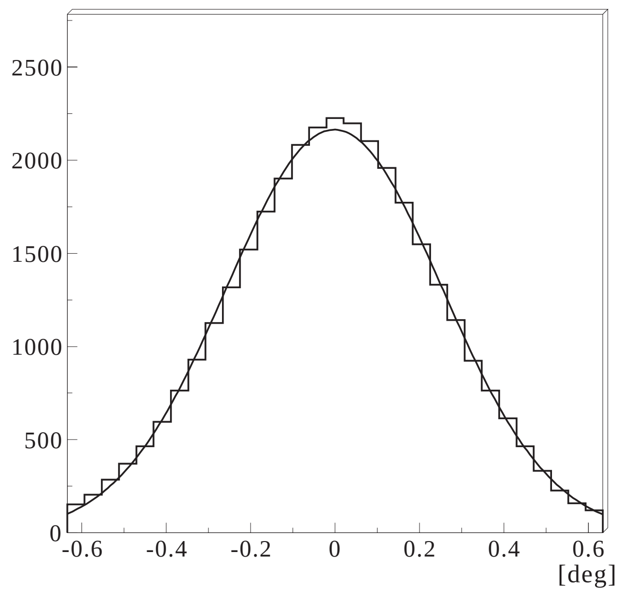

Figure 7.3: Point spread function of the CANGAROO-II 10m telescope. Fitting by Gaussian function, the PSF is estimated to be 0.24 degree radius.

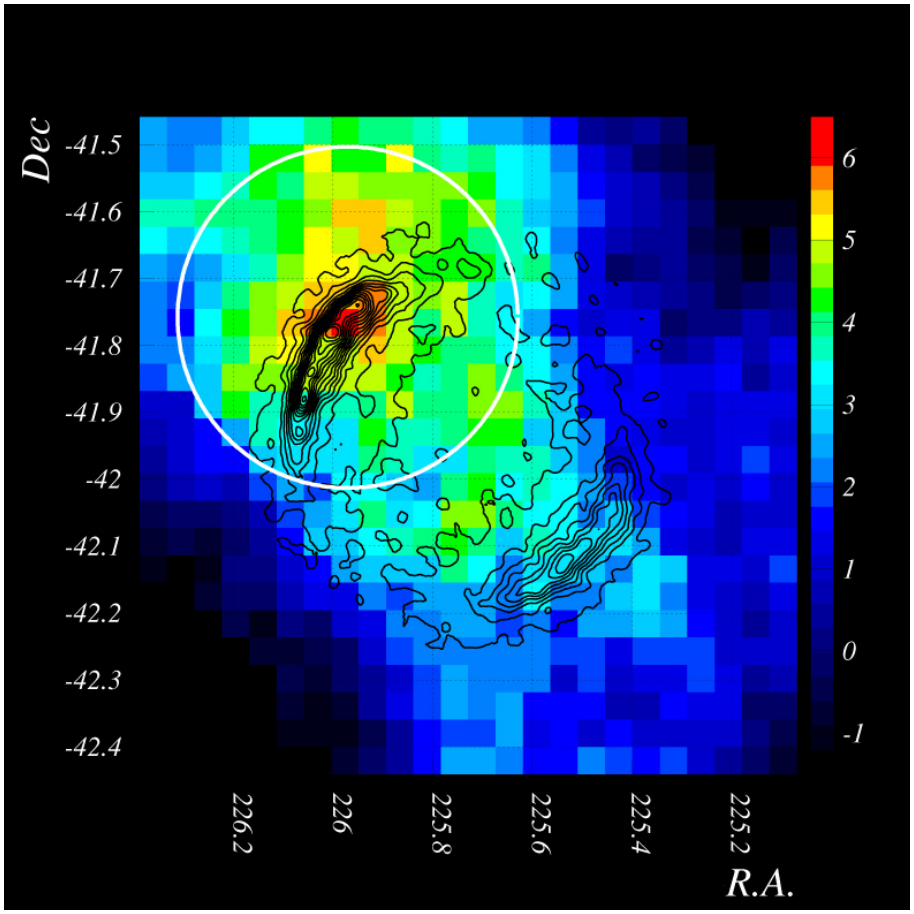

Figure 7.4: Significance map around SN1006. The hard X-ray (2–7 keV) flux of the ASCA data are overlaid (solid line), and the white circle of a 0.24 degree radius is the point spread function of the CANGAROO-II 10m telescope.

Chapter 8

Discussion and Conclusion

We have observed the NE-rim of SN1006 with the CANGAROO-II 10m telescope in April and May 2000, and successfully obtained the gamma-ray signals above ~ 1.5 TeV from the same position of the previous 3.8m results. The total observation time used in this analysis is 1.88×10^5 seconds for ON-source data and 1.62×10^5 seconds for OFF-source data. The integral gamma-ray flux I is estimated as follows:

$$I(E > 1.4\text{TeV}) = (6.1 \pm 0.9_{\text{stat}} \pm 1.3_{\text{sys}}) \times 10^{-12} \ [\text{photons} \cdot \text{cm}^{-2} \cdot \text{sec}^{-1}]. \tag{8.1}$$

Figure 8.1 shows the integral fluxes obtained by the CANGAROO-II 10m and 3.8m telescope.

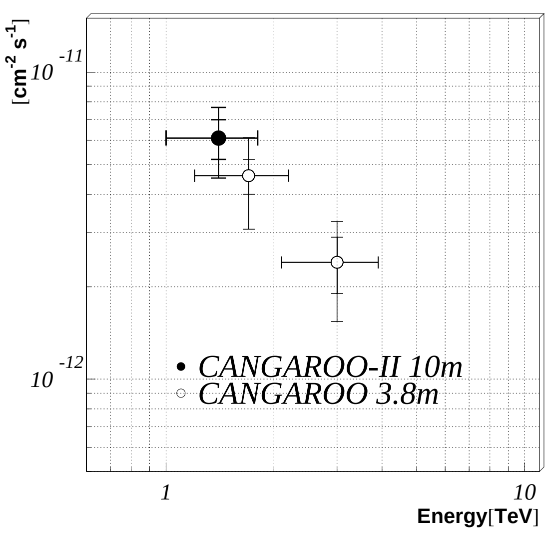

Figure 8.1: Integral spectrum obtained by CANGAROO telescopes. The resultant flux of this work is consistent with the previous results.

The differential flux $F(E)$ is also obtained between 1.25 and 3.3 TeV as follows;

$$F(E) = (7.4 \pm 2.0) \times 10^{-12} (E/1\text{TeV})^{-2.3\pm0.4} \quad [\text{cm}^{-2} \cdot \text{sec}^{-1} \cdot \text{TeV}^{-1}]. \tag{8.2}$$

Figure 8.2 shows the differential fluxes obtained by the CANGAROO-II 10m and 3.8m telescope. The flux obtained in this work is consistent with the previous results within error.

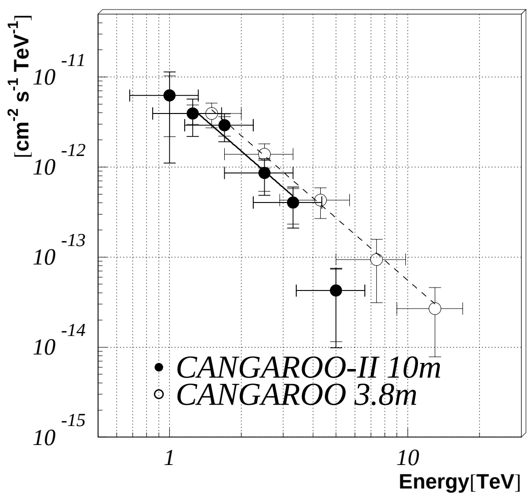

Figure 8.2: Differential spectrum obtained by CANGAROO telescopes. The filled marks and the solid line are the observed and the fitted flux in this work, respectively. The blank marks and the dashed line are the previous results of the CANGAROO 3.8m telescope. The resultant flux of this work is consistent with the previous results.

This is the third time to detect TeV gamma-rays from SN1006 observed by the independent new telescope, which confirms the emission of TeV gamma-ray from SN1006. It also provides a convincing evidence for the shock acceleration mechanism up to $\sim$ 100 TeV in a SNR.

We made the significance map around SN1006, calculating the signal excesses for each grid of which the field of view was divided. The extension of the TeV gamma-ray emission region observed is consistent with the PSF of the telescope of $\sim$ 30 arcmin (Figure 7.4), and of which maximum peak point matches that of the hard X-ray observation.

From the non-thermal X-ray observation, the detected TeV gamma-rays are supposed to be generated by IC scattering of very high-energy electrons on 2.7K CMS photons as seed photons. One model calculates the expected TeV gamma-ray spectrum based on the observed radio and X-ray spectra, assuming the power-law and the exponential cut-off energy spectrum for electrons [45]. The distribution of primary momenta E of accelerated electrons, which are accelerated in the shock wave by the first-order Fermi mechanism, is written in this model,

$$\frac{dN}{dE} \propto \left(\frac{E}{mc^2}\right)^{-\alpha} \mathrm{e}^{-\frac{E}{E_{\max}}}, \tag{8.3}$$

where m and $E_{\max}$ are the mass and the maximum energy of accelerated particles. Unknown parameters in this formula are determined by fitting the observed radio and X-ray synchrotron spectra [58] [79] [51]. For electron acceleration, assuming that the radio and X-ray non-thermal fluxes are mainly due to synchrotron emission, the following values are obtained:

$$\alpha = -2.2, \tag{8.4}$$

$$E_{\max}\sqrt{B} = 101, \tag{8.5}$$

where $E_{\max}$ and B are in unit of TeV and μG, respectively. Figure 8.3 shows the several spectra expected of the IC model by varying the magnetic field with the differential flux obtained by the CANGAROO 3.8m telescope [70]. The ambient magnetic field of $4 \pm 1\mu$G seems to be most probable.

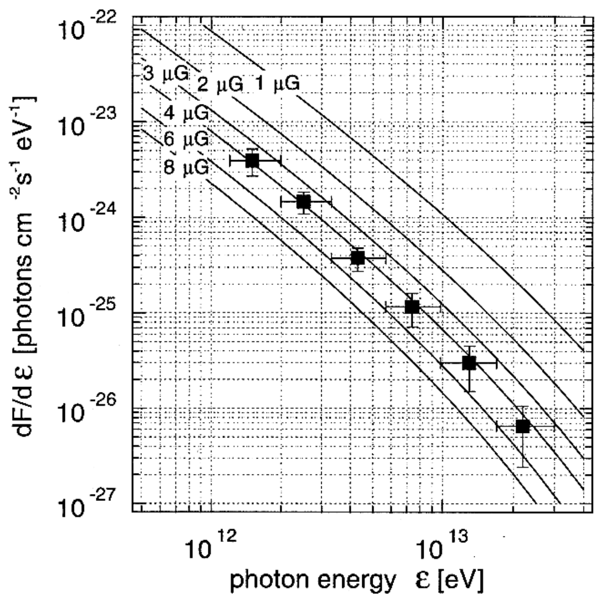

Figure 8.3: Observed differential spectrum from the NE-rim of SN1006, where only statistical errors are shown. In addition, spectra of TeV gamma-rays for several magnetic field strength B calculated by the IC model are presented [70].

In order to verify the origin of cosmic-rays, we have to obtain a clear evidence for acceleration of protons. The identification of the parent particles of TeV gamma-rays (electrons or protons) will be possible by observing a wide spectrum from sub to multi TeV region as shown in Figure 8.4. Flatter spectrum than -2.0 in TeV region is surely due to IC process, while that due to π^0

decay generated by collisions between ISM and high-energy protons is expected to be steeper than -2.0.

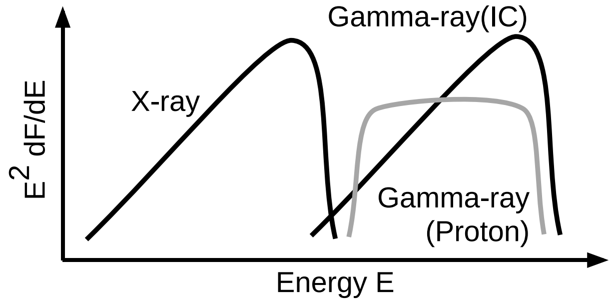

Figure 8.4: Typical energy spectra of synchrotron X-ray, IC TeV gamma-rays, and TeV gamma-rays due to π^0 decay.

The wide band energy spectrum from radio to TeV regions at the NE-rim of SN1006 and the model fitting are shown in Figure 8.5 [45]. The allowable spectrum of the gamma-rays generated by π^0 decay process, described in chapter 2.1, is also plotted in Figure 8.5, The π^0 decay model is difficult to satisfy both the EGRET upper limit and TeV flux, whereas the IC fitting spectrum can explain the observed spectrum quite well. In addition, from this fitting, the energy flux of gamma-rays at 300 GeV due to the IC process is estimated to be $\sim$ 4eV cm^{-2}sec^{-1} , which is lower than the upper limit reported by Durham group; $\sim$ 8eV cm^{-2}sec^{-1} [3].

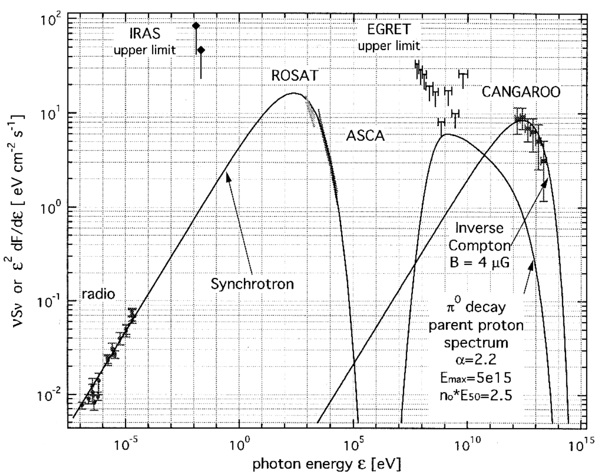

Figure 8.5: Multi-band spectrum of energy fluxes observed from the NE-rim of SN1006, where observed fluxes or upper limits of radio [58], infrared, soft X-ray [79], hard X-ray [51], GeV gamma-ray (EGRET archive data) and TeV gamma-ray [70], are presented. Solid lines are the fits based on the model of IC model and neutral pion decay.

XMM-*Newton* was the X-ray satellite launched in December 1999, having the three detectors of EPIC (European Photon Imaging Camera), RGS (Reflection Grating Spectrometer), and OM (Optical Monitor). The EPIC has two imaging camera of MOS (Metal-Oxide Semi-conductor) and PN-CCD camera. Recently, XMM-*Newton*/EPIC MOS observed the NE-rim of SN1006, and for the first time presented the spatial variation of the energy spectrum in X-ray around the NE-rim, and the cut-off energy of the synchrotron emission can be estimated at every point in the NE-rim [60] (Figure 8.6). From that result, the very strong variations of the cut-off energy were found in both the radial and azimuthal directions from the remnant center. The cut-off energy distribution along the radial direction from the center to the NE-rim monotonously increases up to the rim position (Figure 8.7). This indicates that the site of the particle acceleration is the shock front. In addition, the cut-off energy drastically varies along the rim from 0.1 to 1 keV, where the highest energy point is concentrated within the ~ 10 arcmin (Figure 8.8). This maximum position is consistent with the position of the maximum flux observed in hard X-ray by *ASCA*, while at the position observed the strongest intensity in radio, the cut-off energy was measured to be 10 times less than that of the maximum point. This maximum position is also consistent with the position showing the TeV gamma-ray emission in this work. The detected morphology of TeV gamma-rays in both 10m and 3.8m telescope strongly suggests the point-like emission at this point. If the cut-off energy of the synchrotron emission was less than 0.1 keV, the energy of IC gamma-ray flux from there would be quite lower than that detected by the CANGAROO-II telescope. Thus, the XMM-*Newton* result strongly supports the point-like emission of TeV gamma-rays from the NE-rim of SN1006 observed by 3.8m and 10m telescope.

We will construct the second 10m telescope, for the stereoscopic observation, and be in operation in this spring. This "CANGAROO-III" is a project to study celestial gamma-rays in the sub-TeV region, using an array of four 10m telescopes. A high angular resolution and a good rejection power of background EAS are provided by the stereoscopic observation.

The stereoscopic observation can determine the direction of a each EAS. An EAS image observed by a single telescope provides only the information about the plane defined by the EAS axis and the position of the telescope. However, the stereoscopic observation can determine the direction of the EAS, namely the direction of the gamma-ray, as a cross line of above two planes of two images observed for the same EAS from different positions (Figure 8.9, Figure 8.10).

Simulated performances of the angular resolution and the effective area of the stereoscopic observation by several 10m telescopes are shown in Figure 8.11 and 8.12 which were estimated for the design of the CANGAROO-III stereoscopic telescope. A real imaging ability with an angular resolution of $\sim 0.1^{\circ}$ around 600 GeV, a threshold energy of 100 GeV, and a sensitivity of $\sim 5 \times 10^{-13}\text{cm}^{-2}\text{sec}^{-1}$ at 500 GeV are expected [6] [10] [69]. In particular, the sensitivity is improved for a factor of ~ 10. In addition, the observation operated in "monocular mode", of

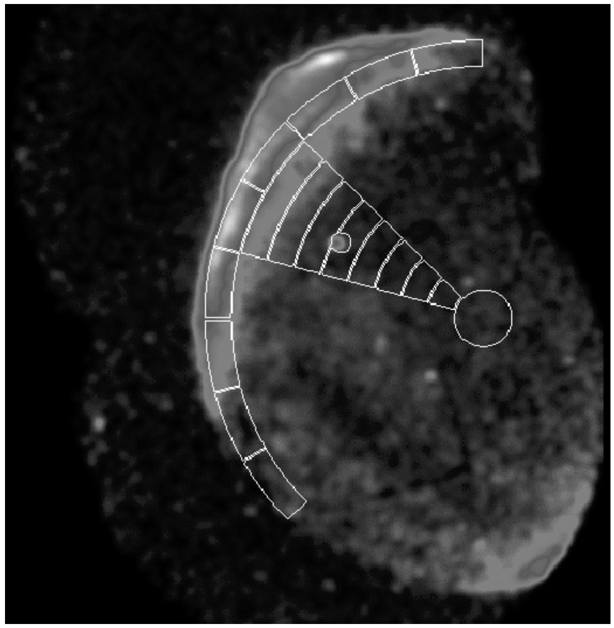

Figure 8.6: Image in X-ray of 2 $\sim$ 10 keV observed by XMM-*Newton* [60]. The analyzing regions for the radial and the azimuthal direction are shown as white grids.

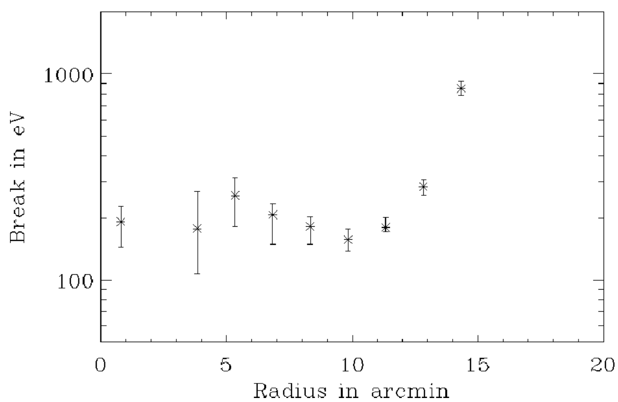

Figure 8.7: Distribution of the cut-off energy in the radial direction [60]. Each point corresponds to the radial grids in Figure 8.6. The cut-off energy of the synchrotron emission is highest at the rim (most right point).

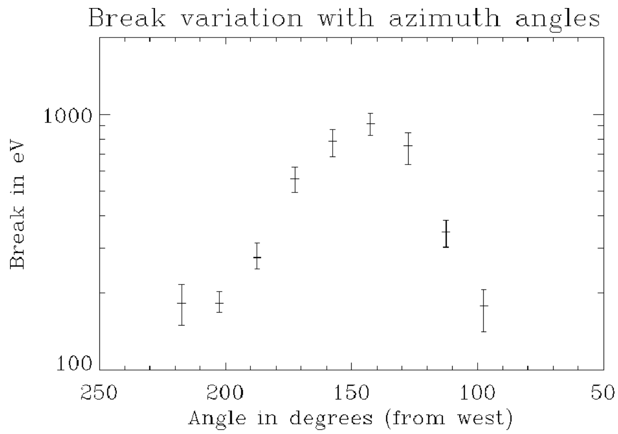

Figure 8.8: Distribution of the cut-off energy in the azimuthal direction [60]. Each point corresponds to the azimuthal grids in Figure 8.6. The cut-off energy of the synchrotron emission is not uniform along the NE-rim. The difference between the highest and the lowest cut-off energy reaches five times in the rim region.

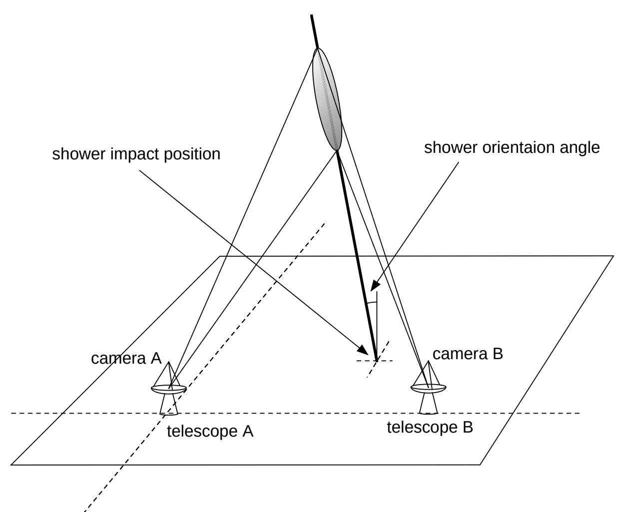

Figure 8.9: Schematic diagram of the stereo observation.

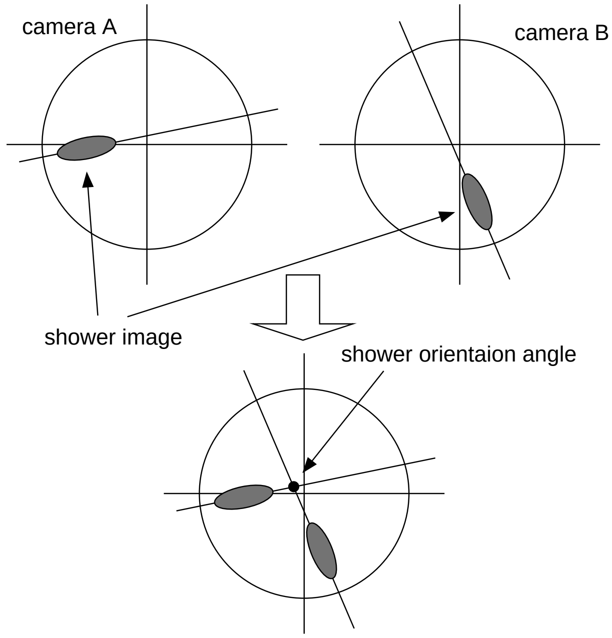

Figure 8.10: Overlaid images in the field of views of the two telescopes. observed from different angles in the stereo observation. A source direction is determined as a cross point of two axes of images.

which the telescopes of the array individually observe the source, can obtain the larger effective area and we can observe two (or more, number of telescopes) targets simultaneously.

Above improvement will drastically advance the study of TeV gamma-ray emissions from SNR, because the morphological study is inevitable for SNR, due to the complex structure of the gamma-ray emission region. The high angular resolution of the CANGAROO-III will reveal the detailed structure of TeV gamma-ray emission region of SN1006. SN1006 is a weaker TeV gamma-ray source detected so far. In particular, since the differential index of SN1006 is flatter than that of cosmic-rays, the gamma-ray signals in lower energy region become more difficult to detect due to the increase of background protons. In addition, the energy spectrum is considered to be much flatter below the peak energy of the IC process ($\sim$ 2 TeV). In order to catch weak signals, the high sensitivity of $\lesssim 10^{-12}$ in sub-TeV region is needed. Hence expected sensitivity of the CANGAROO-III will allow us to obtain the energy spectrum in the lower energy region.

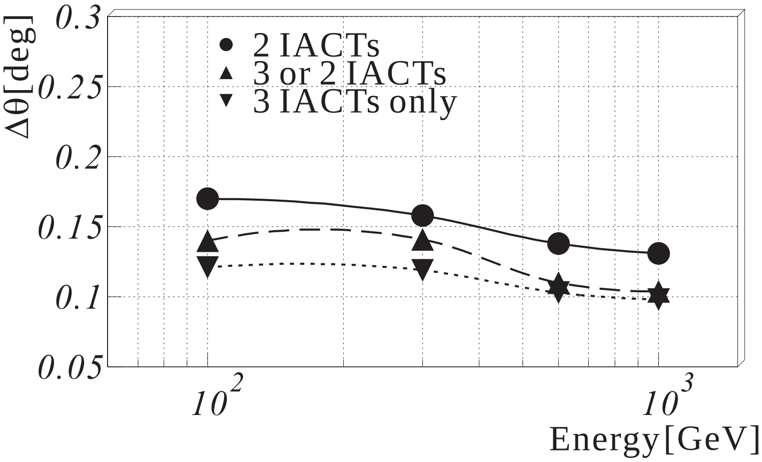

Figure 8.11: Simulated performance of an angular resolution for the CANGAROO-III. Three lines show the stereoscopic observation mode of two telescopes coincidence, three telescopes coincidence, and three or two telescope coincidence. This simulation was studied for the zenith.

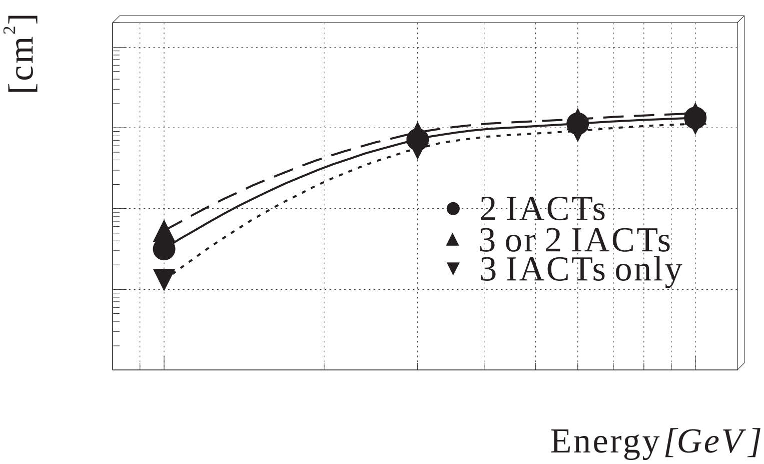

Figure 8.12: Simulated performance of an effective area for the CANGAROO-III. Three lines defined the same as above figure, and this simulation was studied for the zenith.

Acknowledgement

I would like to thank my supervisor, Prof. Toru Tanimori (Kyoto University) for his support over the past six years. I also wish to thank Prof. Yasushi Watanabe, Prof. Nobuyuki Kawai, Dr. Hidetoshi Kubo (Kyoto University), Dr. Hirokazu Ishino, Dr. Jun Kataoka for their support and encouragement.

I would like to thank Prof. Ryoji Enomoto (Institute for Cosmic Ray Research, The University of Tokyo;ICRR) and Prof. Masaki Mori (ICRR), for his suggestion in my research work.

I would also like to thank my colleagues in the University of Adelaide; Dr. John Patterson for his help during my stay in Woomera and Adelaide.

Thanks are due to Dr. Koji Sakurazawa, Dr. Hiroshi Muraishi (IPU), Dr. Masayo Moriya, Dr. Kimihiro Okumura (ICRR) and Ms. Junko Kushida, for the information in the analysis, Thanks are due to Akihiro Asahara (Kyoto University) and Kazuyoshi Takano for the information in observation data.

Thanks are also due to others who assisted me in the observations in Woomera; Mr. David Swaby (Adelaide), Ms. Rieko Suzuki (ICRR). All other colleagues in the CANGAROO group are given my best thanks.

I wish to thanks my colleagues in the Watanabe-Kawai group; Mr. Jun'ichi Kaneko, Mr. Hidetoshi Kakuno, Mr. Mikio Morii, Mr. Takanori Sakamoto, Mr. Nobuo Abe, Mr. Satoshi Koishi, Mr. Shotaro Yanaka, Mr. Hiroshi Nishihama, Mr. Nishimura, Mr. Fumiyasu Ohno, Mr. Takayoshi Harada, Mr. Yuuri Serino, Ms. Rie Sato, Ms. Chino Iizuka, and Ms. Akiko Ohno, for their encouragement. I also wish to thanks my colleagues the cosmic-ray group of Kyoto University; Prof. Katsuji Koyama, Prof. Takeshi Tsutu, Dr. Yuji Tazawa, Dr. Fumihide Iwamuro, Mr. Hiroshi Murakami, Mr. Jun Yokogawa, Ms. Aya Bamba, Mr. Kensuke Imanishi, Mr. Makoto Kouno. Mr. Tsutomu Nagayoshi, Mr. Masaru Ueno, Ms. Reiko Orito, Mr. Atsushi Senda Mr. Shin'ichiro Takagi, Mr. Daisuke Nishida, Ms. Shio Watanabe, and Ms. Ayako Furumori, for their encouragement.

The receipt of Research Fellowships of the Japan Society for the Promotion of Science for Young Scientists is also acknowledged.

Bibliography

[1] Becker,R.H., *et al.*, ApJL, 240, 713, 1980.

[2] Bell,A.R., MNRAS, 182, 147, 1978.

[3] Chadwick,P.M., *et al.*, Proc. GeV-TeV gamma-ray Astrophysics Workshop (August 13-16, 1999, Snowbird, USA; AIP Conf. Proc. 512, 210-214, 2000).

[4] Chevalier,R.A., Kirshner,R.P., and Raynolds,J.C., ApJ, 235, 186, 1980.

[5] Enomoto,R., *et al.*, Proc. 27th ICRC, Hambrug, 2477, 2001.

[6] Enomoto,R., *et al.*, Astropart. Phys., 16, 235, 2002.

[7] Fermi,E., Phys. Rev., 75, 1169, 1949.

[8] Gardner,F.F., and Milne,D.K., AJ, 70, 754, 1965.

[9] Gunji,S., *et al.*, CANGAROO observation manual Ver.0105, 2001.

[10] Hara,S., Master's thesis, Tokyo Institute of Technology, 1999.

[11] Hara,S., *et al.*, Proc. 27th ICRC, Hambrug, 2455, 2001.

[12] Hartman,R.C., *et al.*, Astrophys. J., Suppl. Ser. 123, 79, 1999.

[13] Hayakawa,S., Prog. Theor. Phys. 8, 571, 1952.

[14] Hayami,H., Master's thesis, Tokyo Institute of Technology, 1997.

[15] Hayashida,N., *et al.*, Phys. Rev. Lett. 73, 3491, 1994.

[16] Hillas,A.M., Proc. 19th ICRC, 3, 445, 1985.

[17] Ichimura,M., *et al.*, Phys. Rev. D, 48, 1949, 1993.

[18] Ichizawa,S., Graduation thesis, Tokyo Institute of Technology, 1995.

[19] Jelley,J.V., Cerenkov Radiation and its Applications, Pergamon Press, p219, 1958.

[20] Jungman,G., Kamionkowski,M., Griest,K., Rep. 267, 195, 1996.

[21] Kamei,S., Graduation thesis, Tokyo Institute of Technology, 1996.

[22] Kamei,S., Master's thesis, Tokyo Institute of Technology, 1998.

[23] Kawachi,A., *et al.*, Proc. 26th ICRC, Salt Lake City, 5, 207, 1999.

[24] Kawachi,A., *et al.*, Astropart. Phys. 14, 261-269, 2001.

[25] Kifune,T., *et al.*, Astrophys. J. 438, 91, 1995.

[26] Kirshner,R.P., Winkler,P.F., and Chevalier,R.A., ApJ, 315, L135, 1987.

[27] Koyama,K., *et al.*, PASJ, 39, 437, 1987.

[28] Koyama,K., *et al.*, Nature, 378, 255, 1995.

[29] Koyama,K., *et al.*, PASJ 49, L7, 1997.

[30] Kubo,H., *et al.*, Prec. 27th ICRC, Hambrug, 2900, 2001.

[31] Li,T., and Ma,Y., Astrophys. J.272, 317-324, 1972.

[32] Long,K.S., Blair,W.P., and van den Bergh,S., ApJ, 333, 749, 1988.

[33] Mastichiadis,M., A&A, 305, L53, 1996.

[34] Mastichiadis,M., and de Jager,O.C., A&A, 311, L5, 1996.

[35] Mattox,J.R., *et al.*, ApJ, 461, 396, 1996.

[36] Michelson,P.F., in Proc. Towards a Major Atmospheric Cherenkov Detector-III, edited by Kifune,T., page 257, Universal Academy, Tokyo, 1994.

[37] Mori,M., *et al.*, Proc. 26th ICRC, Salt Lake City, 5, 287, 1999.

[38] Mori,M., *et al.*, Proc. GeV-TeV gamma-ray Astrophysics Workshop (August 13-16, 1999, Snowbird, USA; AIP Conf. Proc. 515), 2000.

[39] Mori,M., *et al.*, to appear in Proc. High Energy Gamma-ray Astronomy (June 26-30, 2000, Heidelberg, Germany; AIP Conf. Proc. 558), 2001.

[40] Moriya,M., Ph.D thesis, Tokyo Institute of Technology, 2000.

[41] Muraishi,H., *et al.*, A&A 354, L57, 2000.

[42] Murakami,T., *et al.*, Nature, 368, 127-129, 1994.

[43] Morrison,P., IL Nuovo Cimento 7, 858, 1958.

[44] Minkoski,R., AJ, 71, 371, 1966.

[45] Naito,T., *et al.*, Aston. Nachr., 320, 205-206, 1999.

[46] Nomachi,M., *et al.*, in Proc. Int. Conf. on Computing on High Energy Physics '94, LBL-35822, p114, 1994.

[47] Nomoto,K., Thieleman,F., and Yokoi,K., ApJ, 266, 405, 1984.

[48] Ogio,S., Master's thesis, Tokyo Institute of Technology, 1990.

[49] Okumura,K., *et al.*, Proc. 27th ICRC, Hambrug, 7, 2679, 2001.

[50] Oosaki,T., Master's thesis, Tokyo Institute of Technology, 1996.

[51] Ozaki,M., Ph.D thesis, Kyoto University, 1998.

[52] Pfeffermann,E., and Aschenbach,B., Proc. 'Röntgenstrahlung from the Universe', eds. Zimmermann, H.U.; Trümper, J.; and Yorke, H.; MPE Report 263, p. 267-268, 1996.

[53] Pohl,M., A&A, 307, 57 ,1996.

[54] Punch,M., *et al.*, 1991, Proc. 22nd. ICRC, vol1,464

[55] Punch,M., *et al.*, 1992, Nature, 358, 477

[56] Ramana Mourth,R.V., and Wolfendare,A.W., Gamma-ray Astronomy, Cambridge University Press, 1986.

[57] Reynolds,S.P., and Ellison,D.C., Proc. 22th ICRC (Dublin), 2, 404, 1991.

[58] Reynolds,S.P., and Ellison,D.C., ApJL, 399, L75, 1992.

[59] Roger,R.S., *et al.*, ApJ, 332, 940, 1988.

[60] Rothenflug,R., *et al.*, Proc. "New Visions of the X-ray Universe in the XMM-Newton and Chandra era", Noordwijk, 2001.

[61] Sakurazawa,K., Ph.D thesis, Tokyo Institute of Technology, 1999.

[62] Sakurazawa,K., Master's thesis, Tokyo Institute of Technology, 1996.

[63] Sakurazawa,K., Graduation thesis, Tokyo Institute of Technology, 1994.

[64] Sokolsky,P., Introduction to Ultrahigh Energy Cosmic Ray Physics (Addion-Wesley Publishing Company, Inc.), 1989.

[65] Susukita,R., Ph.D thesis, Kyoto University, 1997.

[66] Suzuki,R., Master's thesis, Tokyo Institute of Technology, 1998.

[67] Swanenburg,B.N., *et al.*, Astrophys. J. 450, 784, 1995.

[68] Tanimori,T., *et al.*, ApJL 492, L33-L36, 1998.

[69] Tanimori,T., Progress of Theorical Phys., Suppl., 143, 78, 2001.

[70] Tanimori,T., *et al.*, Proc. 27th ICRC, Hambrug, 2465, 2001.

[71] Teshima,M., *et al.*, "Telescope Array Project", ICRR, 1993.

[72] Thompson,D.J., *et al.*, Astrophys. J., Suppl. Ser. 86, 625, 1993.

[73] Tomida,M., Ph.D thesis, Kyoto University, 2000.

[74] Tomii,A., Graduation thesis, Tokyo Institute of Technology, 1996.

[75] Tsukagoshi,T., Master's thesis, Tokyo Institute of Technology, 1994.

[76] Vartanian,M.H., Lum,K.S.K., and Ku,W.H., ApJ, 255, L5, 1985.

[77] Weekes,T.C., Phys. Rep., 160, 1, 1988.

[78] Weekes,T.C., ApJ, 342, 379, 1989.

[79] Willingale,R., *et al.*, MNRAS, 278, 749, 1996.

[80] Wu,C., Leventhal,M., Sarazin,C.L., and Gull,T., ApJL, 269, L5-L9, 1983.

[81] Yoshida,T., and Yanagita,S., Proc. 2nd INTEGRAL Workshop (Transparent Universe), ESASP-382, 85, 1997.

[82] Yoshikoshi,T., Master's thesis, Tokyo Institute of Technology, 1993.

[83] Yoshikoshi,T., Ph.D thesis ,Tokyo Institute of Technology, 1996.

[84] Yoshikoshi,T., *et al.*, Astrophys. J. Lett., 487, L65, 1997.

[85] van den Bergh,S., ApJ, 208, L17, 1976.

[86] CERN Program Library Long Writeup W5013, 1994.

[87] Proposal for the Gamma-ray Large Area Space Telescope-GLAST, submitted to the Department of Energy by the GLAST Collaboration. SLAC Report 522, 1998.

[88] `http://chandra.harvard.edu/photo/0237/`

[89] `http://chandra.harvard.edu/photo/0052/`

[90] `http://cossc.gsfc.nasa.gov/cossc/egret/3rd_EGRET_Cat.html`

[91] `http://glast.riken.go.jp/`